NASA
Technical
Paper
2442
November 1985

# Vortex Wake Alleviation Studies With a Variable Twist Wing



G. Thomas Holbrook,
Dana Morris Dunham,
and George C. Greene



NASA

**NASA Technical Paper 2442**

1985

# Vortex Wake Alleviation Studies With a Variable Twist Wing

G. Thomas Holbrook,
Dana Morris Dunham,
and George C. Greene

*Langley Research Center*
*Hampton, Virginia*

National Aeronautics
and Space Administration

**Scientific and Technical Information Branch**

## Contents

## Summary

Vortex wake alleviation studies were conducted in a wind tunnel and a water towing tank using the variable twist wing, a vortex-generator model capable of controlled and measured variations in span load. Fourteen different configurations of the multisegmented wing model were tested at a Reynolds number of $1 \times 10^6$ and a lift coefficient of 0.6 in the Langley 4- by 7-Meter Tunnel and the Hydronautics Ship Model Basin water tank at Hydronautics, Inc., Laurel, Md. In the wind tunnel, detailed span load measurements were taken and detailed near-wake data obtained with hot-film anemometer and trailing-wing surveys. In the water tank, near- and far-wake trailing-wing rolling-moment surveys were made. The tests examined the roles of span load, drag, and turbulence distributions in vortex wake alleviation. An additional objective was to determine whether relatively simple analytical predictions of span load and wake roll up could realistically characterize the vortex generator span load and the resulting vortex wake development.

The variety of measurements allowed results to be correlated and their accuracy to be checked between test facilities as well as between wing and wake measurements. In this manner, several facility and measurement technique effects were found to have significantly influenced portions of either the vortex wake roll up or the experimental quantification of vortex wake intensity. Detailed wind tunnel measurements of span load distributions on the wing and cross plane wake velocities at a semispan downstream correlated well with each other and with water tank measurements of peak trailing-wing rolling moments. These detailed measurements were used to show that inviscid analytical prediction techniques accurately portrayed the vortex generator span load distribution and initial vortex wake development to the resolution limits of the data. However, meander and flow angularity in the wind tunnel prevented, in other than a qualitative sense, the use of wake velocity data measured at 6 and 11 semispans downstream. Average trailing-wing rolling moments were shown to be unreliable as a measure of the vortex intensity because vortex meander amplification did not scale between the test facilities and free-air conditions. High values of meander amplification caused average trailing-wing rolling-moment data in both facilities, as well as wake velocity data in the wind tunnel, to falsely indicate rapid vortex decay with downstream distance.

A tapered-span-load configuration, which exhibited little or no drag penalty, was shown to offer significant downstream wake alleviation to a small trailing wing. This wing configuration achieved wake alleviation through span load specification of more uniform vorticity shedding at the wing trailing edge. In contrast, the greater downstream wake alleviation achieved with the addition of spoilers to a flapped-wing configuration was shown to result directly from the high incremental drag and turbulence associated with the spoilers and not from the span load alteration they caused.

## Introduction

Large aircraft produce vortex wakes which can cause severe roll upset to encountering aircraft within several miles of the generating aircraft. To preclude hazardous operations within airport terminal areas, pilots are advised (and required under IFR (instrument flight rules) conditions) to maintain longitudinal aircraft spacings of up to 6 n.mi. Should these requirements be maintained into the 1990's, the benefits of new four-dimensional terminal control and landing systems technology may be limited. The growth of air transportation capacity could thus be inhibited and its cost increased. Both near- and far-term solutions to the vortex wake problem are being sought in a joint research program conducted by the National Aeronautics and Space Administration and the Federal Aviation Administration. NASA is investigating vortex wake alleviation and the FAA is pursuing wake detection and avoidance technology. Portions of this research are compiled in references 1 and 2, respectively.

Since 1970, fundamental and applied vortex wake research has been aimed at understanding the physics of vortex flows and determining the effects of the vortex-generating aircraft and surrounding atmospheric conditions on the vortex wake roll up and decay. This work has encompassed a broad spectrum of experimental, computational, and theoretical aerodynamics (refs. 1 to 6); this broad-based approach is necessitated by the extensive domain of vortex flows. From birth to death of a typical aircraft vortex wake system, a vast downstream distance is traversed and flow regimes range from inviscid to viscous and laminar to turbulent. This complex system is immersed in an atmosphere that can influence the life of the vortex system according to its turbulence and stability levels. During this life cycle, the vortex wake is generally believed to pass through three less-than-distinct phases: (1) vortex generation and roll up, (2) a stable, plateau region often exhibiting the onset of mutual induction instabilities, and (3) vortex decay and breakdown. Because each phase is uniquely suited to certain types of experimental and analytical techniques, and since the wake exists over such a large downstream distance, most vortex wake

research has necessarily been limited to independent investigation of each phase.

Another difficulty encountered in vortex wake research is the need for very detailed knowledge of the wing load distribution because the aerodynamic state of the aircraft or model serves as the initial condition for the transformation from wing flow to wake flow. To determine the relationship between wing load distribution and wake development, however, a variety of load distributions must be tested. Typically, this would require the use of several models, each extensively instrumented to obtain pressure distribution data. The cost of designing and building numerous models of this complexity is prohibitive.

For this investigation, the requirements for multiple span loads and large downstream distances were met by testing a unique, pressure-instrumented variable twist wing (VTW) model both in a wind tunnel, to obtain detailed wing and near-wake measurements, and in a water towing tank, where wake measurements were made at near- and far-downstream distances. The VTW, shown in figure 1, is a multisegmented wing model capable of controlled and measured variations in span load. This capability eliminates the need for several models. Drag and turbulence distributions were varied using spoilers, splines, or drag plates.

Spoilers and splines have been shown to be vortex attenuators (refs. 7 to 9) because when properly located on a vortex-generator model or aircraft, the wake of the vortex generator imposes a reduced rolling moment on a smaller trailing wing or aircraft. One specific objective of these tests was to determine how spoilers alleviate the roll upset experienced by following aircraft. Thus, spoilers were used as vortex attenuators in this investigation. However, the splines and drag plates were not applied strictly as attenuators, but instead were used to control the drag and turbulence distributions of the VTW.

Reduction of the rolling moment imposed on a trailing wing results from reducing the vortex tangential velocity over the region occupied by the following model or aircraft. Peak tangential velocities are reduced by increasing the size of the vortex core. An indicator of the vortex core radius is the vorticity dispersion radius, which characterizes the spread of vorticity, either as shed at the vortex generator wing or in the rolled-up vortex wake. The vorticity centroid $\bar{b}/2$ and the vorticity dispersion radius $\bar{d}$ are directly analogous to the mean and standard deviation of the vorticity distribution shed at the wing $(d\Gamma'(y)/dy)$. (See fig. 2.) Similarly, in the wake, the vorticity distribution $\Omega(y,z)$ determines the vorticity centroid (the lateral centroid position $\bar{y}$ is shown in fig. 2) and the vorticity dispersion radius, but the latter is now a function of time or downstream distance. For a given input angular momentum, represented by the vortex generator centerline circulation $\Gamma_o$, the aim is to reduce the vortex wake roll upset potential to a small trailing wing by increasing the vorticity dispersion radius in the wake.

There are a number of ways to increase the vorticity dispersion radius. One direct approach is to alter the span load of the vortex generator so that the vorticity dispersion is greater initially. In 1933, Betz (ref. 10) developed an approximate analysis describing the relationship between the span load and the vorticity dispersion radius. Span load alteration has been applied in several theoretical and experimental works. (See refs. 11 to 13.) A second method of increasing the vorticity dispersion deals with the diffusion of vorticity away from the vortex center, a process which occurs naturally because of laminar and turbulent viscous effects. In quiescent atmospheric conditions, if little turbulence is produced by the vortex generator, this process is much too slow. Therefore, the introduction of turbulence-producing devices on the vortex generator can enhance the growth of the vorticity dispersion radius in the downstream wake. Another approach is to reduce the flux of angular momentum into the wake by increasing the vortex generator drag distribution locally. The increased drag creates an unfavorable axial pressure gradient and, if properly located, retards the local acceleration of the vortex sheet. The convective concentration of the entire sheet is thus altered, and a rolled-up wake with a greater vorticity dispersion radius results. This effect is analogous to the vortex deintensification that occurs as a result of including the wing drag distribution in a Betz inviscid wake roll-up calculation, as described in reference 14.

Splines increase the wing drag distribution locally and thereby impose an adverse axial pressure gradient on the vortex wake. Splines also increase the turbulence shed into the wake. (The original design motivation for the splines, however, was the desire to create an axial pressure gradient. See ref. 8.) Spoilers produce all three effects, since in addition to increasing the drag and turbulence distributions, they also alter the span load. This investigation used the span load tailoring capability of the VTW and also made selective use of splines and drag plates for controlling drag and turbulence distributions in order to determine the chief mechanism responsible for spoiler-produced vortex wake alleviation.

Fourteen different configurations of the VTW were tested to examine the roles of span load, drag, and turbulence distributions in vortex wake alleviation with attention to performance penalties on the vortex generator. An additional objective was to

determine whether relatively simple analytical predictions of span load and wake roll up could realistically characterize the vortex generator span load and the resulting vortex wake development. Both the vortex generator and vortex wake measurements were sufficiently detailed to allow comparisons with the analytical predictions of each and to enable an evaluation of the test facility and measurement technique effects. Appendixes A and B present test method details and experimental influences, respectively.

## Symbols

| | |
|---|---|
| $A$ | wing aspect ratio, $b^2/S$ |
| $b$ | wing span, m |
| $\bar{b}/2$ | vorticity centroid of wing lift distribution relative to wing centerline (does not include effects of lifting centerbody) (see fig. 2), m |
| $\bar{b}/b$ | normalized vorticity centroid of wing lift distribution relative to wing centerline (does not include effects of lifting centerbody) |
| $C_A$ | axial-force coefficient, $\frac{\text{Axial force}}{q_\infty S}$ |
| $C_D$ | drag coefficient (referenced to geometric angle of attack $\alpha$), $\frac{\text{Drag}}{q_\infty S}$ |
| $C'_D$ | drag coefficient corrected for possible angle-of-attack inaccuracies, $\frac{C_N \sin(\alpha + \alpha_o) + C_A \cos(\alpha + \alpha_o)}{q_\infty S}$ |
| $C_L$ | lift coefficient (referenced to geometric angle of attack $\alpha$), $\frac{\text{Lift}}{q_\infty S}$ |
| $C'_L$ | lift coefficient corrected for possible angle-of-attack inaccuracies, $\frac{C_N \cos(\alpha + \alpha_o) - C_A \sin(\alpha + \alpha_o)}{q_\infty S}$ |
| $C_{L,\text{CB}}$ | centerbody lift coefficient, $\frac{\text{Centerbody lift}}{q_\infty S}$ |
| $C_{L,p}$ | lift coefficient integrated from right wing $c_p$ data, $\frac{\text{Integrated lift}}{q_\infty S}$ |
| $C_{l,\text{AV}}$ | magnitude of maximum average $C_{l,\text{TW}}$ value measured for a vortex of significant strength in a $Y$-$Z$ cross plane with trailing wing at fixed $y, z$ position |
| $C_{l,\text{PK}}$ | magnitude of maximum $C_{l,\text{TW}}$ value measured for a vortex of significant strength in a $Y$-$Z$ cross plane |
| $C_{l,\text{TW}}$ | trailing-wing rolling-moment coefficient, $\frac{\text{Rolling moment}}{q_\infty S b}$ |
| $C_N$ | normal-force coefficient, $\frac{\text{Normal force}}{q_\infty S}$ |
| $c$ | wing chord, m |
| $c_\ell$ | section lift coefficient, $\frac{\text{Section lift}}{q_\infty c}$ |
| $c_{\ell,o}$ | $c_\ell$ at wing centerline |
| $c_n$ | section normal-force coefficient integrated from chordwise $c_p$ data |
| $c_p$ | static pressure coefficient, $\frac{p - p_\infty}{q_\infty}$ |
| $\bar{d}$ | vorticity dispersion radius of wing lift distribution relative to vorticity centroid position (does not include effects of lifting centerbody) (see fig. 2), m |
| $i, j$ | indices |
| $\ell$ | incremental length vector, m |
| $\Delta\ell$ | grid square element length on interpolated wake velocity grid, m |
| $n$ | index for labeling vorticity contour levels, where $\Omega s/U_\infty = \pm e^n/2$, $n = 0,\ 1,\ 2,\ \ldots$ |
| $p$ | static pressure, Pa |
| $q$ | dynamic pressure, Pa |
| $r$ | radius from center of vortex, m |
| $S$ | wing reference area, $m^2$ |
| $s$ | VTW semispan, m |
| $\bar{s}$ | lift centroid position of wing lift distribution (does not include effects of lifting centerbody) (see fig. 2), m |
| $t$ | time, sec |
| $U$ | total velocity vector, m/sec |
| $u, v, w$ | velocity components in $X, Y, Z$ Cartesian coordinate system, respectively, m/sec |

$u_{av}, v_{av}, w_{av}$ averaged velocity components in $X, Y, Z$ Cartesian coordinate system, respectively, m/sec

$\bar{u}, \bar{v}, \bar{w}$ interpolated velocity components in $X, Y, Z$ Cartesian coordinate system, respectively, m/sec

$X, Y, Z$ right-hand Cartesian coordinate system originating at centerline of VTW trailing edge with $X$ aligned to wind tunnel or water tank longitudinal centerline, $Y$ aligned horizontally along right wing and perpendicular to $X$, and $Z$ aligned vertically upward (see fig. 3)

$X_{LE}$ VTW body axis aligned with local chord and originating at wing leading edge

$x, y, z$ longitudinal, lateral, and vertical dimensions along $X, Y, Z$ Cartesian coordinate system, m

$x_{LE}$ dimension along $X_{LE}$ axis, m

$\bar{y}$ lateral vorticity centroid of VTW wake relative to wing centerline, m

$|y_{TW}|$ $y$ magnitude at which $C_{l,AV}$ measurement obtained, m

$y_\Omega$ $y$ value of vortex center determined from wake velocity measurements, m

$\alpha$ geometric angle of attack of wing centerline chord, deg

$\alpha_o$ angular offset between free-stream velocity and $\alpha = 0°$, deg

$\Delta\alpha$ wing segment twist angle relative to wing centerline chord (wing segment leading edge up is positive), deg

$\beta$ vorticity dispersion radius for a Gaussian distribution of vorticity, m

$\Gamma$ circulation measured over wake survey cross plane in semispan wake of VTW (see fig. 2), $m^2/sec$

$\Gamma_o$ circulation at wing centerline as derived from lift distribution measurements (does not include effects of lifting centerbody) (see fig. 2), $m^2/sec$

$\Gamma'$ circulation distribution along VTW semispan as derived from lift distribution measurements (does not include effects of lifting centerbody) (see fig. 2), $m^2/sec$

$\rho$ density, $kg/m^3$

$\sigma_u$ standard deviation of $u$ velocity component, m/sec

$\sigma_w$ standard deviation of $w$ velocity component, m/sec

$\Omega$ streamwise component of vorticity measured over wake survey cross plane in semispan wake of VTW (see fig. 2), $sec^{-1}$

Subscript:

$\infty$ free-stream conditions

## Test Facilities

Two test facilities were used in this investigation: the Langley 4- by 7-Meter Tunnel and the Hydronautics Ship Model Basin (HSMB), a water towing tank at Hydronautics, Inc., Laurel, Md. The wind tunnel tests emphasized detailed model aerodynamic data and detailed near-wake data, whereas the water tank tests were used primarily to collect far-wake rolling-moment data.

### Langley 4- by 7-Meter Tunnel

The test section of the Langley 4- by 7-Meter Tunnel (fig. 1) has a height of 4.42 m, a width of 6.63 m, and a length of 15.24 m. The VTW was blade mounted atop a sting in the upstream end of the test section, near the entrance cone, and maintained at test section centerline during test runs. Angle of attack was determined from an accelerometer mounted in the fuselage. A six-component strain-gauge balance was used to determine lift and drag for the wing and centerbody combination.

A survey rig, also pictured in figure 1, was used in these tests for $Y, Z$ cross plane sampling of either the three wake velocity components or the rolling moment on a trailing-wing model in the VTW wake. The survey rig could be positioned in the test section from 1 to 11 semispans behind the VTW. Either a hot-film probe or a trailing-wing model was mounted

to the motor-driven traverse mechanism on the survey rig to allow both lateral and vertical movements. Digital encoders on the traverse mechanism provided the lateral and vertical position of the sensor during test runs.

### Hydronautics Ship Model Basin Water Tank

The HSMB is a water towing tank facility 125 m long and 7.32 m wide, with a water depth of 3.81 m. Two independently powered carriage systems were used to propel the VTW and trailing-wing models through the tank. (See fig. 3.) The VTW quarter-chord line was located $1.12s$ below the waterline and the model was attached overhead to the lead carriage by a blade mounted to a tilt table. The tilt table provided for angle-of-attack adjustment. Variable reluctance force measuring block gauges (ref. 15), attached internally to the VTW centerbody, measured lift and drag from the model wing only. (Centerbody forces were not measured.)

The trailing-wing carriage had a motor-driven scan system which traversed 46 cm vertically during each run at a rate of 4 cm/sec through the wake of the VTW. The lateral position of the blade-mounted trailing wing was changed manually between runs. Separation distance between the two models was determined using the time differential for the two carriages to pass the midlength point of the water tank and the measured speed of the two carriages. Prior vortex wake work in this facility indicated that 15 minutes between runs was sufficient time to allow the model-induced turbulence levels in the tank to damp to quiescent conditions. Although the turbulence was not measured directly, a comparison of flow field steadiness at $x/s = 11$ in both test facilities indicated a substantially lower turbulence level in the water tank.

## Models

### Variable Twist Wing

Two variable twist wing (VTW) models were used during this investigation: an extensively instrumented aluminum model which provided force and moment data as well as detailed span load measurements in the wind tunnel, and an anodized aluminum model which provided force and moment data only in the water tank. The wind tunnel VTW was mounted atop a faired support strut which attached to the centerbody. The water tank VTW was mounted below a faired support strut which attached to the tail cone. Other than model installation differences, the VTW models were geometrically identical and were the same size.

The VTW model is shown mounted in the wind tunnel in figure 1, and a schematic with dimensions is shown in figure 4. The model had a metal wing with an aspect ratio of 7, a span of 2.489 m, and an NACA 0012 airfoil section. The wing consisted of 72 segments (each 2.96 cm wide and independently rotatable about its quarter chord), with 36 installed on each side of a wing center panel of 35.56 cm span fixed to the centerbody. A body-of-revolution wing-tip cap was fitted to each wing tip and twisted in unison with the final outboard wing segment. Spoilers, splines, or drag plates were added to several VTW configurations, as shown in figure 5. These devices were centered at $y/s = \pm 0.607$ and the splines and drag plates were mounted aft of the trailing edge at about $x/s = 0.122$ (or $x/c = 0.43$).

The wind tunnel VTW model had 580 pressure taps for measurement of spanwise and chordwise pressure distributions. Pressure coefficient data were obtained along 19 spanwise positions on the right wing and 1 symmetrically matching position just left of the wing centerline. Spanwise and corresponding chordwise positions of each pressure orifice are given in table I. Right-wing segments were hollowed to accept either pressure orifice tubing or electronic scanning pressure transducers and associated wiring. Generally, alternate segments contained the pressure transducers, which accepted the pressure orifice inputs from the adjacent segment through openings in each side of the segment. These openings were sized and located to accommodate up to 15° twist between adjacent segments without unsealing the openings to the free stream. Pressure data were taken under computer control with all 580 orifices electronically scanned and recorded in 0.1 sec.

Thus, the VTW design allowed the span load distribution to be tailored via wing segment twist, and the pressure instrumentation permitted accurate measurement of the pressure distribution over the wing. Fourteen VTW configurations that differed in either wing twist distribution or wing device installations were tested for this investigation. The configurations, shown in figure 6, are categorized into three groups—continuous span load distributions, partial-span-flap span load distributions, and alleviated vortex wake configurations. This grouping system differentiates between the configurations of group I, which produced one predominant vortex per semispan, and those of group II, which shed multiple semispan vortices. The configurations of group III were tested to examine the mechanism of spoiler-produced vortex wake alleviation. The configurations are given designations and are described in table II. These groupings and configuration designations will be utilized throughout the remainder of this report.

Details of the wing twist distributions and wing device installations are given in table III and are plotted with the span load data.

### Trailing Wing

Measuring the rolling moment on a smaller wing positioned in the wake of the vortex generator has become an accepted means of quantifying the hazard posed by the vortex wake system of a particular configuration. (See refs. 16 to 27.) The aspect-ratio-5.35 trailing wing used for these tests has a span equal to 13 percent of the VTW span. A photograph and dimensions of the unswept trailing-wing model installed on the wind tunnel traverse mechanism are presented in figure 7. In each test facility, the model was mounted on a roll balance and attached to a traverse mechanism capable of positioning the model both laterally and vertically as required in the VTW wake. The trailing-wing balance used in the water tank tests also measured lift and drag. Positive and negative lift on the trailing wing was used to determine if it was in an upwash or downwash region. This determination aided in positioning the wing relative to major-strength vortices.

## Test Method

The VTW was tested at a Reynolds number of $1 \times 10^6$, based on wing chord, in both facilities. This condition required free-stream dynamic pressure and velocity values of 1005 Pa and 40.52 m/sec, respectively, in the wind tunnel and 5049 Pa and 3.179 m/sec, respectively, in the water tank. All measurements of VTW span load distributions, trailing-wing rolling moments, and wake velocities were made with the VTW at a $C_L$ of 0.6 to avoid stall over any twisted portion of the wing. Additional VTW aerodynamic data were taken through an angle-of-attack range in the wind tunnel. The types of data taken in this investigation are summarized in table IV according to downstream distance and test facility. Generally, the wind tunnel test was used to obtain detailed model and near-wake data and the water tank test was used to obtain far-wake rolling-moment data. The following paragraphs summarize each set of measurements in both facilities; details of the measurement techniques are presented in appendix A.

Wind tunnel measurements of $C_L$ and $C_D$ for each VTW configuration were taken from an angle of attack of $-4°$ to beyond stall in increments of $2°$. Except on the untwisted wing configuration (VTW1), water tank measurements of the longitudinal aerodynamic data were made only at $C_L = 0.6$. Several factors influenced the accuracy and repeatability of the $C_L$ and $C_D$ measurements obtained in both facilities. At $C_L = 0.6$, force balance accuracy for lift was within $\pm 4.5$ percent in the wind tunnel and $\pm 1.1$ percent in the water tank, whereas drag accuracy of the utilized force balances was quite poor—for a worst case situation, drag accuracy was possibly only within $\pm 53$ percent in the wind tunnel and $\pm 25$ percent in the water tank. The data signals from both test facilities were low-pass filtered and averaged over long time periods to remove the effects of model vibrations, flow turbulence, and $q_\infty$ fluctuations. Although these techniques could not improve the measurement accuracy, they brought the overall repeatability for $C_L$ to within $\pm 3$ percent in both facilities and improved the $C_D$ repeatability to within $\pm 7$ percent in the wind tunnel and $\pm 3$ percent in the water tank. This level of $C_D$ consistency was adequate for the purposes of the present tests since drag was measured mainly to obtain significant $C_D$ differences between VTW configurations in the same facility.

As noted previously, electronic scanning pressure transducers were incorporated within VTW wing segments for the wind tunnel test to allow computer-controlled recording of all 580 pressure orifice values in about 0.1 sec. These values were then transformed to $c_p$ data, integrated chordwise to obtain span load pressure distributions, and integrated over the right wing to obtain the wing-alone lift coefficient $C_{L,p}$. The accuracy of the electronic scanning pressure transducers assured that each chordwise $c_n$ integration was within $\pm 0.02$ of the true value and that overall $C_{L,p}$ error was typically less than $\pm 2$ percent. Several parameters were computed from the measured span load distributions for comparison with the measured vorticity distributions in the wake and also with the trailing-wing rolling-moment data. The lift centroid $\bar{s}$, wing centerline circulation $\Gamma_o$, vorticity centroid $\bar{b}/2$, and vorticity dispersion radius $\bar{d}$ were calculated as shown in appendix A. This report emphasizes span load data derived from the pressure distribution measurements rather than chordwise $c_p$ data. Complete chordwise and spanwise $c_p$ measurements for the VTW configurations tested in the wind tunnel are given in reference 28.

Trailing-wing rolling-moment surveys of the VTW wake were made at four downstream distances—near-field data were taken in the wind tunnel at $x/s = 6$ and 11, and far-field data with a near-field overlap were taken in the water tank at $x/s = 11$, 40, and 70. In the wind tunnel, the trailing-wing rolling-moment signal was sent through a 0.1-Hz low-pass filter and the output was averaged over a long period at each $y, z$ survey point. In the water tank, the trailing-wing rolling-moment signal was recorded with a 20-Hz resolution in an analog format from

which peak and long-period average data were determined. In both facilities, a sufficient number of runs were made at each downstream survey cross plane to insure that the maximum rolling-moment coefficient had been measured for each vortex of significant strength. These maximum rolling moments are presented as $C_{l,\mathrm{PK}}$ for water tank peak data and as $C_{l,\mathrm{AV}}$ for wind tunnel and water tank averaged data.

Wake velocity surveys were made in the wind tunnel at three downstream positions ($x/s$ = 1, 6, and 11) behind the right wing for each of four wing twist configurations (VTW4, VTW7, VTW7$S_0$, and VTW7$S_3$). At each downstream location, semispan cross plane surveys of $u$, $v$, and $w$ velocities were made using a three-component hot-film probe attached to the traverse mechanism on the survey rig. The hot-film probe traversed the cross plane continuously at 1.3 cm/sec along about 55 horizontal rows which were separated vertically by 1.3 cm ($0.01s$) in high-vorticity regions and spread to about 5 cm ($0.04s$) apart near the upper and lower cross plane boundaries. The analog hot-film voltage signals were sampled at the rate of 50 points per second and $0.02s$ spatial averages of probe position and flow velocities were computed in running-average fashion for each horizontal traverse. To compute vorticity ($\Omega$) contours within each cross plane, the averaged velocities were linearly interpolated to a $0.02s$ (2.6-cm) mesh grid and vorticity was determined at the center of each grid square by taking the line integral of velocity around the square per unit area. Additional details of the computation of the vorticity cross planes can be found in appendix A. The interpolated velocities were also used to determine the total circulation $\Gamma$ and the lateral vorticity centroid position $\bar{y}$ in the wake cross plane for comparison with their counterparts measured on the VTW, $\Gamma_o$ and $\bar{b}/2$.

## Presentation of Results

Results are presented under the five text subheadings listed in the first column of the table below. Figures pertinent to each subheading are also listed. Within each subheading (except that entitled Predicted and Measured Vortex Wake Development) the results will be addressed in the following order:

Aerodynamic data
Span load data
Trailing-wing rolling-moment data
Wake velocity data

Additional overall results are presented in tables V to VII.

| Text subheading | Text page | Pertinent figures |
|---|---|---|
| Effects of Facilities and Measurement Techniques | 24 | B1–B11 |
| Predicted and Measured Vortex Wake Development | 27 | 8–11 |
| Effects of Continuous Span Load Distributions | 31 | 12–16 |
| Effects of Partial-Span-Flap Span Load Distributions | 35 | 17–21 |
| Effects of Alleviated Vortex Wake Configurations | 37 | 22–28 |

## Discussion

### Effects of Facilities and Measurement Techniques

Several facility and measurement technique effects were found to have significantly influenced portions of either the vortex wake roll up or the experimental quantification of vortex wake intensity. These findings and their impact on the interpretation of the test results are summarized here. A detailed discussion of these results can be found in appendix B, entitled Experimental Influences.

***Aerodynamic data.*** A comparison of the wind tunnel and water tank VTW1 aerodynamic data from an $\alpha$ of $-6°$ to $16°$ was made to ascertain that the $C_L$ and $C_D$ data correlated between facilities and thus that the wakes shed at the wing trailing edge were similar. It was determined that $C_L$ and $C_D$ data could be correlated between the test facilities once angle-of-attack corrections were applied. Although flow angles were not measured directly in either test facility, this and other investigations with the VTW and similar models indicated a wind tunnel $\alpha$ correction of about $+0.5°$ due to flow angularity and a water tank $\alpha$ correction of about $-0.5°$ due to reference frame offsets. Application of these corrections correlated the two data sets well. Since $C_D$ is very sensitive to $\alpha$ corrections (a $1°$ correction in angle of attack changes $C_D$ by 33 percent) and because the exact $\alpha$ correction for each facility is unknown, the $C_D$ data cited in this report are uncorrected and are useful mainly for drag comparisons between VTW configurations in the same facility.

The survey rig was located at $x/s$ = 6 or 11 when aerodynamic data were measured through an $\alpha$

range. At these locations, the survey rig had no effect on the aerodynamic data. However, when the survey rig was used for making wake velocity surveys behind the right wing at $x/s = 1$, it caused an upwash of greater than 0.6° across the right wing and an increased $C_L$. The effect of the survey rig on the wake velocity data at this station was negated for the most part by making a reduction in $\alpha$ to maintain $C_L = 0.6$. This reduction left a small swirl in the wake induced by the higher loading on the right wing of the VTW.

***Span load data.*** Wind tunnel pressure distribution measurements on all VTW configurations indicated a wing centerline span load asymmetry. A small lateral flow angularity toward the left wing caused the centerbody to block the flow on the lower surface of the wing just left of centerline and thereby reduced $c_\ell$ at $y/s = -0.0612$. Negligible rolling moment on the VTW indicated that the span load effect was localized just left of centerline. For this reason, the $c_\ell$ data at $y/s = -0.0612$ were ignored in evaluating $C_{L,p}$, $\bar{s}$, $\Gamma_o$, $\bar{b}/2$, and $\bar{d}$. (The determination of these values from the span load data is given in appendix A.)

When the lift of the centerbody was taken into account, integrations of wing lift from the pressure distribution data agreed well with the lift measured by the force balance. A potential-flow panel method code was used to approximate the centerbody lift. Since the distribution of lift on the centerbody was unknown, its effect on $\bar{s}$, $\Gamma_o$, $\bar{b}/2$, and $\bar{d}$ is not included.

***Trailing-wing rolling-moment data.*** Averaged trailing-wing rolling-moment data were significantly influenced by vortex meander in both test facilities. In the wind tunnel, vortex meander increased from an amplitude of about $0.02s$ at $x/s = 1$ to about $0.2s$ at $x/s = 11$. In the water tank, meander amplitude ranged from negligible at $x/s = 11$ to at least $0.13s$ at $x/s = 70$. As a result of this meander, the model was not centered steadily in the vortex, and thus $C_{l,\mathrm{AV}}$ data falsely indicated rapid vortex decay with downstream distance because the long averaging period and increasing meander effectively enlarged the spatial averaging zone. In both test facilities, the meander amplification was well beyond that expected in calm air, possibly because of ambient turbulence or the enclosing walls of each test facility. (See appendix B for a discussion of the meander amplification.) The choice of a shorter averaging period was thus entirely arbitrary since the average $C_{l,\mathrm{TW}}$ would correlate with a full-scale roll upset only under similar meander conditions.

To illustrate the length of the rolling-moment averaging periods, the water tank and wind tunnel averaging periods can be scaled such that the VTW represents a full-scale transport airplane. Doing so yields full-scale periods of 18 and 64 sec, respectively. A comparison of these averaging periods with the typical 1- to 3-sec period of a vortex encounter shows that the experimental averaging periods are far from characteristic aircraft roll response times. In comparison, the peak rolling-moment data contained fluctuations with a period analogous to about 0.05 sec at full scale. Thus, $C_{l,\mathrm{PK}}$ can be expected to provide a better measure than $C_{l,\mathrm{AV}}$ of the potential roll upset for calm-air conditions. Because the predominant meander period was long (equivalent to the Crow instability period in the water tank), the relatively short response time for $C_{l,\mathrm{PK}}$ data allowed consistent $C_{l,\mathrm{PK}}$ values to be obtained for a given tangential velocity profile regardless of meander level. Therefore, $C_{l,\mathrm{PK}}$ data (where available) will be used over $C_{l,\mathrm{AV}}$ data in evaluating attainment of downstream alleviation by a VTW configuration.

***Wake velocity data.*** Several factors influenced the accuracy and applicability of the wake velocity data measured in the wind tunnel. Two factors which affected the measured velocity near the vortex core were oscillations of the hot-film probe and vortex meander. Probe oscillation effects were negated by the 100 point per $0.02s$ spatial averaging technique applied to the data; however, vortex meander effectively increased the spatial averaging of the velocity and vorticity profiles. Because vortex meander increased with downstream distance, the measured vorticity profiles at both $x/s = 6$ and $x/s = 11$ were significantly reduced and distorted. Thus, as it did for averaged trailing-wing rolling-moment data, meander amplification caused the wake velocity data to falsely portray rapid vortex decay with downstream distance. Another factor that influenced the accuracy of the complete cross plane of velocity data was a right-to-left wing flow angularity which caused the vertical VTW mounting blade to shed its own wake into the cross plane beyond $x/s = 1$. In view of these contaminations, the wake velocity data were quantitatively accurate within 10 to 20 percent only at $x/s = 1$. At $x/s = 6$ and 11, these data must be taken as qualitative and were useful primarily in judging whether complete merger of multiple vortices within the wake had occurred.

## Predicted and Measured Vortex Wake Development

This discussion addresses correlation of the VTW span load with vortex wake development.

Comparisons of the measured vorticity data and predicted vorticity distributions based on both measured and predicted span loads are made at $x/s = 1$. One objective is to determine if wake development can be characterized accurately using relatively simple techniques to predict span load distribution and vortex wake roll up. A second, more specific objective is to evaluate the degree of similarity between wind tunnel and water tank VTW configurations chosen to match the span load of $VTW7S_0$ (the configuration utilizing spoilers for downstream wake alleviation).

First, to establish that the vorticity measurements at $x/s = 1$ were in correspondence with the span load measurements and that significant contamination had not yet resulted from wind tunnel flow asymmetries, a vortex blob code was utilized to predict wake development with the measured span load as input. The vortex blob technique is discussed in detail by Leonard in reference 29. As an initial condition for the blob code, the wing vorticity distribution was derived in a manner similar to that of Weston and Liu (ref. 30) by discretization of the measured span load distribution into 50 equally spaced Gaussian vortices, each having a constant vorticity dispersion radius $\beta$. The thickness of the shed vorticity sheet was then proportional to $\beta$, which was found to best represent the velocity data for all VTW configurations when set to $0.0185s$. As expected, this value was very near the wake averaging length, or the resolution limit of the data set.

As the vortex blob technique is essentially inviscid, it cannot be applied to model the wake of $VTW7S_0$ because of the turbulent and separated flow caused by the spoilers. Of the three remaining VTW configurations having measured wake velocity, $VTW7S_3$ had the most complex wake. The computation of its wake development based on the measured span load is compared with the measured vorticity field at $x/s = 1$ in figure 8. Although the inviscid nature of the roll up for the unseparated-flow VTW configurations may be considered dominant up to $x/s = 11$, comparisons of predicted and measured wake vorticity beyond $x/s = 1$ are pointless because of the unsteady nature of the flow field and the resultant effects on the measurements.

The prediction shown in figure 8(b) matches the measured data well in terms of the distribution of the residual vorticity sheet and the strengths and positions of the dominant vortices. Note that the inboard region of negative (opposite sign) vorticity is predicted from the asymmetric loading measured at wing centerline. This region is predicted as more extensive than measured because the centerline $c_\ell$ was taken as the average of measured values on either side of the center. A more realistic result of the lateral-flow angularity would be to reduce the lift across the centerline only near the centerbody ($y/s < 0.03$). The positive vorticity seen on the centerline in the plot of measured data (fig. 8(c)) is believed to have resulted from the combined vorticities shed from the VTW support blade under the influence of the lateral flow and the VTW centerbody, neither of which is modeled in the prediction. The small region of negative vorticity measured near the tip vortex was found in three of the four measured cross planes at $x/s = 1$ and resulted from sharp wingtip load changes as the rapidly developing tip vortex curled over the aft portion of the wing tip. This span load "discontinuity" was measured directly on several VTW configurations and was found by Weston on an aspect-ratio-6 wing (ref. 31). However, its small scale eluded span load measurements on most VTW configurations. This discontinuity can be modeled by cubic spline fits to the span load data at the wing tip. Although it is not shown, initialization of the blob routine with such a data set resulted in a similar portrayal of the tip vortex and negative vorticity regions at $x/s = 1$.

The overall fidelity of the comparison shown in figure 8 establishes a good correlation between VTW span load measurements and wake survey measurements at $x/s = 1$. The next step is to determine if wake development can be characterized accurately with a relatively simple span load prediction technique used to initialize a vortex blob calculation of wake roll up to $x/s = 1$. Span load distributions were computed for all VTW configurations (except those with spoilers, splines, or drag plates) with the vortex lattice program of reference 32. The VTW span load distribution was modeled for the vortex lattice code as 420 horseshoe vortices on a semispan with 10 horseshoe vortices per wing segment. Each segment was given a local angle of attack, representing the wing twist ($\Delta\alpha$), and the centerline angle of attack was added all along the semispan. All comparisons of the measured and predicted span loads utilized a vortex lattice centerline angle of attack chosen to match the lattice-predicted $C_L$ with the pressure-integrated $C_{L,p}$ rather than with the force-balance-measured $C_L$. This choice allowed a comparison of the measured and predicted $dc_\ell/dy$ (which is directly related to the strength of the vorticity shed at the wing trailing edge) since neither the lattice-predicted $C_L$ nor the pressure-integrated $C_{L,p}$ included the centerbody lift that was embodied in the force-balance-measured $C_L$.

Figure 9 presents a comparison of predicted and measured spanwise vorticity distributions at the trailing edge for four VTW configurations. Wake velocity surveys were made behind three of these. No

velocity survey was made behind VTW2, which is included in the comparison because it exhibited the sharpest span load gradients of all the VTW configurations tested. In the figure, measured $dc_\ell/d(y/s)$ values were derived from linear point-to-point span load slopes and assigned at the midpoints of $y$-station data pairs, whereas predicted $dc_\ell/d(y/s)$ values were output from a 51-point (equally spaced) cubic spline fit to the lattice span load prediction at 42 equally spaced semispan positions.

It appears from figure 9 that the lattice technique is capable of providing a realistic assessment of spanwise vorticity distribution at the wing trailing edge. As would be expected, the largest discrepancies occurred at the high-gradient regions of the span load. These discrepancies are probably attributable to the truly three-dimensional nature of wing flow and thus of span load development. The obviously three-dimensional span load "discontinuity" caused by the wing-tip vortex for VTW2 is, of course, not predicted by the lattice technique. A question remains as to whether these types of discrepancies are significant when wake initiation is computed with a spatial resolution on the order of $0.02s$, the wake averaging length.

The lattice predictions evaluated in figure 9 were utilized with the vortex blob technique to predict the vortex wake development to $x/s = 1$ for VTW4, VTW7, and VTW7S$_3$. These results are compared with the corresponding vorticity measurements in figure 10. The overall characterization of wake development, including vorticity distribution and magnitude, is seen to be very good. Even the multiple concentrations of vorticity, which are believed to be due to the 1° wing segment twist discontinuities of the VTW4 configuration, are predicted well. These comparisons are meaningful only at and above the spatial resolution limit of the data, which was determined by the 100-point averaging technique and the spatial averaging caused by vortex meander. At $x/s = 1$, these combined effects produced a spatial resolution limit of about $0.02s$ to $0.04s$. At scales smaller than this, the vortex blob prediction is artificially forced to match the averaged vorticity field by the choice of a vorticity sheet thickness parameter $\beta$ that is proportional to the spatial averaging length of the experimental measurements.

The wind tunnel and water tank tests each utilized VTW configurations that were twisted slightly differently in attempts to match the expected span load of VTW7S$_0$. Incomplete span load data at the time of the tests necessitated these approximations and resulted in VTW7S$_2$ being tested in the water tank and VTW7S$_3$ being tested in the wind tunnel. Of these three configurations, span load measurements were obtained only on VTW7S$_0$ and VTW7S$_3$. As shown in figure 11, the differences between the three configurations in terms of their measured and expected vorticity distributions at the wing trailing edge are minor.

## Effects of Continuous Span Load Distributions

***Aerodynamic data.*** Figure 12 compares the aerodynamic data of VTW configurations in group I—continuous span load distributions. All four configurations were below stall at the $C_L = 0.6$ test condition, and interestingly, considering the wide variation in span loads between the configurations, all exhibited about the same measured drag level at $C_L = 0.6$. This result was verified in the water tank (see table VII), where VTW1 (the untwisted wing) and VTW4 (the tapered span load configuration) had essentially identical $C_D$ measurements at $C_L = 0.6$.

***Span load data.*** As can be seen in figure 13, the vortex-lattice-predicted span loads compare favorably with the measured span loads, with major discrepancies occurring only at the wing tip of VTW1, VTW2, and VTW3, and the wing centerline of VTW4. Vortex lattice underprediction at the wing tip was caused by the rapid roll up and passage of the tip vortex over the aft portion of the wing tip. Examination of the most outboard chordwise $c_p$ data (ref. 28) showed that the wing-tip vortex influenced the last half of the wing chord. Over prediction at the wing centerline of VTW4 was probably due to centerbody influence at the high angle of attack of this configuration. Because VTW4 had the largest negative discrepancy between measured $C_L$ and $C_{L,p}$ (table V) and because the lattice prediction was quite good for $y/s \geq 0.2$, the actual inboard span load was probably greater than that shown because of unaccounted-for chordwise pressure forces and centerbody lift.

Two of these configurations, VTW1 and VTW4, were investigated in the water tank test. The major differences in their span loads can be noted in figure 13 and table VI. Essentially, VTW1 represents a span load which is between elliptic and rectangular distributions, whereas the VTW4 span load lies near a parabolic distribution in terms of its $\bar{b}/2$ and $\Gamma_o$, but has approximately linear regions of span load similar to those found with triangular loading. Total angular momentum shed into the semispan wake, as determined by $\Gamma_o$, was considerably greater for VTW4. However, the distribution of this momentum, indicated by $\bar{d}$, should be substantially more diffused in the fully rolled-up wake. As expected,

the centroidal lift position $\bar{s}$ was about 13 percent less for VTW4 than for VTW1 and indicated a corresponding drop in wing root bending moment.

***Trailing-wing rolling-moment data.*** As shown in figure 14, the tapered span load of VTW4 presents a significantly reduced rolling moment to a small trailing wing when compared with the untwisted VTW1 configuration. Peak rolling-moment data in the wake of VTW4 exhibit a nearly level trend, whereas $C_{l,\mathrm{PK}}$ data for VTW1 decay slowly from 48 to 38 percent above those of VTW4 from $x/s = 11$ to $x/s = 70$. Thus the vorticity dispersion in the wake, rather than the total circulation, was the dominant parameter in characterizing the roll upset potential for a small wing. This result is reasonable considering that the smallest vorticity dispersion radius for any VTW span load was comparable to the trailing-wing semispan. Vorticity dispersion is not strictly an invariant of the wake (ref. 11); indeed, the slow $C_{l,\mathrm{PK}}$ decay for VTW1 is indicative of an increasing vorticity dispersion radius with downstream distance. However, for the span loads of group I the vorticity dispersion radius can be expected to accurately depict vorticity distribution following initial roll up. In fact, the correlation between $C_{l,\mathrm{PK}}$ and dispersion holds up over the small downstream distances in the wind tunnel for all four VTW configurations, a fact not necessarily expected for $C_{l,\mathrm{AV}}$ measurements as the meander amplitudes approach dispersion radii levels.

Comparing $C_{l,\mathrm{PK}}$ and $C_{l,\mathrm{AV}}$ data merely substantiates that $C_{l,\mathrm{AV}}$ data are unreliable as a measure of rolling moment. This unreliability is especially noticeable in the wake of VTW4, where $C_{l,\mathrm{AV}}$ drops 60 percent while $C_{l,\mathrm{PK}}$ remains essentially constant over $11 \leq x/s \leq 70$. Comparing the wind tunnel and water tank $C_{l,\mathrm{AV}}$ data at $x/s = 11$ again points out the higher meander level, and thus lower $C_{l,\mathrm{AV}}$ measurements, in the wind tunnel at this downstream distance.

This group of configurations illustrates the significant wake alleviation attainable through span load alteration alone. A comparison of the VTW1 and VTW4 configurations shows that VTW4 achieved a 27-percent reduction in $C_{l,\mathrm{PK}}$ at $x/s = 70$ while maintaining essentially identical drag and reducing the wing root bending moment by 13 percent. In this case, $C_{l,\mathrm{PK}}$ was reduced on the small trailing wing by more uniform vorticity shedding at the VTW trailing edge. This more uniform shedding resulted in greater vorticity dispersion in the developed wake. The limiting case for this type of wake roll up with simple span loads is triangular loading. (See table VI(b).) Although the vorticity dispersion for VTW1 was tighter than that for an elliptical span load, it was probably not unlike the dispersion local to vortices originating at the discontinuous, high-lift flap systems of modern jet transport aircraft. Thus, a significant level of wake alleviation for small encountering aircraft appears possible on future air transport aircraft if the span load is tailored to increase vorticity dispersion in the wake.

Increasing the vorticity dispersion radius in the wake through this type of span load alteration incurs a significant increase in total angular momentum (i.e., $\Gamma_o$) shed into the semispan wake, and thus implies an increased roll upset threat to encountering aircraft with semispans much larger than the vortex generator vorticity dispersion radius $\bar{d}$. Although it is true that $C_{l,\mathrm{TW}}$ for a relatively large vortex-encountering airplane will theoretically increase directly with vortex generator $\Gamma_o$, the corollary that the upset will increase correspondingly is not well established. Since it is not within the scope of this report to address vortex hazard correlation, it must suffice to state that because the inertia and energy relationships between a small aircraft intercepting a large aircraft's wake and a medium-size aircraft intercepting a large aircraft's wake are entirely different, it may be expected that the dynamic interaction between the wake and the encountering aircraft may be significantly different.

***Wake velocity data.*** Figures 15 and 16 display the wake survey data for VTW4 as vorticity contour maps at the three wind tunnel downstream measurement cross planes and as averaged $u$ and $w$ velocity profiles through localized vorticity concentrations at $x/s = 1$. Roll up is seen to proceed from a sheet at $x/s = 1$ (fig. 15(a)) with several vorticity concentrations due to the 1° increments in wing twist to a semispan wake at $x/s = 11$ (fig. 15(c)) with its dominant vortex outboard and a residual vorticity concentration inboard. Velocity profiles at $x/s = 1$ portray relatively tight vortices with axial flow deficits. Turbulence levels, inferred by $\sigma_w$ and $\sigma_u$ (fig. 16), are seen to be negligible outside vortex cores, whereas the high peaks at the cores result from the combined effects of the high-level velocity gradient, hot-film probe oscillation, and vortex meander. As noted previously, the inboard negative vorticity at $x/s = 1$ was possibly due to the centerline wing lift asymmetry, whereas the positive vorticity on the centerline is believed to be shed from both the VTW blade support, under the influence of the lateral flow angularity, and the VTW centerbody.

## Effects of Partial-Span-Flap Span Load Distributions

***Aerodynamic data.*** Figure 17 compares the aerodynamic data of the three VTW configurations that

simulate flapped-wing span loads by outboard wing twist and effectively model 40-, 60-, and 80-percent flapped wings. Each configuration exhibited the same lift curve slope and avoided wing stall until beyond the $C_L = 0.6$ test condition. Stall occurred at the lowest angle of attack for VTW6 because its local angle of attack ($\alpha+\Delta\alpha$) at the wing tip was 2° and 3° higher than those of VTW7 and VTW5, respectively. Since the outboard wing panel stalled first, the configuration with the least outboard twisted wing area, VTW7, had the highest $C_L$ at stall.

***Span load data.*** The vortex-lattice-predicted span loads compare well with the measured span loads in figure 18 except at the wing-tip and wing centerline locations, where lateral flow angularity, centerbody influence, and three-dimensional wing flow effects were present. VTW7 (the 80-percent flapped-wing configuration) was tested in both facilities and was utilized as a baseline configuration against which alleviation attained by group III configurations was referenced. As seen in table VI(a), of the three flapped-wing configurations, VTW7 had the smallest $\Gamma_o$ and $\bar{d}$, but the largest $\bar{b}/2$ and $\bar{s}$.

***Trailing-wing rolling-moment data.*** Peak rolling-moment data in figure 19 indicate a tightly rolled-up wake with little decay over $11 \leq x/s \leq 70$ for VTW7. In fact, merger of the flap and tip vortices between $x/s = 11$ and $x/s = 40$ increased the $C_{l,\mathrm{PK}}$ measurement slightly. By $x/s = 70$, $C_{l,\mathrm{PK}}$ for VTW7 (the 80-percent flapped-wing configuration) was 20 percent below that of VTW1 (the untwisted wing) and 9 percent above that of VTW4 (the tapered span load configuration). Average rolling-moment data in the water tank were taken only for the tip vortex of VTW7 and showed a relatively level trend during flap and tip vortex merger, followed by a decreased value at $x/s = 70$ due to meander. In the wind tunnel, only one maximum $C_{l,\mathrm{AV}}$ could be discerned because of the proximity of the merging flap and tip vortices. Wind tunnel and water tank $C_{l,\mathrm{AV}}$ data were identical at $x/s = 11$ for VTW7, perhaps because flow field fluctuations at this point are governed largely by the merging of the wing-tip and flap vortex systems rather than by the customarily higher background turbulence levels of the wind tunnel.

***Wake velocity data.*** Wake initiation and development for VTW7 are shown in figures 20 and 21. The qualitative value of the vorticity cross planes at $x/s = 6$ and $x/s = 11$ becomes apparent in judging the approaching merger of the wing-tip and flap vortices. Although the vorticity magnitudes are severely understated at these locations, the positions of peak vorticity should be relatively accurate. Radial distances between the two peaks decreased nearly linearly with downstream distance and implied complete merger by about $x/s = 20$. This finding is in agreement with water tank trailing-wing data, as are the relative positions of the flap and wing-tip vortices at $x/s = 11$. (By $x/s = 11$ the flap and wing-tip vortices had rotated about 250° counterclockwise with respect to each other relative to their position at $x/s = 1$.)

It is interesting to note that of the four VTW configurations with wake velocity data, VTW7 had the lowest $\Gamma_o$ and the highest $\bar{b}/2$ and therefore would be expected to exhibit the lowest rate of vorticity convection from wing centerline into the wake survey cross plane. This expectation was borne out in the vorticity cross planes, as VTW7 showed little evidence of centerline vorticity convection from the VTW support blade or VTW centerbody, and was also supported by a low $\Gamma/\Gamma_o$ trend and an initially high $\bar{y}/(\bar{b}/2)$ measurement. (See appendix B.)

## Effects of Alleviated Vortex Wake Configurations

VTW7, the 80-percent flapped-wing configuration, is used as a baseline unalleviated vortex wake configuration, and VTW7$S_0$, the 80-percent flapped wing with spoilers, is used as a baseline alleviated vortex wake configuration. Size and position of the spoilers were chosen as compromises based on results from several 4- by 7-Meter Tunnel investigations. (See refs. 7, 33, and 34.) Generally, the downstream wake alleviation achieved with VTW7$S_0$ was investigated by using several VTW configurations to study the effect of span load alteration alone and one VTW configuration to test the effect of adding drag and turbulence without span load alteration. Additional VTW configurations used splines or drag plates along with span load alteration to investigate the interrelation of incremental drag, turbulence, and span load with respect to wake alleviation. As shown in table II, three VTW configurations were tested only in the wind tunnel and two were tested only in the water tank. As noted earlier, the similarity of the initial vorticity distributions for the VTW7$S_2$ and VTW7$S_3$ configurations would make their downstream wakes similar, and therefore, these configurations are treated as equivalent in this section of the discussion.

***Aerodynamic data.*** Figure 22(a) compares the aerodynamic data for the baseline unalleviated and the spoiler-alleviated configurations. The spoilers produced the typical effects of local separated flow: a

reduction in both lift curve slope and maximum lift capability with a substantial increase in drag for a specified lift. As listed in table VII, at $C_L = 0.6$ the $C_D$ increased from VTW7 to VTW7S$_0$ by 0.056 in the wind tunnel and 0.066 in the water tank. The drag for VTW7S$_0$ is thus about 190 percent greater than that for VTW7.

The VTW7S$_0$ span load was matched by wing twist alone with the VTW7S$_1$, VTW7S$_2$, and VTW7S$_3$ configurations. Aerodynamic data for these configurations are presented in figure 22(b). Because these configurations matched span load without the addition of splines or drag plates, the $C_D$ increase referenced against that of VTW7 was typically 0.01 or less at $C_L = 0.6$ and yielded an increase of about 30 percent in total drag. The effect on the aerodynamic data of VTW7S$_3$P caused by installation of the drag plates on VTW7S$_3$ is shown in figure 22(c). The drag plates were sized to increase the VTW7S$_3$ drag to near that of VTW7S$_0$. An extra $C_D$ increase of 0.044 resulted, for a total drag increase of 170 percent relative to that of VTW7.

Two water-tank-tested VTW configurations used splines sized to produce a drag increase equivalent to that caused by the spoilers with the VTW at zero lift. (This drag increase was smaller than that produced by the drag plates.) Splines were added to the twist distribution of VTW7 to produce VTW7X. The $C_D$ was thus increased by 0.027 at $C_L = 0.6$ to produce an increase in drag of about 90 percent relative to that of VTW7. Splines were added to the twist distribution of VTW7S$_2$ to produce VTW7S$_2$X. This addition increased $C_D$ by 0.026 and resulted in a total $C_D$ increase of 110 percent over that of VTW7. Since no increase in angle of attack was required to maintain $C_L = 0.6$ with the splines, it is surmised that they were sufficiently aft of the VTW trailing edge and aligned with the flow that they did not significantly alter the VTW span load near $C_L = 0.6$.

***Span load data.*** Figure 23(a) shows the span load data for VTW7S$_0$ and illustrates the effect of spoilers on VTW7. The $c_\ell$ was essentially halved at $y/s = 0.6$ because of the spoiler installation. This decrease forced an increase in $\Gamma_o$ to maintain $C_L = 0.6$ and a corresponding decrease in $\bar{b}/2$ to maintain the net impulse $(\bar{b}/2)\Gamma_o$. Notice that the loading around the wing tip was increased slightly because of the higher angle of attack required to maintain $C_L = 0.6$. This increase suggests that the wing-tip vortex should, at least initially, be more intense for VTW7S$_0$ than for VTW7. Not only did $\Gamma_o$ increase and $\bar{b}/2$ decrease by 19 percent, as shown in table VI(a), but the vorticity dispersion radius was also more than doubled in the transformation of VTW7 to VTW7S$_0$.

Figures 23(b), (c), and (d) present the measured and/or predicted span loads of VTW configurations that utilized wing twist alone to match the VTW7S$_0$ measured span load. Other than a failure of VTW7S$_2$ and VTW7S$_3$ to duplicate the outboard side of the spoiler $c_\ell$ "trough," these span loads approximate the VTW7S$_0$ span load well and match its dominant wake initiation parameters $\Gamma_o$, $\bar{b}/2$, and $\bar{d}$ within 2.5 percent.

The addition of drag plates to VTW7S$_3$ required an extra 0.3° $\alpha$ to maintain $C_L = 0.6$ and thus more substantially altered the VTW7S$_3$P span load from that of VTW7S$_0$, as seen in figure 23(e). In this case, values given in table VI(a) for $\Gamma_o$ and $\bar{b}/2$ varied 4 percent from those of VTW7S$_0$. Figures 23(f) and (g) portray the expected span loads for VTW7S$_2$X and VTW7X, respectively, assuming the splines do not influence their span loads. Measured span load data are not available, since neither configuration was evaluated in the wind tunnel.

***Trailing-wing rolling-moment data.*** Figure 24(a) establishes the downstream $C_{l,\mathrm{TW}}$ reduction accomplished by the addition of spoilers to the 80-percent flapped-wing configuration. In terms of $C_{l,\mathrm{PK}}$ measurements, a 31-percent reduction was achieved by $x/s = 70$. These results are consistent with $C_{l,\mathrm{AV}}$ measurements obtained over shorter downstream distances by Croom (ref. 33). Note that the alleviated configuration, VTW7S$_0$, initially had higher $C_{l,\mathrm{TW}}$ data in both facilities (as expected based on the span load measurements), but the crossover of $C_{l,\mathrm{AV}}$ between VTW7S$_0$ and VTW7 in the wind tunnel over $6 < x/s < 11$ did not occur in the water tank for either $C_{l,\mathrm{PK}}$ or $C_{l,\mathrm{AV}}$ until $11 < x/s < 40$. This difference is an indication of the possible effect that variations in turbulence and meander levels between facilities can have on $C_{l,\mathrm{AV}}$ data.

Figure 24(b) shows the effect on downstream wake alleviation caused by matching the span load of VTW7S$_0$ without the high drag and turbulence of the spoilers. The $C_{l,\mathrm{PK}}$ data for VTW7S$_2$ indicate that the multiple vortex wake structure that now exists (in place of the predominant single semispan vortex of VTW7S$_0$) proceeds to $x/s = 70$ without complete merger. Since the wing-tip vortex of VTW7S$_0$ is well away from the spoiler region, it would be expected that the wing-tip vortices of VTW7S$_0$ and VTW7S$_2$ would initially be equivalent. This expectation is verified by the $C_{l,\mathrm{PK}}$ data at $x/s = 11$. The fact that the inboard vortex (originating from the inboard portion of the semispan) of VTW7S$_2$ also initiates with an identical $C_{l,\mathrm{PK}}$ strength was fortuitous. By $x/s = 70$, the predominant outboard vortex of VTW7S$_2$ was registering an 11 percent $C_{l,\mathrm{PK}}$

reduction relative to that of VTW7, or about one-third of the alleviation obtained with the spoilers. This small reduction of the wing-tip vortex intensity relative to that of VTW7 may be due to slightly higher vorticity diffusion created by the turbulence from the mutually shearing vortices in the multiple-vortex wake.

Figure 24(c) compares the $C_{l,\mathrm{TW}}$ data for the baseline unalleviated and alleviated configurations (VTW7 and VTW7$S_0$) with those obtained for VTW configurations using the splines or drag plates to simulate the drag and turbulence effects of the spoilers. The addition of splines to VTW7$S_2$ (configuration VTW7$S_2$X) produced, at the initial downstream location, $C_{l,\mathrm{PK}}$ data for both the inboard and outboard vortices that were below $C_{l,\mathrm{PK}}$ data for either VTW7$S_0$ or VTW7. The wake of VTW7$S_2$X continued to decay until about $x/s = 40$, and by $x/s = 70$ there was no discernible inboard vortex and the $C_{l,\mathrm{PK}}$ was slightly lower than that obtained for VTW7$S_0$. Thus, the splines in conjunction with the matched span load appear to have created a downstream wake similar to that of the spoiler-alleviated configuration. The lower incremental drag and turbulence of the splines may account for the longer time required for the decay of the inboard vortex system, because the remnants of this system may have merged into the complete vortex system to yield no $C_{l,\mathrm{PK}}$ decay along $40 < x/s < 70$. An examination of relative vortex positions within the wakes of VTW7$S_2$ and VTW7$S_2$X shows the increased likelihood of merger of the VTW7$S_2$X inboard vortex since, by $x/s = 40$, the displacement between the inboard and wing-tip vortices for VTW7$S_2$X was about half that for VTW7$S_2$. Decay rates beyond $x/s = 70$ are unknown; however, the equivalence of both $C_{l,\mathrm{PK}}$ and $C_{l,\mathrm{AV}}$ data between VTW7$S_0$ and VTW7$S_2$X would require comparable meander levels and, therefore, similar turbulence levels in each wake.

Since the incremental drag and turbulence plus span load matching of VTW7$S_2$X replicated the downstream wake alleviation of VTW7$S_0$ (the 80-percent flapped wing with spoilers), whereas the VTW7$S_2$ configuration (which used wing twist alone to match the VTW7$S_0$ span load) achieved little downstream alleviation, how important a role was span load playing in the spoiler-attained alleviation? To determine if the incremental drag and turbulence of the spoilers were the key parameters in the alleviation obtained with the VTW7$S_0$ configuration, $C_{l,\mathrm{PK}}$ data were taken in the wake of VTW7X. This configuration consisted of the baseline unalleviated VTW7 (80-percent flapped wing) with splines added to simulate only the drag and turbulence effects of the spoilers. Beneficial aspects of the VTW7X configuration were its lower drag and $\Gamma_o$. As shown in figure 24(c), VTW7X did indeed produce substantial wake alleviation; $C_{l,\mathrm{PK}}$ data essentially agreed with those for the predominant vortex of VTW7$S_2$X and, throughout the $x/s$ range, remained below those of VTW7$S_0$.

***Wake velocity data.*** Figures 25 and 26 present the measured vorticity cross planes and selected velocity profiles in the wake of the spoiler-alleviated configuration, VTW7$S_0$. When these measurements are compared with the corresponding data for VTW7 (figs. 20 and 21), the effect of the spoilers is apparent. As predicted by the higher wing-tip span load of VTW7$S_0$ (caused by the increased $\alpha$ to maintain $C_L = 0.6$) and by $C_{l,\mathrm{PK}}$ measurements, the wing-tip vortex of VTW7$S_0$ was initially more intense than that of VTW7. This effect is most noticeable when comparing velocity profiles of the two configurations at $x/s = 1$ (figs. 21(b) and 26(b)). Additionally, the intensity of the VTW7$S_0$ flap vortex was reduced because the local reduction in span load caused by the spoiler lowered the amount of vorticity wrapping into it. As a result, by $x/s = 6$ the VTW7$S_0$ wing-tip vortex predominated, whereas the VTW7 wake was still in the midst of a merger of the flap and wing-tip vortices. Beyond $x/s = 11$, the merger of the VTW7 wake system was completed, and a stable, plateau phase, as determined by the $C_{l,\mathrm{PK}}$ data, resulted until at least $x/s = 70$. However, the wake of VTW7$S_0$ decayed significantly beyond $x/s = 6$ as the effect of the spoilers on wake development was incurred.

The substantial drag and turbulence associated with the spoilers were manifested in the wake in several ways. Most obvious was the broad region of unsteady flow aft of the spoiler location, as exemplified by the high $\sigma_w$ and $\sigma_u$ measurements at $x/s = 1$ (fig. 26(d)). This turbulence field shows up in the $x/s = 1$ vorticity plane as very diffused and spread regions of positive and negative vorticity emanating from either side of the spoiler-induced $c_\ell$ trough. The diffused characterization of these regions was partially a result of the increased spatial averaging produced by the highly unsteady nature of the flow field here. Apparent also in figure 26(d) is the substantial axial velocity ($u$) deficit created downstream of the spoilers. This velocity deficit is representative of the unfavorable pressure gradient produced by the high drag of the spoilers.

Thus, the spoilers introduced three basic mechanisms capable of contributing to the significant decay of the VTW7$S_0$ wake beyond $x/s = 6$. Besides the change in span load, two direct inputs of the spoilers were high turbulence, which increased the otherwise laminar rate of vorticity diffusion, and increased

drag, which caused a positive axial pressure gradient that tended to counteract the convective concentration of the vorticity sheet. The role of span load alteration in the downstream alleviation of VTW7$S_0$ appears minimal, as is demonstrated by comparing the trailing-wing measurements behind VTW7$S_2$ (which simulated only the span load alteration of the spoilers) and those behind VTW7X (which simulated only the incremental drag and turbulence of the spoilers).

In marked contrast to the highly diffused vorticity concentrations aft of the spoilers on VTW7$S_0$, highly concentrated vortices were created from both sides of the $c_\ell$ trough on VTW7$S_3$. (See figs. 27 and 28.) These vortices were produced by wing twist alone. As was noted with the water tank trailing-wing data through $x/s = 70$ and suggested in the wind tunnel by the enlarging displacement between vortices with increasing $x/s$, this multiple vortex wake persisted far downstream. The similarity between VTW7$S_0$ and VTW7$S_3$ wing-tip and residual flap vortices at $x/s = 1$ and the similarity of their combination at $x/s = 6$ mean that the spoiler wake has as yet had little effect on this portion of the VTW7$S_0$ vortex system. This is in good agreement with identical $C_{l,\mathrm{PK}}$ measurements for both VTW7$S_0$ and the wing-tip vortex of VTW7$S_2$ at $x/s = 11$ in the water tank. A significant decay then ensues in the wake of VTW7$S_0$, apparently as a result of the spoiler wake and the wing-tip vortex wrapping together. Once this occurs, the turbulence and axial deficit imparted to the flow field by the spoiler act to dissipate the wing-tip vortex system.

The addition of splines to VTW7$S_2$ (creating VTW7$S_2$X) produced a near-field reduction in $C_{l,\mathrm{PK}}$ measurements for both the wing-tip and inboard vortex systems. This effect is similar to the $C_{l,\mathrm{AV}}$ reduction between the wakes of VTW7$S_3$ and VTW7$S_3$P that was caused by installation of the drag plates. Whether this reduction resulted from a more rapid initial decay due to turbulent diffusion of vorticity or from an impaired concentration of the vorticity sheet because of the added drag is unknown. However, the effect was clearly independent of the inboard vortex system since the wing-tip vortex $C_{l,\mathrm{PK}}$ data essentially matched for both configurations with splines—VTW7X, which produced only an outboard vortex system, and VTW7$S_2$X, which produced both an inboard and an outboard vortex system.

Thus, the downstream wake alleviation attained by VTW7$S_0$ resulted directly from the incremental drag and turbulence associated with the spoilers. The span load alteration caused by the spoilers is seen to play no part in the development of the alleviation for this particular configuration.

## Concluding Remarks

Several measurement techniques in two different test facilities were used to provide a comprehensive and interrelated set of wing and wake measurements in the variable twist wing investigation. Detailed wing and near-wake data were obtained in a wind tunnel, and trailing-wing surveys of the near- and far-downstream wake were obtained in a water tank. A total of 14 different wing configurations were tested at the same Reynolds number and lift coefficient in each facility.

The variety of measurements allowed results to be correlated and their accuracy to be checked between test facilities as well as between wing and wake measurements. As a result of these correlations, several facility and measurement technique effects were found to have significantly influenced portions of either the vortex wake roll up or the experimental quantification of vortex wake intensity. Detailed wind tunnel measurements of both span load distributions on the wing and cross plane wake velocities at a semispan downstream correlated well with each other and with water tank measurements of peak trailing-wing rolling moments. These detailed measurements were used to show that inviscid analytical prediction techniques accurately portrayed the vortex generator span load distribution and initial vortex wake development to the resolution limits of the data. However, meander and flow angularity in the wind tunnel prevented, in other than a qualitative sense, the use of wake velocity data measured at 6 and 11 semispans downstream. Average trailing-wing rolling moments were shown to be unreliable as a measure of the vortex intensity because vortex meander amplification did not scale between the test facilities and free-air conditions. High values of meander amplification caused average trailing-wing rolling-moment data in both facilities, as well as wake velocity data in the wind tunnel, to falsely indicate rapid vortex decay with downstream distance.

A tapered-span-load configuration, which exhibited little or no drag penalty, was shown to offer significant downstream wake alleviation to a small trailing wing. This wing configuration achieved wake alleviation through span load specification of more uniform vorticity shedding at the wing trailing edge. In contrast, the greater downstream wake alleviation achieved with the addition of spoilers to a flapped-wing configuration was shown to result directly from the high incremental drag and turbulence associated with the spoilers and not from the span load alteration they caused.

TABLE I. PRESSURE ORIFICE LOCATIONS ON THE VARIABLE TWIST WING

| Span locations | |
|---|---|
| Wing segment | $y/s$ |
| 0-L[a] | -0.0612 |
| 0-R[a] | .0612 |
| 1 | .1560 |
| 3 | .2037 |
| 5 | .2513 |
| 7 | .2989 |
| 9 | .3465 |
| 13 | .4418 |
| 15 | .4894 |
| 17 | .5370 |
| 19 | .5846 |
| 21 | .6322 |
| 23 | .6798 |
| 25 | .7275 |
| 27 | .7751 |
| 29 | .8227 |
| 31 | .8703 |
| 33 | .9179 |
| 35 | .9656 |
| 36 | .9894 |

| Chord location | |
|---|---|
| $x_{LE}/c$ | $\pm z/c$ |
| 0 | 0 |
| .0125 | .01894 |
| .0250 | .02615 |
| .0500 | .03555 |
| .1000 | .04683 |
| .1500 | .05345 |
| .2000 | .05738 |
| .3000 | .06001 |
| .4000 | .05803 |
| .5000 | .05294 |
| .6000 | .04563 |
| .7000 | .03664 |
| .8000 | .02623 |
| .9000 | .01448 |
| .9800 | .00403 |

[a]Left (0-L) and right (0-R) side of wing center-panel section.

TABLE II. VTW CONFIGURATIONS

| Group | Wing twist configuration designation | Configuration description | Test facility | |
|---|---|---|---|---|
| | | | Wind tunnel | Water tank |
| I Continuous span load distributions | VTW1 | Untwisted wing | √ | √ |
| | VTW2 | Approximately rectangular loading | √ | |
| | VTW3 | Maximum loading at midsemispan | √ | |
| | VTW4 | Tapered loading, maximum at centerline | √ | √ |
| II Partial-span-flap span load distributions | VTW5 | 40-percent flapped wing | √ | |
| | VTW6 | 60-percent flapped wing | √ | |
| | VTW7 | 80-percent flapped wing | √ | √ |
| III Alleviated vortex wake configurations | $VTW7S_0$ | 80-percent flapped wing with spoilers | √ | √ |
| | $VTW7S_1$ | Wing twisted to approximately match span load of $VTW7S_0$ (version 1) | √ | |
| | $VTW7S_2$ | Wing twisted to approximately match span load of $VTW7S_0$ (version 2) | √ | √ |
| | $VTW7S_3$ | Wing twisted to approximately match span load of $VTW7S_0$ (version 3) | √ | |
| | $VTW7S_3P$ | $VTW7S_3$ with drag plates | √ | |
| | $VTW7S_2X$ | $VTW7S_2$ with splines | | √ |
| | VTW7X | VTW7 with splines | | √ |

TABLE III. VTW TWIST DISTRIBUTIONS

[$\Delta\alpha$ is given with respect to wing center panel; wing segment leading edge up is positive]

| Wing segment | Inboard edge, $y/s$ | $\Delta\alpha$, deg, for wing configurations— | | | | | | | | | | | | | |
|---|---|---|---|---|---|---|---|---|---|---|---|---|---|---|---|
| | | VTW1 | VTW2 | VTW3 | VTW4 | VTW5 | VTW6 | VTW7 | VTW7$S_0$ | VTW7$S_1$ | VTW7$S_2$ | VTW7$S_3$ | VTW7$S_3$P | VTW7$S_2$X | VTW7X |
| Centerline | 0 | 0 | 0 | 0 | 0 | 0 | 0 | 0 | 0 | 0 | 0 | 0 | 0 | 0 | 0 |
| 1 | .1429 | ↓ | ↓ | 2.0 | −1 | ↓ | ↓ | ↓ | ↓ | ↓ | ↓ | ↓ | ↓ | ↓ | ↓ |
| 2 | .1667 | ↓ | ↓ | ↓ | −1 | ↓ | ↓ | ↓ | ↓ | ↓ | ↓ | ↓ | ↓ | ↓ | ↓ |
| 3 | .1905 | ↓ | ↓ | ↓ | −2 | ↓ | ↓ | ↓ | ↓ | ↓ | ↓ | ↓ | ↓ | ↓ | ↓ |
| 4 | .2143 | ↓ | ↓ | ↓ | −2 | ↓ | ↓ | ↓ | ↓ | ↓ | ↓ | ↓ | ↓ | ↓ | ↓ |
| 5 | .2381 | ↓ | ↓ | ↓ | −3 | ↓ | ↓ | ↓ | ↓ | ↓ | ↓ | ↓ | ↓ | ↓ | ↓ |
| 6 | .2619 | ↓ | ↓ | ↓ | −3 | ↓ | ↓ | ↓ | ↓ | ↓ | ↓ | ↓ | ↓ | ↓ | ↓ |
| 7 | .2857 | ↓ | ↓ | 4.0 | −4 | ↓ | ↓ | ↓ | ↓ | ↓ | ↓ | ↓ | ↓ | ↓ | ↓ |
| 8 | .3095 | ↓ | ↓ | ↓ | −4 | ↓ | ↓ | ↓ | ↓ | ↓ | ↓ | ↓ | ↓ | ↓ | ↓ |
| 9 | .3333 | ↓ | ↓ | ↓ | −5 | ↓ | ↓ | ↓ | ↓ | ↓ | ↓ | ↓ | ↓ | ↓ | ↓ |
| 10 | .3571 | ↓ | 0.5 | ↓ | −5 | −2 | ↓ | ↓ | ↓ | ↓ | ↓ | ↓ | ↓ | ↓ | ↓ |
| 11 | .3810 | ↓ | ↓ | ↓ | −5 | −4 | ↓ | ↓ | ↓ | ↓ | ↓ | ↓ | ↓ | ↓ | ↓ |
| 12 | .4048 | ↓ | ↓ | ↓ | −6 | −6 | ↓ | ↓ | ↓ | ↓ | ↓ | ↓ | ↓ | ↓ | ↓ |
| 13 | .4286 | ↓ | ↓ | 6.0 | ↓ | −7 | ↓ | ↓ | ↓ | ↓ | ↓ | ↓ | ↓ | ↓ | ↓ |
| 14 | .4524 | ↓ | ↓ | ↓ | ↓ | ↓ | ↓ | ↓ | ↓ | ↓ | ↓ | ↓ | ↓ | ↓ | ↓ |
| 15 | .4762 | ↓ | 1.0 | ↓ | ↓ | ↓ | ↓ | ↓ | ↓ | ↓ | −3.75 | ↓ | ↓ | −3.75 | ↓ |
| 16 | .5000 | ↓ | ↓ | ↓ | ↓ | ↓ | ↓ | ↓ | ↓ | ↓ | −7.50 | ↓ | ↓ | −7.50 | ↓ |
| 17 | .5238 | ↓ | ↓ | ↓ | ↓ | ↓ | ↓ | ↓ | ↓ | −15 | −11.25 | −15.00 | −15.00 | −11.25 | ↓ |
| 18 | .5476 | ↓ | ↓ | ↓ | ↓ | ↓ | ↓ | ↓ | ↓ | −15 | −15.00 | −15.00 | −15.00 | −15.00 | ↓ |

TABLE III. Concluded

[$\Delta\alpha$ is given with respect to wing center panel; wing segment leading edge up is positive]

| Wing segment | Inboard edge, $y/s$ | $\Delta\alpha$, deg, for wing configurations— | | | | | | | | | | | | | |
|---|---|---|---|---|---|---|---|---|---|---|---|---|---|---|---|
| | | VTW1 | VTW2 | VTW3 | VTW4 | VTW5 | VTW6 | VTW7 | VTW7$S_0$ | VTW7$S_1$ | VTW7$S_2$ | VTW7$S_3$ | VTW7$S_3$P | VTW7$S_2$X | VTW7X |
| 19 | .5714 | 0 | 1.0 | 4.0 | −6 | −7 | 0 | 0 | 0 | −15 | −15.00 | −15.00 | −15.00 | −15.00 | 0 |
| 20 | .5952 | ↓ | 1.5 | ↓ | −7 | ↓ | −2.0 | ↓ | ↓ | ↓ | ↓ | ↓ | ↓ | ↓ | ↓ |
| 21 | .6190 | ↓ | ↓ | ↓ | ↓ | ↓ | −4.0 | ↓ | ↓ | ↓ | ↓ | ↓ | ↓ | ↓ | ↓ |
| 22 | .6429 | ↓ | ↓ | ↓ | ↓ | ↓ | −6.0 | ↓ | ↓ | ↓ | ↓ | ↓ | ↓ | ↓ | ↓ |
| 23 | .6667 | ↓ | ↓ | ↓ | ↓ | ↓ | ↓ | ↓ | ↓ | ↓ | −11.25 | −11.25 | −11.25 | −11.25 | ↓ |
| 24 | .6905 | ↓ | ↓ | ↓ | ↓ | ↓ | ↓ | ↓ | ↓ | 0 | −7.50 | −7.50 | −7.50 | −7.50 | ↓ |
| 25 | .7143 | ↓ | 2.0 | 2.0 | −8 | ↓ | ↓ | ↓ | ↓ | ↓ | −3.75 | −3.75 | −3.75 | −3.75 | ↓ |
| 26 | .7381 | ↓ | ↓ | ↓ | ↓ | ↓ | ↓ | ↓ | ↓ | ↓ | 0 | 0 | 0 | 0 | ↓ |
| 27 | .7619 | ↓ | ↓ | ↓ | ↓ | ↓ | ↓ | ↓ | ↓ | ↓ | 0 | −3.00 | −3.00 | 0 | ↓ |
| 28 | .7857 | ↓ | ↓ | ↓ | ↓ | ↓ | ↓ | −6 | −6 | −6 | −6.00 | −6.00 | −6.00 | −6.00 | −6 |
| 29 | .8095 | ↓ | ↓ | ↓ | ↓ | ↓ | ↓ | ↓ | ↓ | ↓ | ↓ | ↓ | ↓ | ↓ | ↓ |
| 30 | .8333 | ↓ | 2.5 | ↓ | −9 | ↓ | ↓ | ↓ | ↓ | ↓ | ↓ | ↓ | ↓ | ↓ | ↓ |
| 31 | .8571 | ↓ | ↓ | 0 | −9 | ↓ | ↓ | ↓ | ↓ | ↓ | ↓ | ↓ | ↓ | ↓ | ↓ |
| 32 | .8810 | ↓ | ↓ | ↓ | −10 | ↓ | ↓ | ↓ | ↓ | ↓ | ↓ | ↓ | ↓ | ↓ | ↓ |
| 33 | .9048 | ↓ | ↓ | ↓ | −11 | ↓ | −5.5 | ↓ | ↓ | ↓ | ↓ | ↓ | ↓ | ↓ | ↓ |
| 34 | .9286 | ↓ | ↓ | ↓ | −11 | ↓ | −5.0 | ↓ | ↓ | ↓ | ↓ | ↓ | ↓ | ↓ | ↓ |
| 35 | .9524 | ↓ | 3.0 | ↓ | −12 | ↓ | −4.5 | ↓ | ↓ | ↓ | ↓ | ↓ | ↓ | ↓ | ↓ |
| 36 | .9762 | ↓ | 3.0 | ↓ | −12 | ↓ | −4.0 | ↓ | ↓ | ↓ | ↓ | ↓ | ↓ | ↓ | ↓ |
| Other devices | | | | | | | | | Spoilers | | | | Drag plates | Splines | Splines |

TABLE IV. SCOPE OF DATA RETRIEVED FOR EACH TEST FACILITY

| Facility | Model condition | VTW data | Location of downstream measurement ($x/s$) | | | | |
|---|---|---|---|---|---|---|---|
| | | | 1 | 6 | 11 | 40 | 70 |
| Wind tunnel | $\alpha$ range | Aerodynamic data | | | | | |
| | $C_L = 0.6$ | Span load and $C_D$ data | Wake velocity data | Wake velocity data | Wake velocity data | | |
| | | | | Trailing-wing $C_{l,\mathrm{AV}}$ data | Trailing-wing $C_{l,\mathrm{AV}}$ data | | |
| Water tank | $\alpha$ range (for VTW1 only) | Aerodynamic data (for VTW1 only) | | | | | |
| | $C_L = 0.6$ | $C_D$ | | | Trailing-wing $C_{l,\mathrm{AV}}$ and $C_{l,\mathrm{PK}}$ data | Trailing-wing $C_{l,\mathrm{AV}}$ and $C_{l,\mathrm{PK}}$ data | Trailing-wing $C_{l,\mathrm{AV}}$ and $C_{l,\mathrm{PK}}$ data |

TABLE V. FORCE-BALANCE-MEASURED LIFT AND PRESSURE-INTEGRATED LIFT FOR A NOMINAL $C_L = 0.6$

| Wing twist configuration | $C_L$ | $C_{L,p}$ | $\frac{C_{L,p} - C_L}{C_L}$ | $\frac{(C_{L,p} + C_{L,\mathrm{CB}}) - C_L}{C_L}$ |
|---|---|---|---|---|
| VTW1 | 0.614 | 0.580 | −0.055 | −0.030 |
| VTW2 | .601 | .575 | −.043 | −.021 |
| VTW3 | .602 | .592 | −.017 | .000 |
| VTW4 | .628 | .577 | −.081 | −.041 |
| VTW5 | .615 | .597 | −.029 | +.008 |
| VTW6 | .620 | .591 | −.047 | −.017 |
| VTW7 | .596 | .571 | −.042 | −.014 |
| $VTW7S_0$ | .591 | .555 | −.061 | −.023 |
| $VTW7S_1$ | .607 | .575 | −.053 | −.015 |
| $VTW7S_3$ | .583 | .564 | −.033 | +.007 |
| $VTW7S_3P$ | .606 | .591 | −.025 | +.015 |

TABLE VI. TWO-DIMENSIONAL SPAN LOAD CHARACTERISTICS
$[C_L = 0.6]$

(a) VTW span loads

| Wing twist configuration | $\frac{\bar{s}}{s}$ | $\frac{\Gamma_o}{U_\infty s}$ | $\frac{\bar{b}}{b}$ | $\frac{\bar{d}}{s}$ |
|---|---|---|---|---|
| VTW1 | 0.448 | 0.0975 | 0.879 | 0.12 |
| VTW2 | .469 | .0927 | .924 | .11 |
| VTW3 | .452 | .0898 | .954 | .22 |
| VTW4 | .391 | .123 | .695 | .24 |
| VTW5 | .386 | .126 | .680 | .26 |
| VTW6 | .405 | .110 | .780 | .16 |
| VTW7 | .417 | .105 | .815 | .12 |
| $VTW7S_0$ | .390 | .125 | .687 | .25 |
| $VTW7S_1$ | .389 | .124 | .691 | .25 |
| $VTW7S_3$ | .377 | .128 | .670 | .24 |
| $VTW7S_3P$ | .375 | .130 | .658 | .25 |

(b) Theoretical span loads

| Span load distribution | $\frac{\bar{s}}{s}$ | $\frac{\Gamma_o}{U_\infty s}$ | $\frac{\bar{b}}{b}$ | $\frac{\bar{d}}{s}$ |
|---|---|---|---|---|
| Rectangular | 0.500 | 0.0857 | 1.000 | 0 |
| Elliptic | .424 | .109 | .785 | .223 |
| Parabolic | .375 | .129 | .667 | .236 |
| Triangular | .333 | .171 | .500 | .289 |

TABLE VII. TRAILING-WING AND CORRESPONDING VTW DATA

[VTW $C_L = 0.6$]

| Wing configuration | Facility | $\alpha$, deg | $C_D$ | Trailing-wing position | | | $C_{l,\mathrm{PK}}$ | $C_{l,\mathrm{AV}}$ |
|---|---|---|---|---|---|---|---|---|
| | | | | $x/s$ | $y/s$ | $z/s$ | | |
| VTW1 | Wind | 7.5 | 0.028 | 6.0 | −0.910 | 0.021 | | 0.073 |
| | tunnel | 7.5 | .028 | 11.0 | −.946 | .061 | | .062 |
| | Water | 7.5 | 0.037 | 11.2 | 0.878 | 0.0 | 0.099 | 0.096 |
| | tank | ↓ | ↓ | 39.3 | .857 | −.163 | .092 | |
| | | | | 39.4 | .837 | −.163 | | .054 |
| | | | | 71.2 | .776 | −.306 | .088 | |
| | | | | 77.7 | .796 | −.306 | | .027 |
| VTW2 | Wind | 6.5 | 0.027 | 6.0 | −0.972 | −0.014 | | 0.077 |
| | tunnel | 6.5 | .027 | 11.0 | −1.018 | .005 | | .064 |
| VTW3 | Wind | 4.8 | 0.028 | 6.0 | −0.856 | 0.115 | | 0.065 |
| | tunnel | 4.8 | .028 | 11.0 | −.887 | .005 | | .052 |
| VTW4 | Wind | 12.5 | 0.028 | 6.0 | −0.847 | 0.128 | | 0.057 |
| | tunnel | 12.5 | .028 | 11.0 | −.820 | .088 | | .044 |
| | Water | 12.6 | 0.037 | 10.4 | 0.776 | 0.061 | 0.067 | |
| | tank | ↓ | ↓ | 10.0 | .776 | .061 | | 0.059 |
| | | | | 40.1 | .490 | −.327 | .065 | |
| | | | | 39.7 | .510 | −.347 | | .036 |
| | | | | 69.3 | .714 | −.878 | .064 | .023 |
| VTW5 | Wind | 11.5 | 0.027 | 6.0 | −0.896 | 0.170 | | 0.055 |
| | tunnel | ↓ | ↓ | 6.0 | −.395 | −.162 | | .050 |
| | | | | 11.0 | −.848 | .131 | | .041 |
| | | | | 11.0 | −.479 | −.323 | | .047 |
| VTW6 | Wind | 9.1 | 0.026 | 6.0 | −0.851 | 0.209 | | 0.050 |
| | tunnel | ↓ | ↓ | 6.0 | −.684 | −.036 | | .044 |
| | | | | 11.0 | −.768 | .169 | | .040 |
| | | | | 11.0 | −.844 | −.077 | | .046 |
| VTW7 | Wind | 8.5 | 0.030 | 6.0 | −0.808 | 0.047 | | 0.040 |
| | tunnel | 8.5 | .030 | 11.0 | −.833 | .056 | | .046 |
| | Water | 8.1 | 0.031 | 10.3 | 0.837 | 0 | 0.067 | |
| | tank | ↓ | ↓ | 10.6 | .827 | 0 | | 0.046 |
| | | | | 10.2 | .857 | .082 | .041 | |
| | | | | 39.4 | .714 | −.143 | .071 | .044 |
| | | | | 69.6 | .714 | −.408 | .070 | |
| | | | | 69.1 | .714 | −.408 | | .031 |

TABLE VII. Concluded

[VTW $C_L = 0.6$]

| Wing configuration | Facility | $\alpha$, deg | $C_D$ | Trailing-wing position | | | $C_{l,\mathrm{PK}}$ | $C_{l,\mathrm{AV}}$ |
|---|---|---|---|---|---|---|---|---|
| | | | | $x/s$ | $y/s$ | $z/s$ | | |
| $\mathrm{VTW7S_0}$ | Wind tunnel | 11.6 | 0.086 | 6.0 | −0.888 | 0.104 | | 0.049 |
| | | 11.6 | .086 | 11.0 | −.827 | .103 | | .035 |
| | Water tank | 11.5 | 0.097 | 11.2 | 0.714 | 0.082 | 0.074 | 0.055 |
| | | ↓ | ↓ | 38.2 | .592 | −.408 | .059 | |
| | | | | 38.9 | .571 | −.388 | | .034 |
| | | | | 70.5 | .571 | −.714 | .048 | |
| | | | | 69.6 | .571 | −.714 | | .017 |
| $\mathrm{VTW7S_1}$ | Wind tunnel | 11.4 | 0.040 | 6.0 | −0.397 | −.036 | | 0.073 |
| | | ↓ | ↓ | 6.0 | −.846 | .124 | | .056 |
| | | | | 11.0 | −.311 | −.301 | | .075 |
| | | | | 11.0 | −.933 | .045 | | .044 |
| $\mathrm{VTW7S_2}$ | Wind tunnel | 11.3 | 0.034 | 6.0 | −0.437 | −0.037 | | 0.072 |
| | | ↓ | ↓ | 6.0 | −.856 | .131 | | .055 |
| | | | | 11.0 | −.375 | −.202 | | .061 |
| | | | | 11.0 | −.911 | .087 | | .041 |
| | Water tank | 11.2 | 0.039 | 11.3 | 0.857 | 0.082 | 0.074 | 0.062 |
| | | ↓ | ↓ | 10.9 | .367 | −.225 | .077 | |
| | | | | 11.6 | .388 | −.225 | | .060 |
| | | | | 39.6 | .612 | −.204 | .064 | |
| | | | | 38.7 | .633 | −.204 | | .019 |
| | | | | 40.2 | .674 | −.898 | .047 | .025 |
| | | | | 69.9 | .388 | −1.020 | .062 | |
| | | | | 70.2 | .388 | −1.020 | | .010 |
| | | | | 70.2 | .816 | −.653 | .041 | .013 |
| $\mathrm{VTW7S_3}$ | Wind tunnel | 11.9 | 0.038 | 6.0 | 0.830 | 0.137 | | 0.057 |
| | | ↓ | ↓ | 6.0 | .379 | −.013 | | .086 |
| | | | | 11.0 | .729 | .110 | | .048 |
| | | | | 11.0 | .321 | −.264 | | .077 |
| $\mathrm{VTW7S_3P}$ | Wind tunnel | 12.2 | 0.082 | 11.0 | 0.696 | 0.112 | | 0.048 |
| | | 12.2 | .082 | 11.0 | .396 | −.237 | | .024 |
| $\mathrm{VTW7S_2X}$ | Water tank | 11.2 | 0.065 | 11.5 | 0.918 | 0.082 | 0.059 | 0.014 |
| | | ↓ | ↓ | 10.6 | .449 | −.204 | .040 | |
| | | | | 39.0 | .592 | −.408 | .044 | |
| | | | | 42.4 | .571 | −.408 | | .010 |
| | | | | 39.9 | .939 | −.653 | .021 | |
| | | | | 69.3 | .612 | −.653 | .044 | |
| | | | | 69.0 | .633 | −.653 | | .013 |
| VTW7X | Water tank | 8.1 | 0.058 | 10.7 | 0.796 | 0.061 | 0.061 | |
| | | ↓ | ↓ | 11.1 | .776 | .041 | | 0.043 |
| | | | | 40.4 | .755 | −.163 | .047 | .027 |
| | | | | 70.3 | .694 | −.367 | .045 | |
| | | | | 69.5 | .714 | −.429 | | .022 |

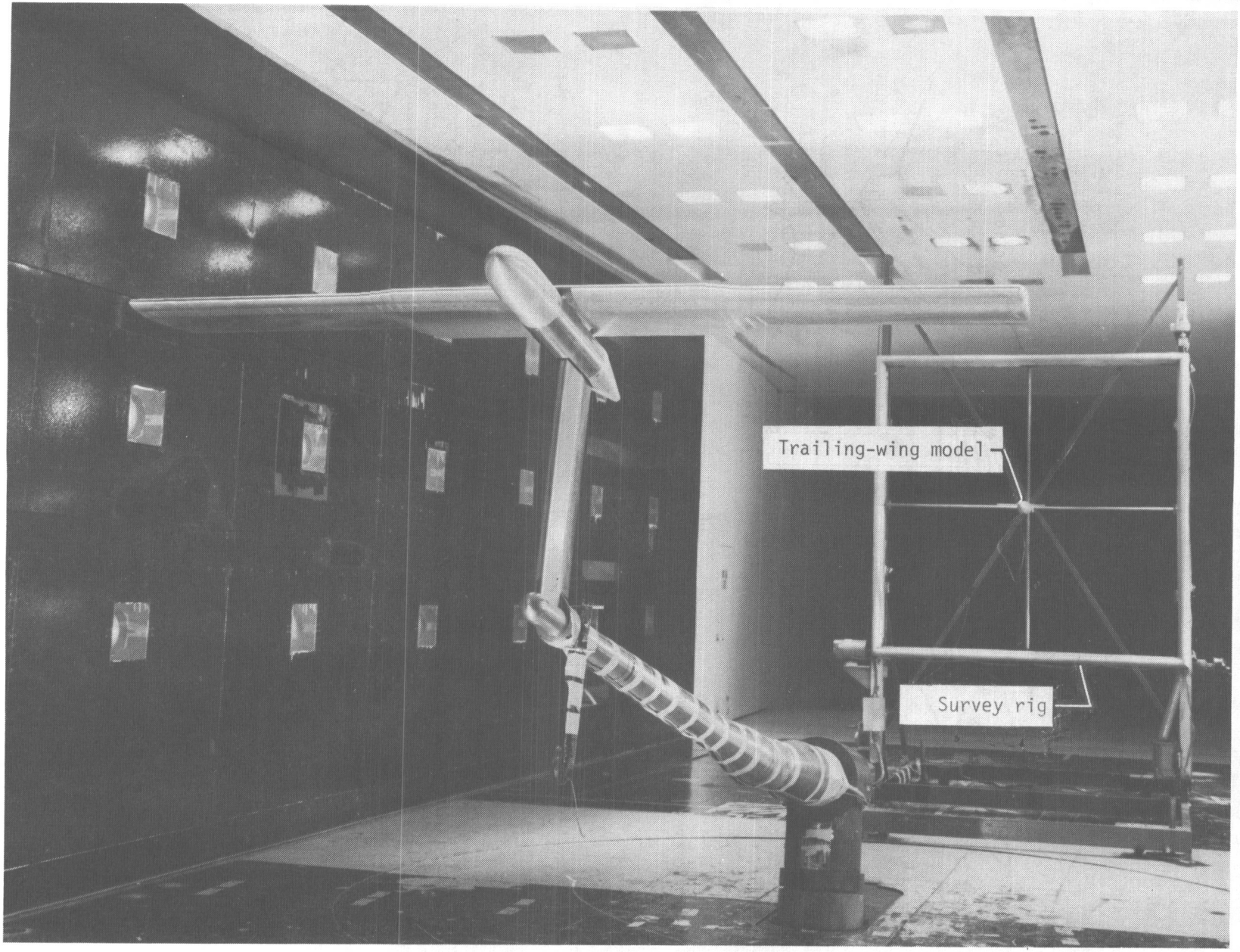


L-85-105

Figure 1. Variable twist wing (VTW) model blade mounted in test section of Langley 4- by 7-Meter Tunnel.

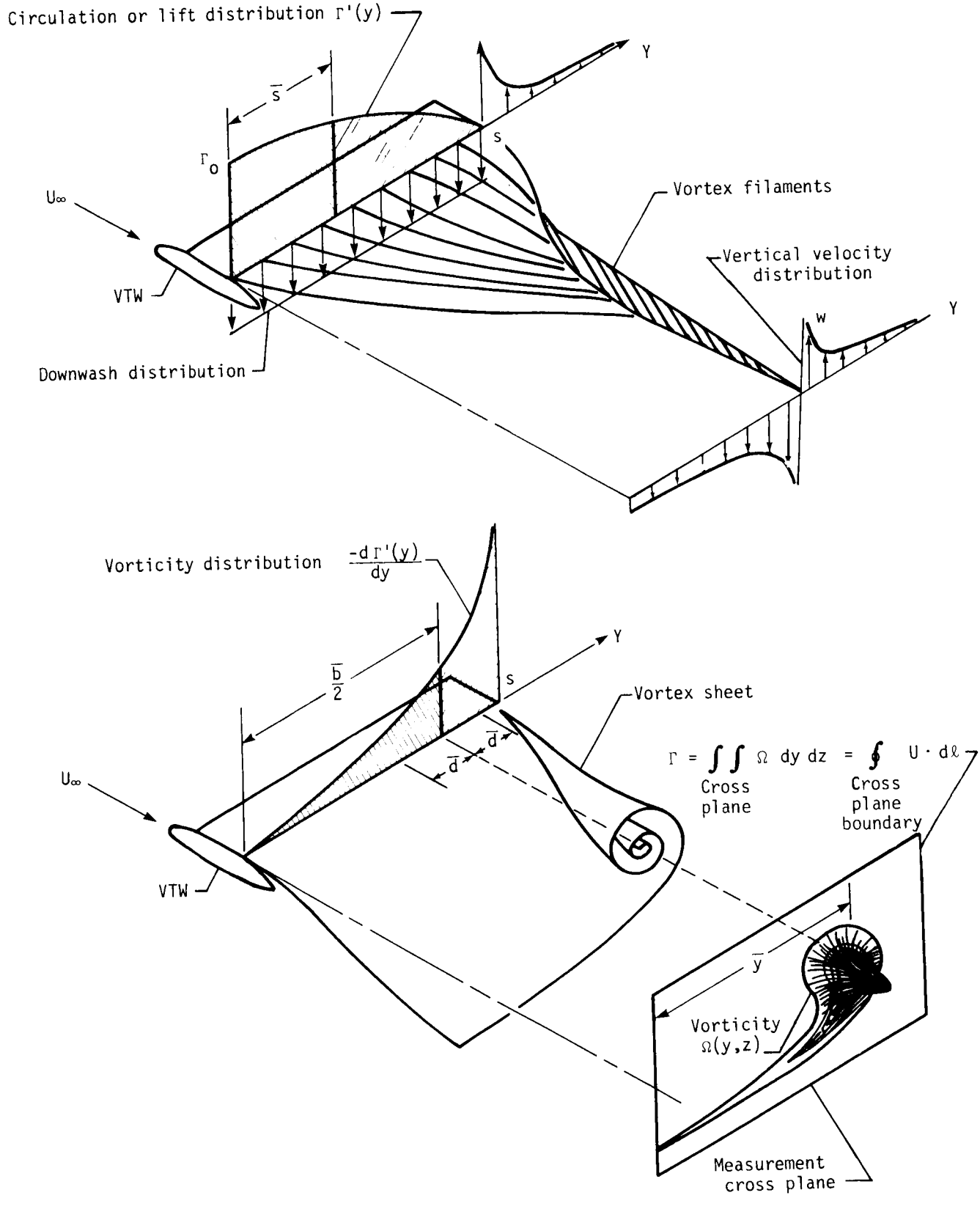


Figure 2. Vortex wake roll up as determined by wing span load distribution.

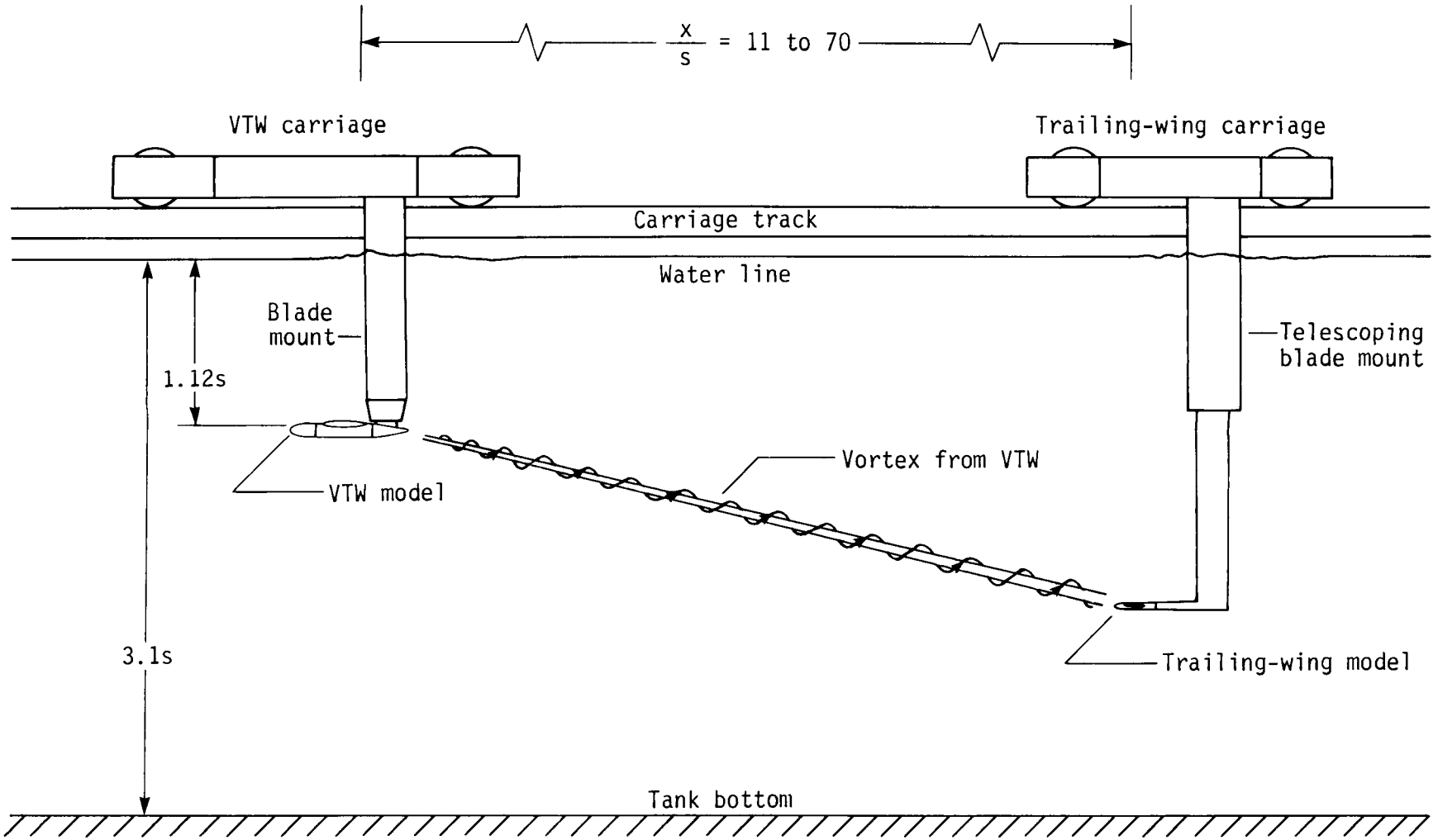


Figure 3. Hydronautics Ship Model Basin water towing tank facility with VTW and trailing-wing models in typical test conditions.

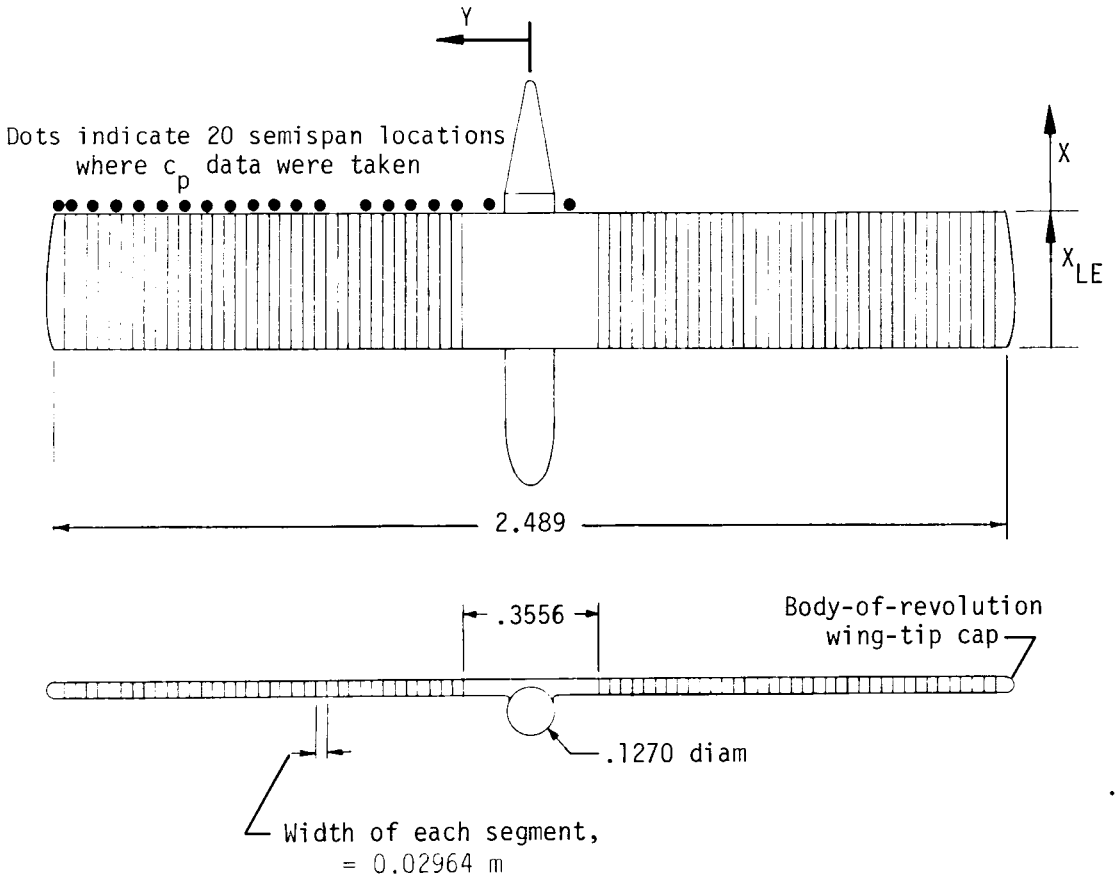


| Wing characteristics | |
|---|---|
| Area, S | 0.8852 $m^2$ |
| Semispan, s | 1.245 m |
| Chord, c | 0.3556 m |
| Aspect ratio | 7 |
| Taper ratio | 1 |
| Airfoil section | NACA 0012 |
| Segment width | 0.02964 m |

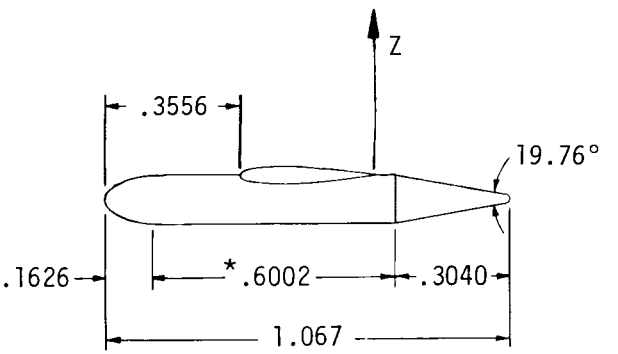


*Cylindrical body length

Figure 4. Three-view sketch of VTW model with no wing twist applied. All dimensions are in meters.

| Device | Front face position, $x_{LE}/c$ |
|---|---|
| Spoiler | 0.3 |
| Spline | 1.43 |
| Drag plate | 1.43 |

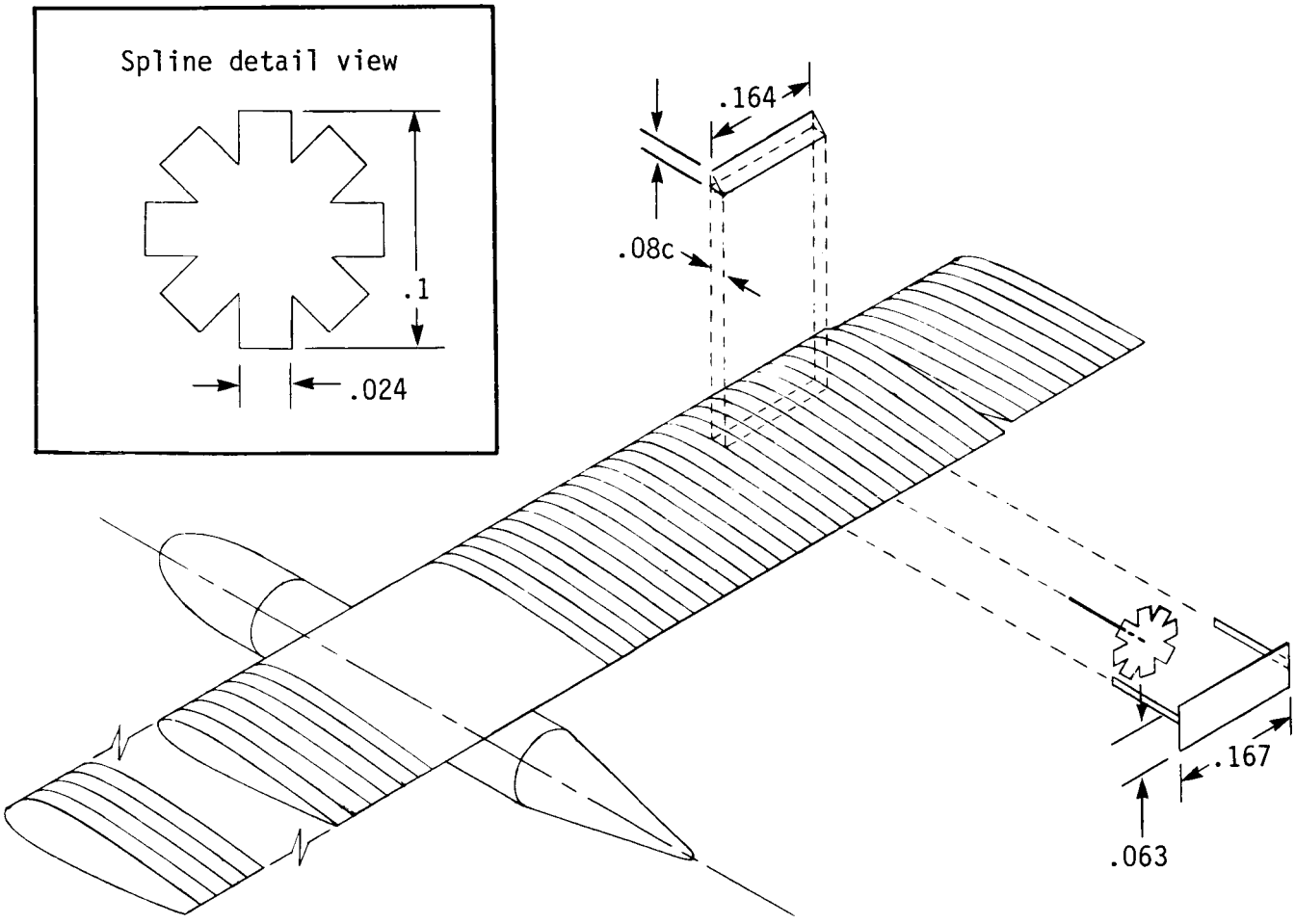


Figure 5. Installation of spoilers, splines, or drag plates at $y/s = \pm 0.607$ on VTW. Unless noted, all dimensions are normalized by VTW semispan.

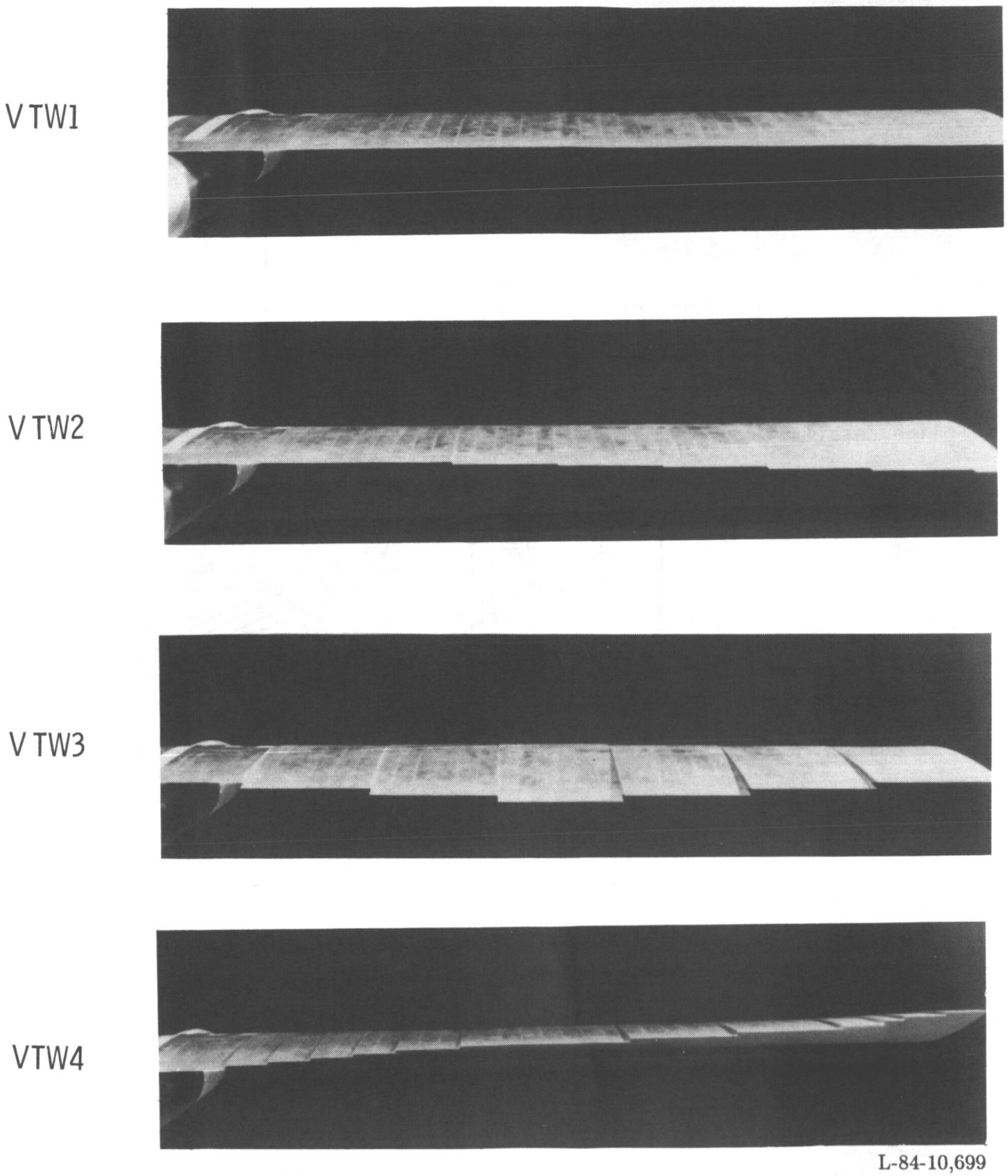


(a) Group I—continuous span load distributions.

Figure 6. VTW groups.

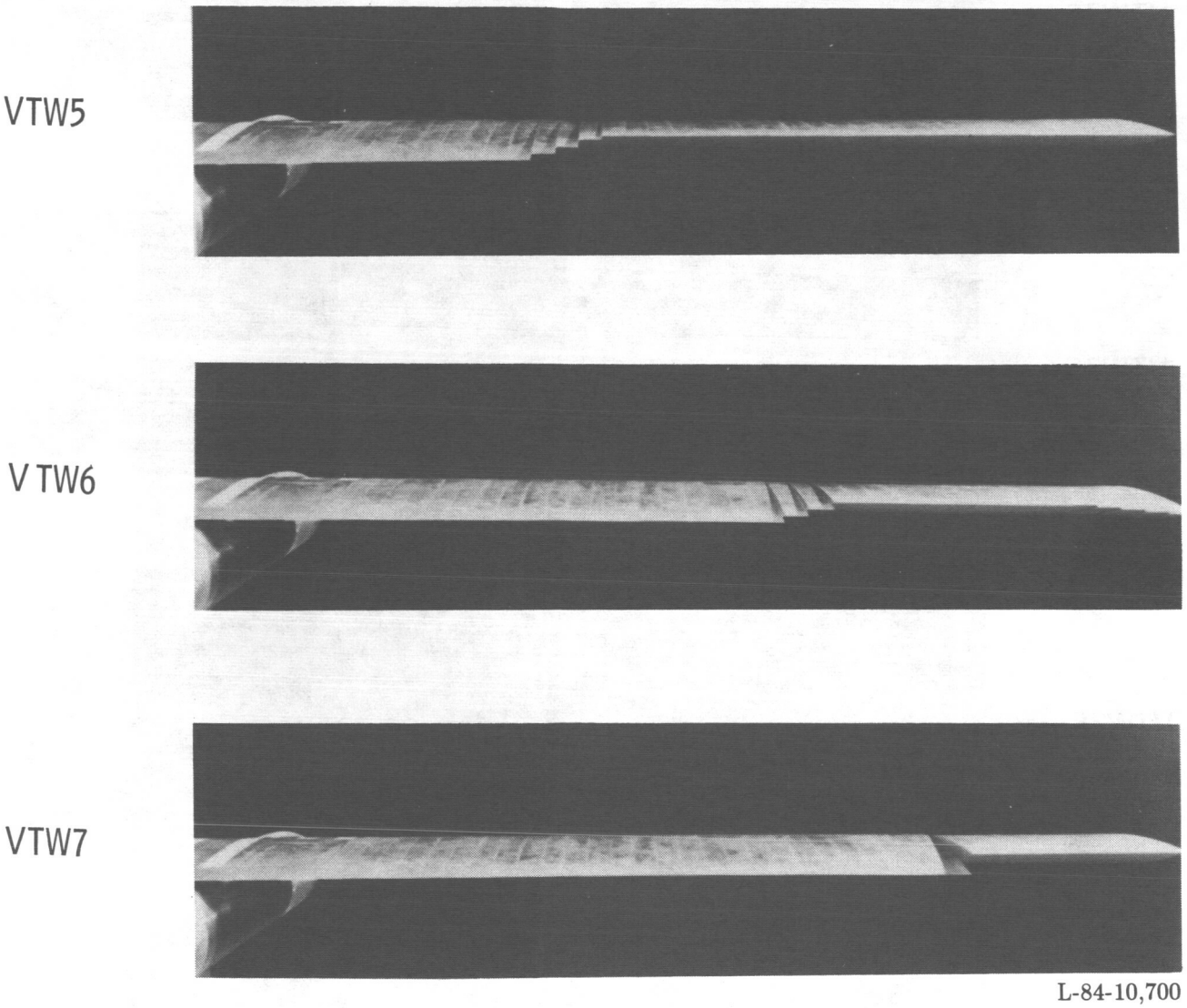


L-84-10,700

(b) Group II—partial-span-flap span load distributions.

Figure 6. Continued.

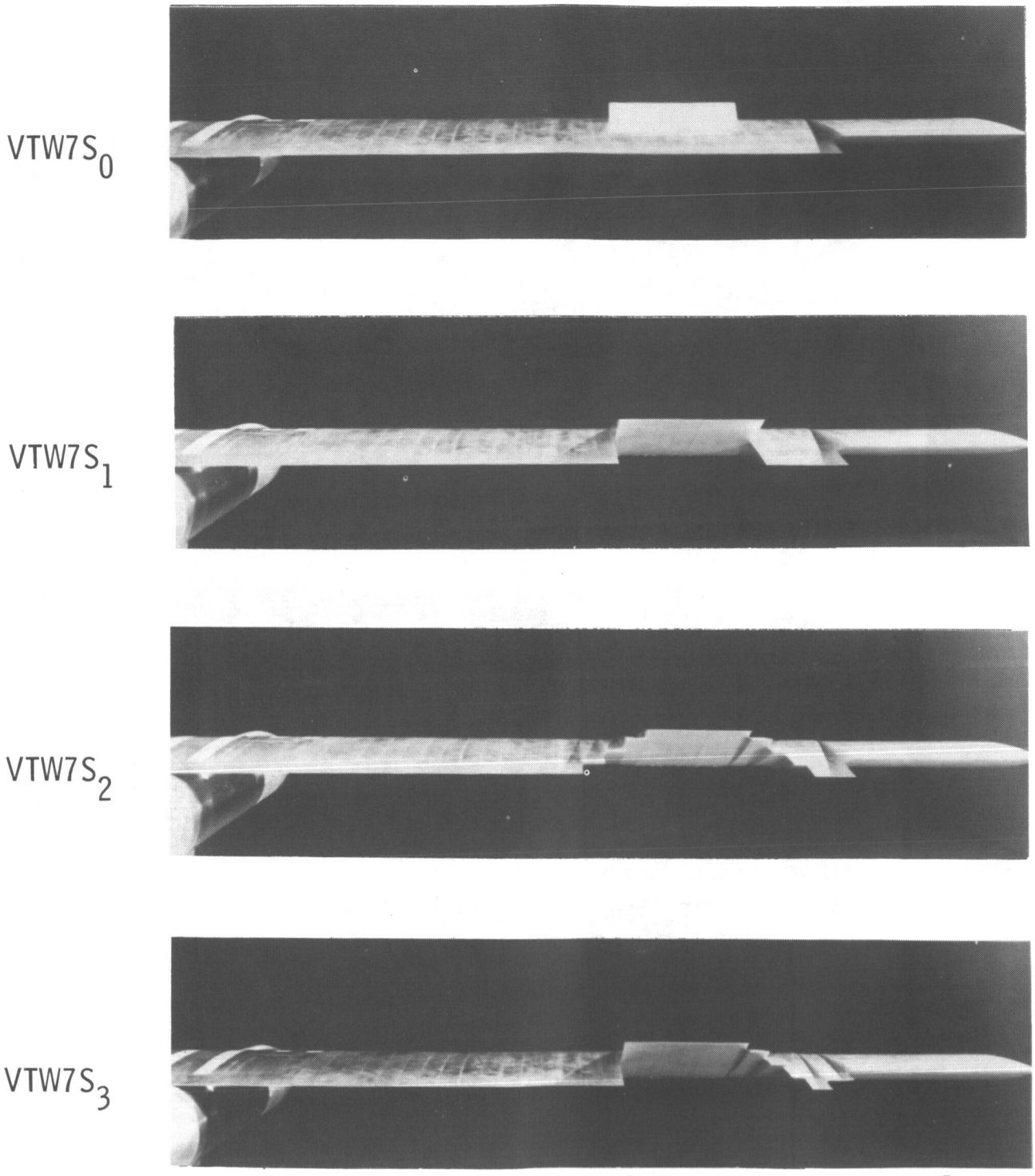


(c) Group III—alleviated vortex wake configurations.

Figure 6. Continued.

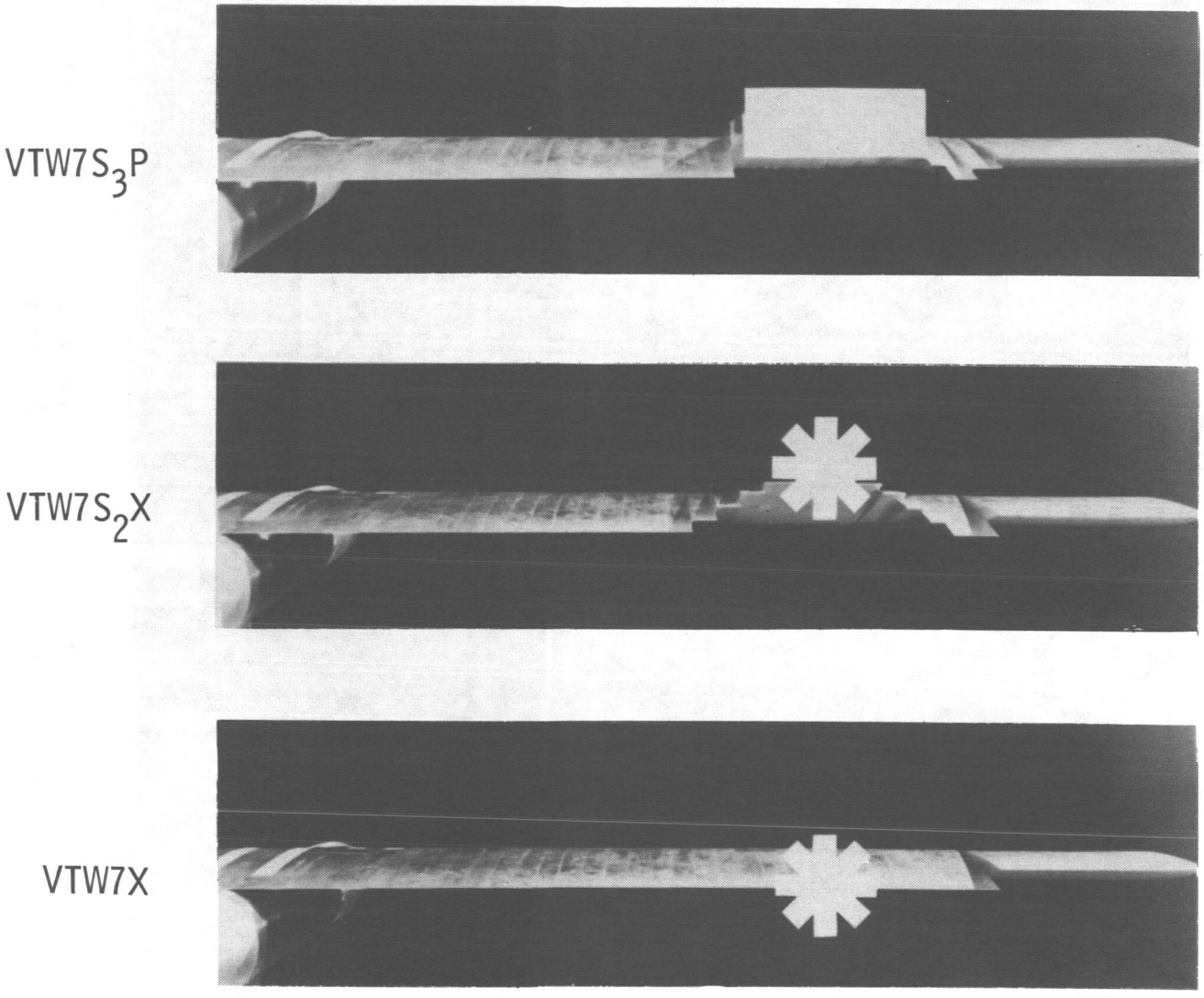


L-85-104

(c) Concluded.

Figure 6. Concluded.

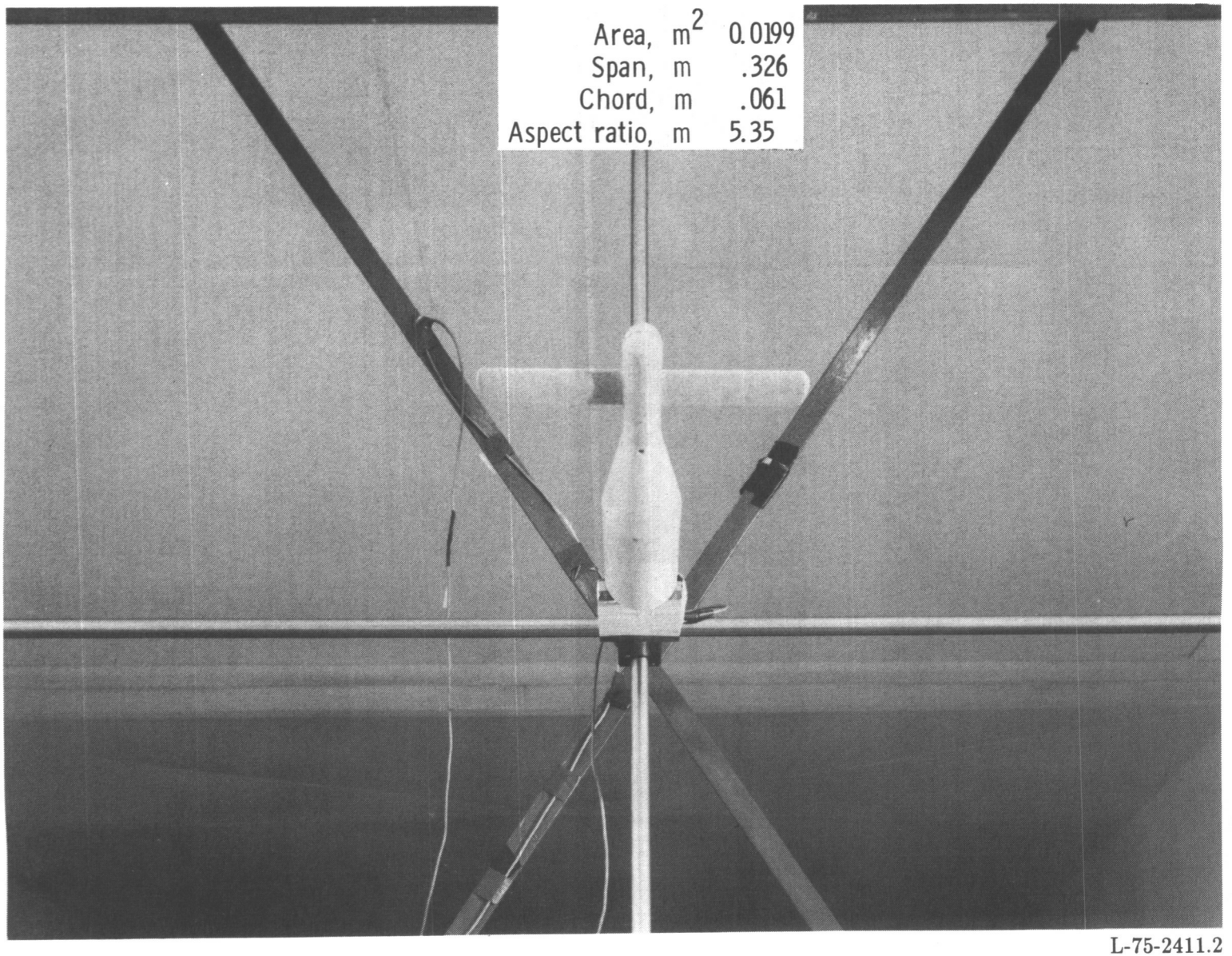


L-75-2411.2

Figure 7. Unswept trailing-wing model installed on wind tunnel traverse mechanism (looking up at model from point slightly in front of traverse frame). Model has NACA 0012 airfoil section.

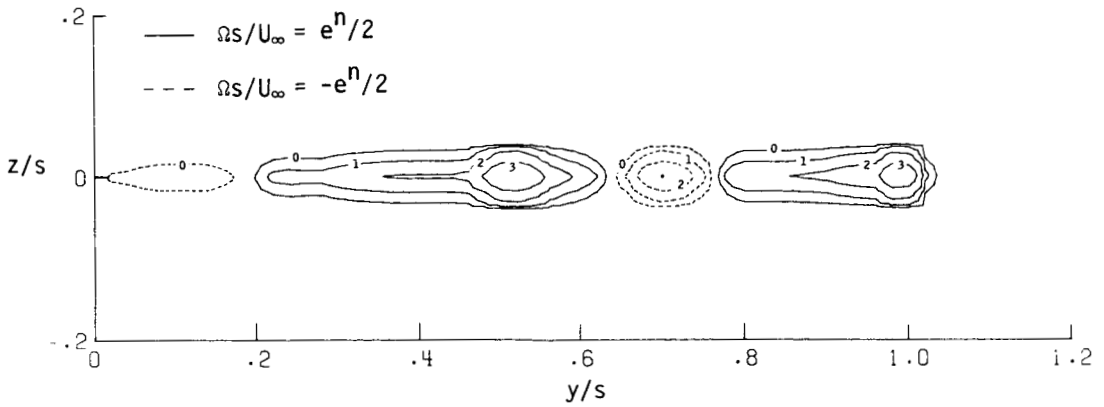


(a) Initialization at $x/s = 0$ from span load measurements.

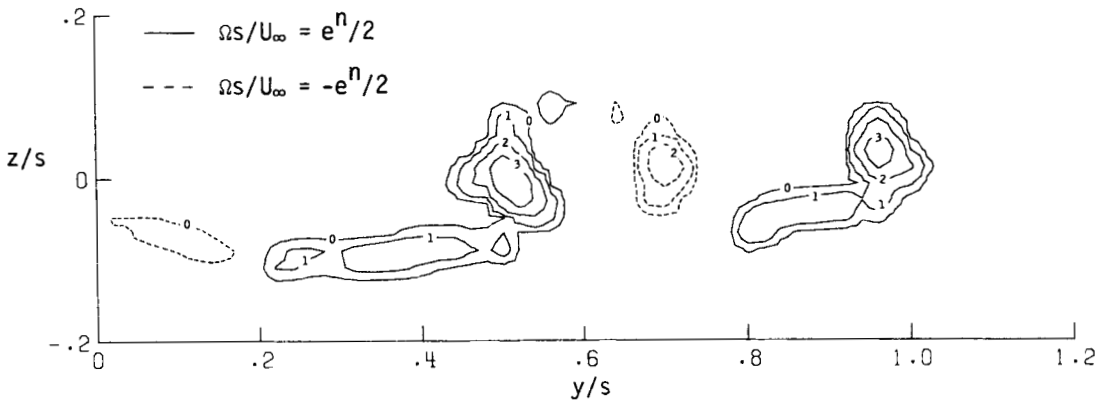


(b) Predicted vorticity at $x/s = 1$.

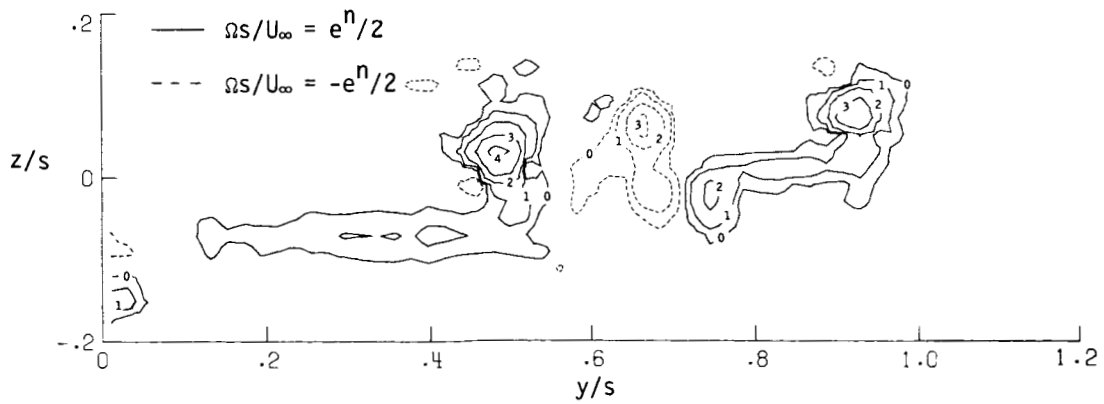


(c) Measured vorticity at $x/s = 1$.

Figure 8. Predicted vorticity cross plane at $x/s = 1$ based on measured span load for VTW7S$_3$. Measured vorticity cross plane at $x/s = 1$ provided for comparison. Contours are labeled with the exponent $n$.

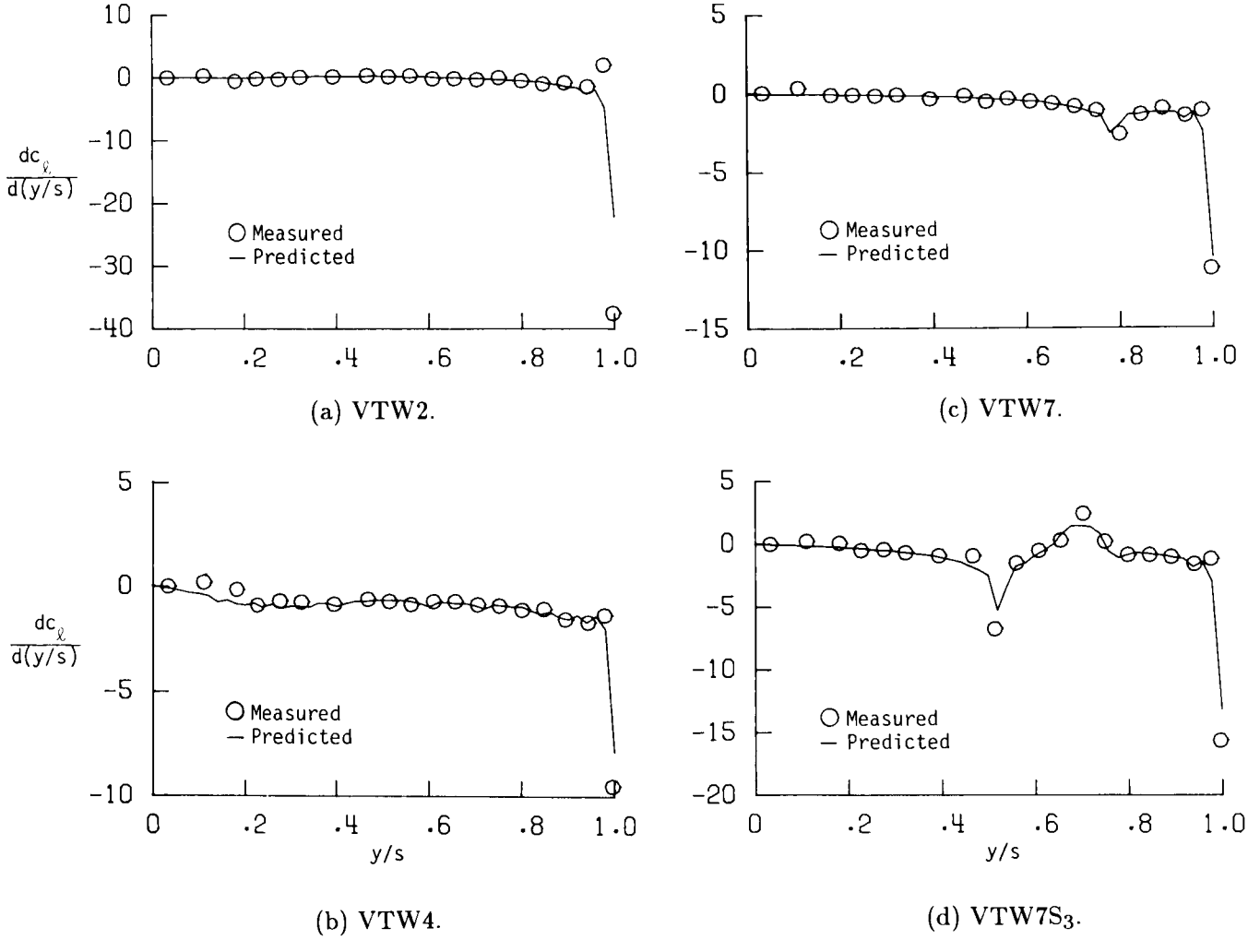


(a) VTW2.

(c) VTW7.

(b) VTW4.

(d) VTW7S$_3$.

Figure 9. Vortex-lattice-predicted and span load measured $dc_\ell/d(y/s)$.

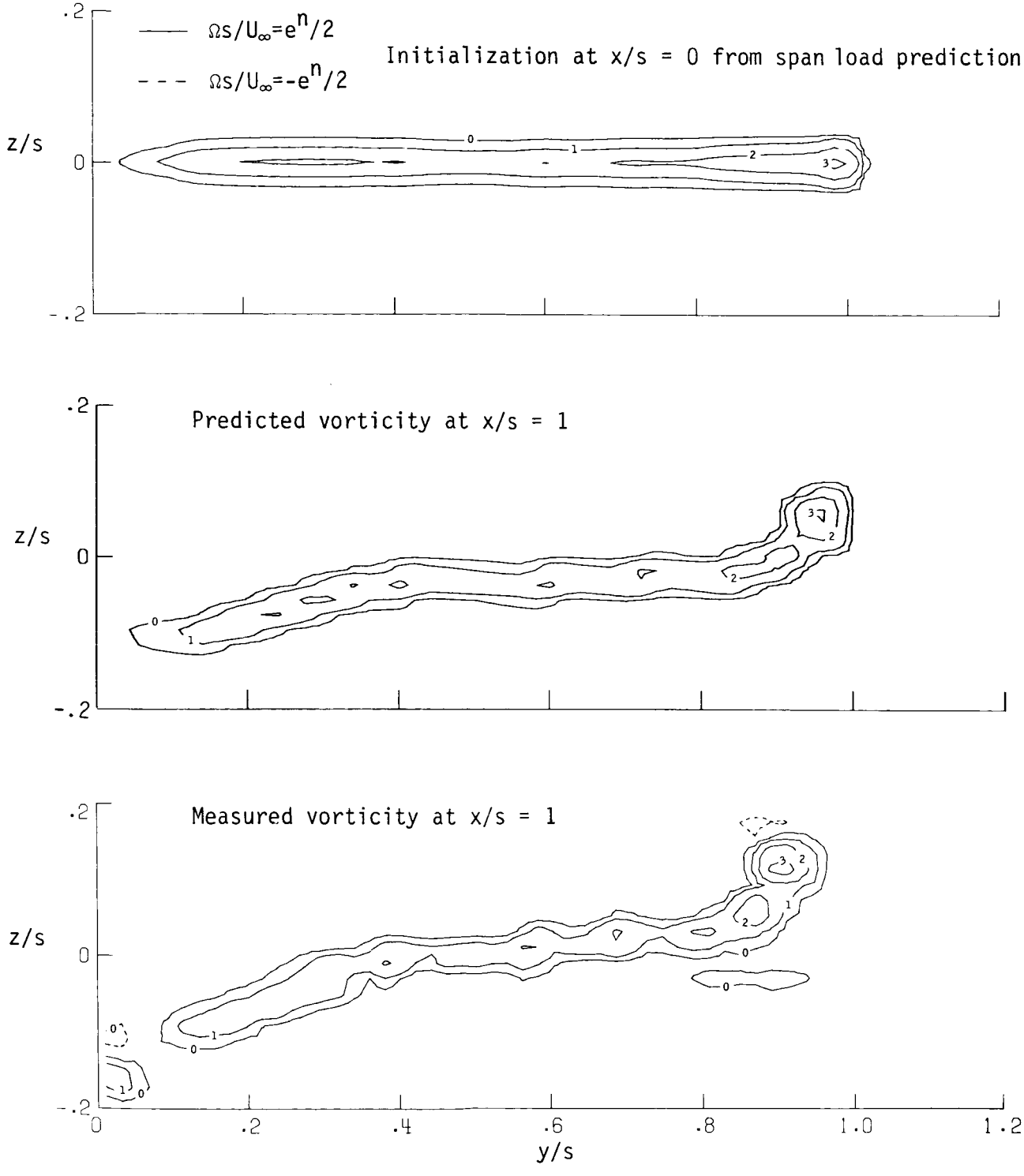


(a) VTW4.

Figure 10. Predicted vorticity cross plane at $x/s = 1$ based on predicted span load. Measured vorticity cross plane at $x/s = 1$ provided for comparison. Contours are labeled with the exponent $n$.

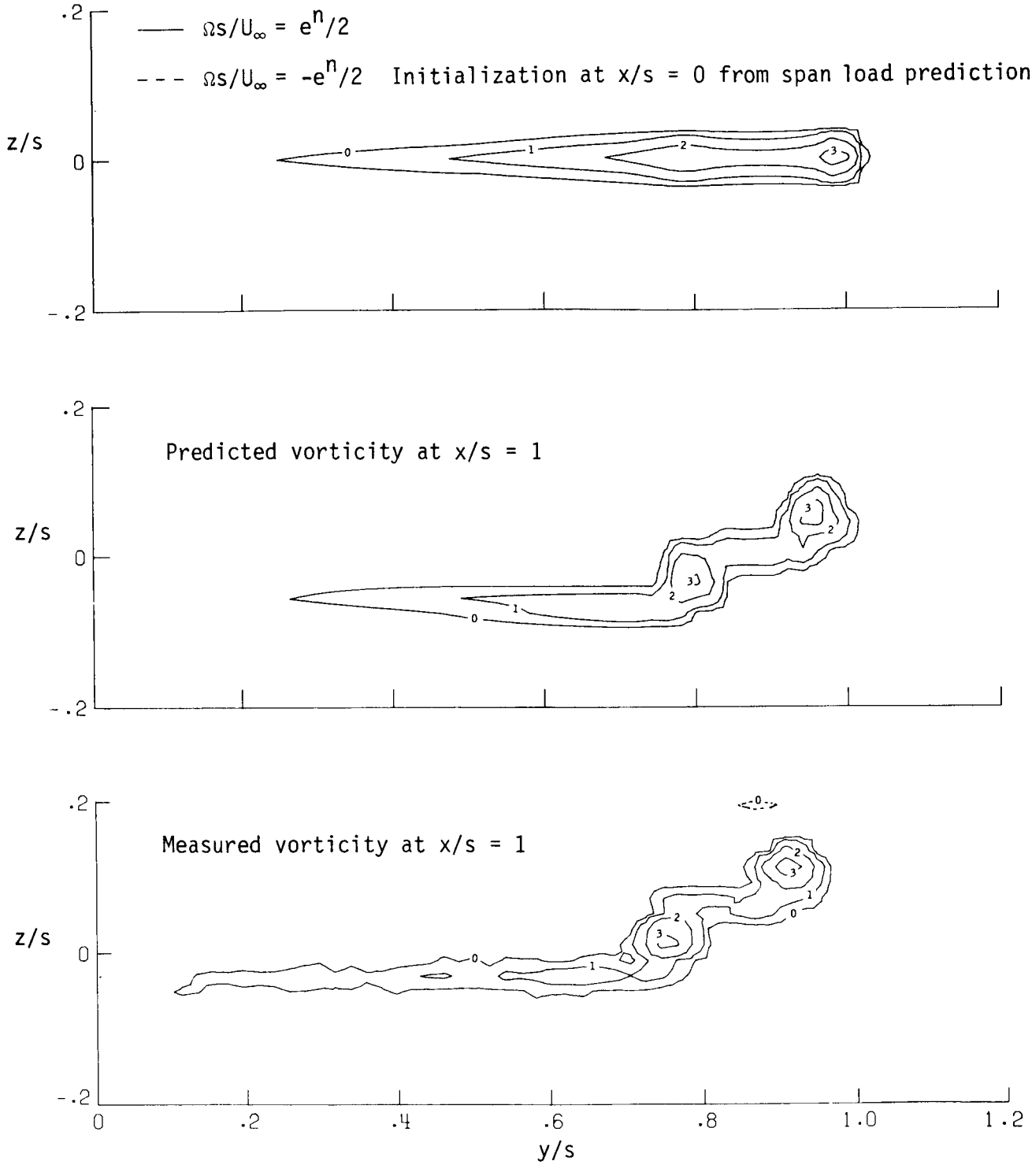


(b) VTW7.

Figure 10. Continued.

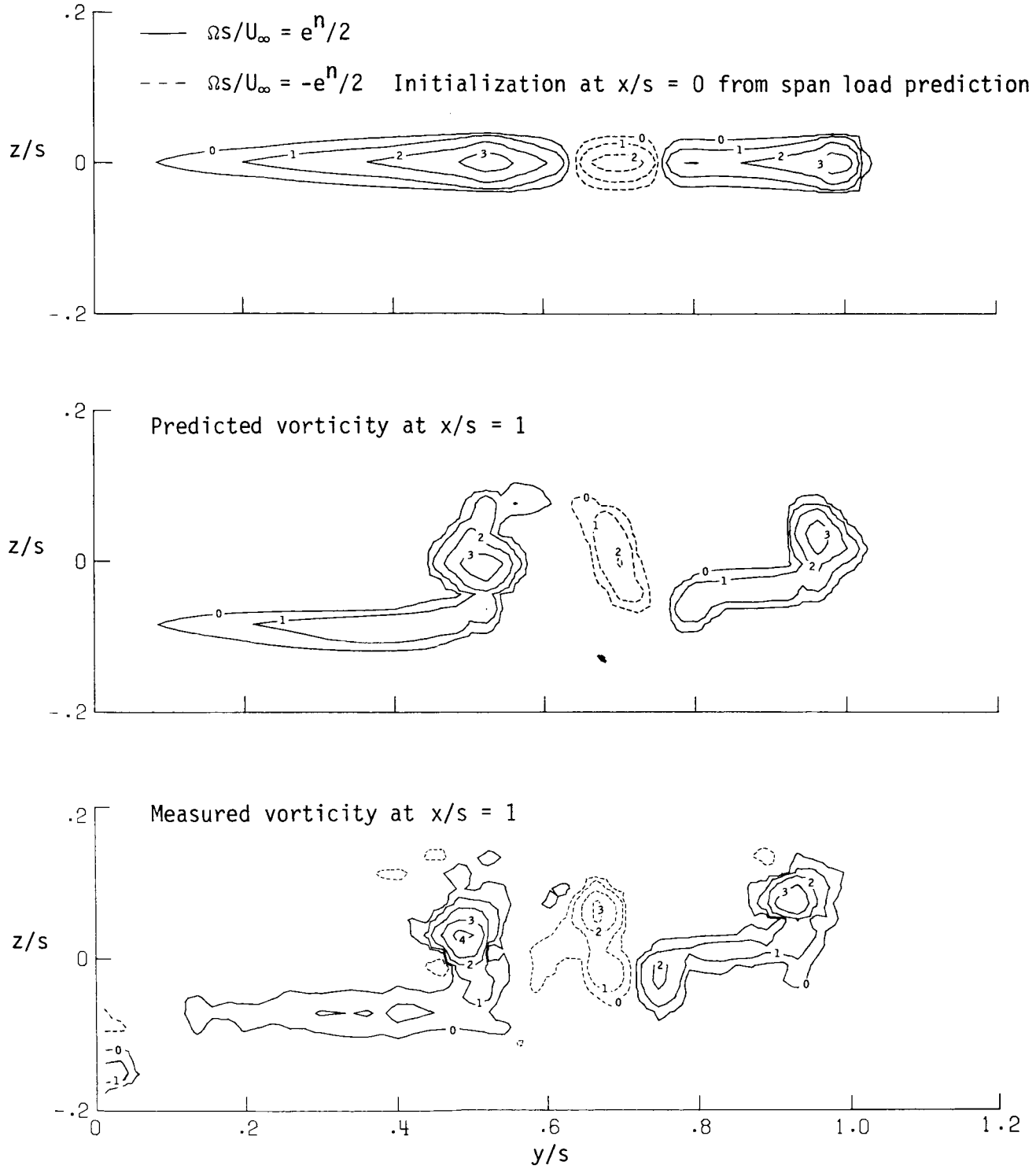


(c) VTW7S$_3$.

Figure 10. Concluded.

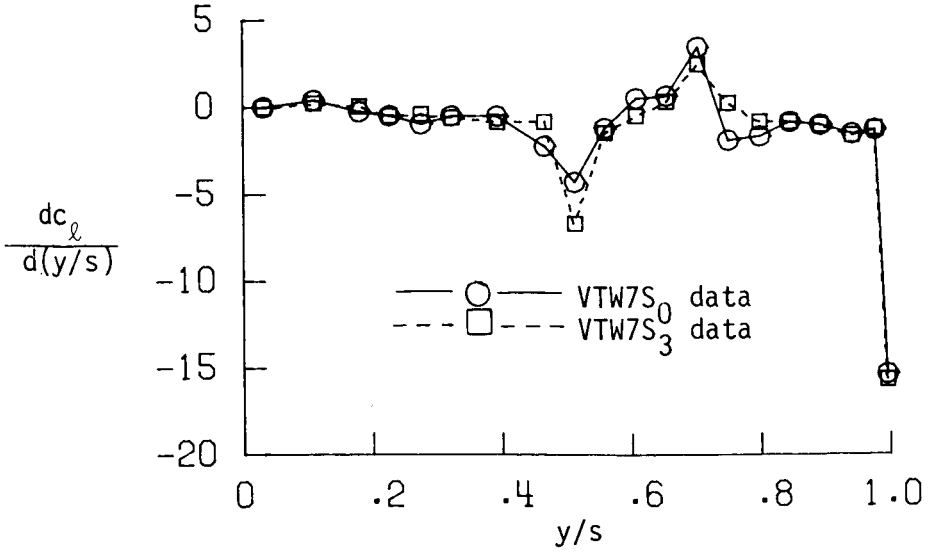


(a) Measured $dc_\ell/d(y/s)$ for wind tunnel VTW configurations.

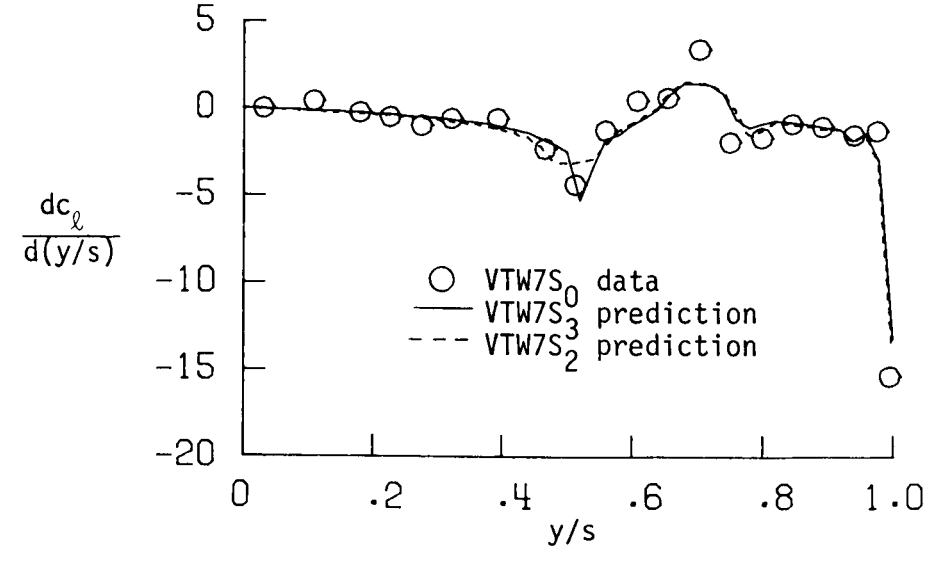


(b) Measured $dc_\ell/d(y/s)$ for VTW7S$_0$ and predicted $dc_\ell/d(y/s)$ for wind tunnel configuration VTW7S$_3$ and water tank configuration VTW7S$_2$.

Figure 11. Values of $dc_\ell/d(y/s)$ for wind tunnel and water tank VTW configurations twisted to match the span load of VTW7S$_0$.

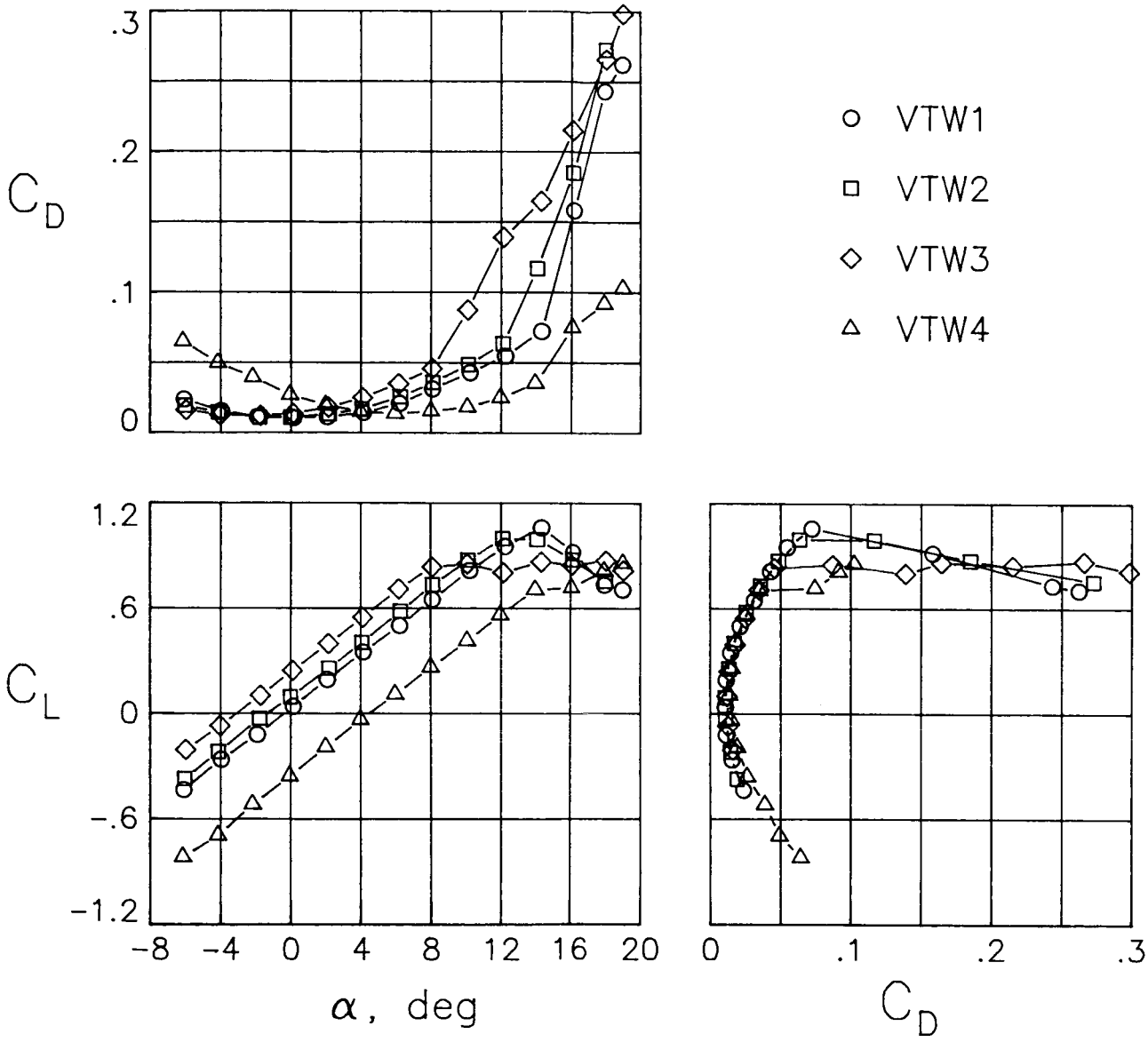


Figure 12. Aerodynamic data for VTW configurations in group I—continuous span load distributions.

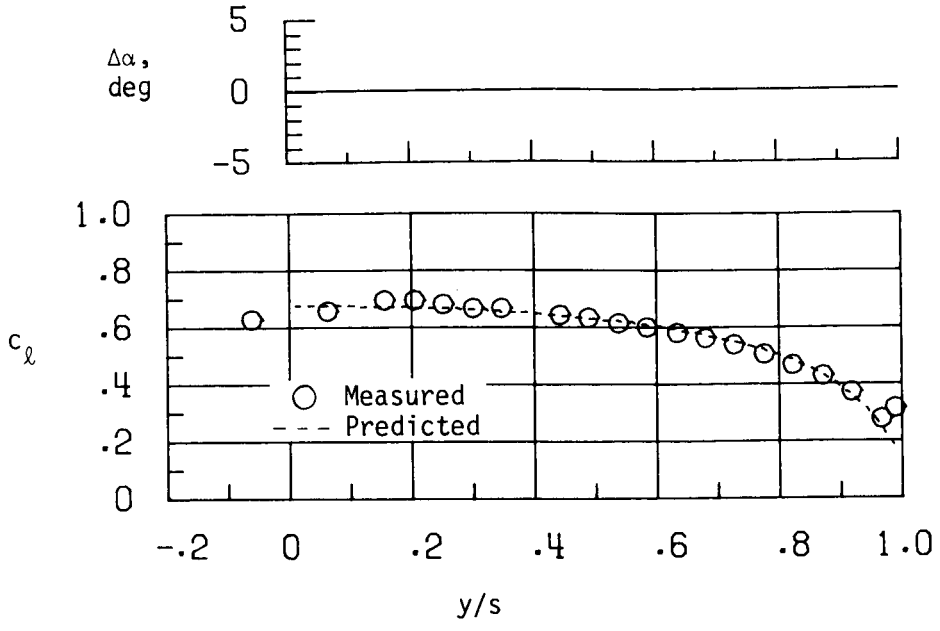


(a) VTW1.

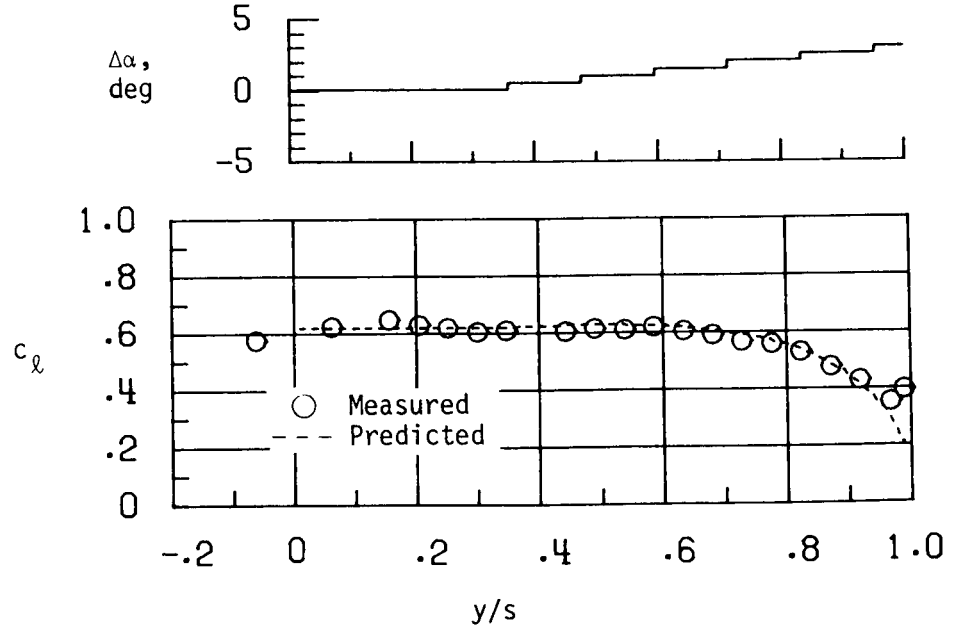


(b) VTW2.

Figure 13. Measured and vortex-lattice-predicted span loads for VTW configurations in group I—continuous span load distributions.

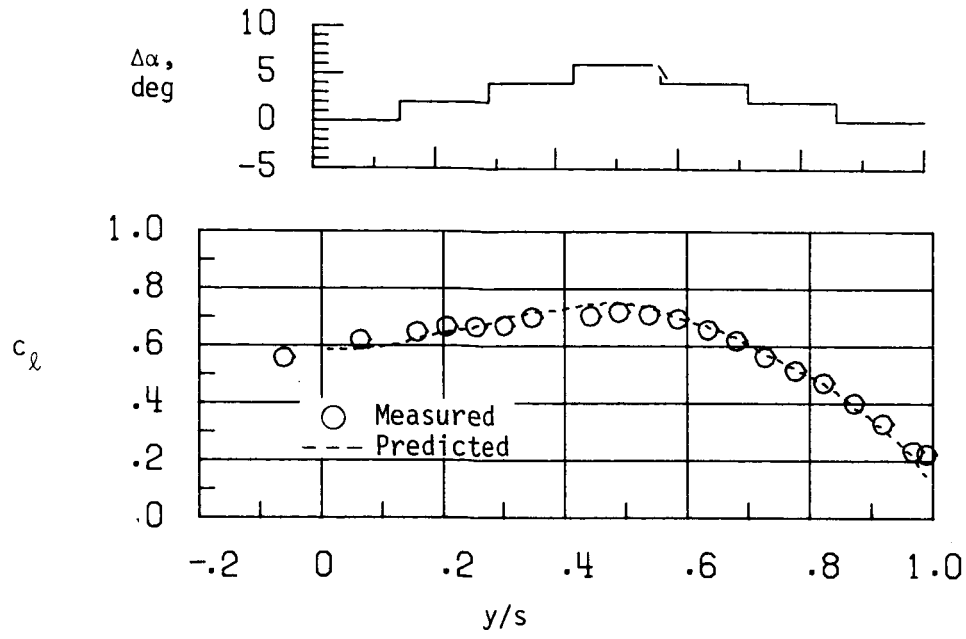


(c) VTW3.

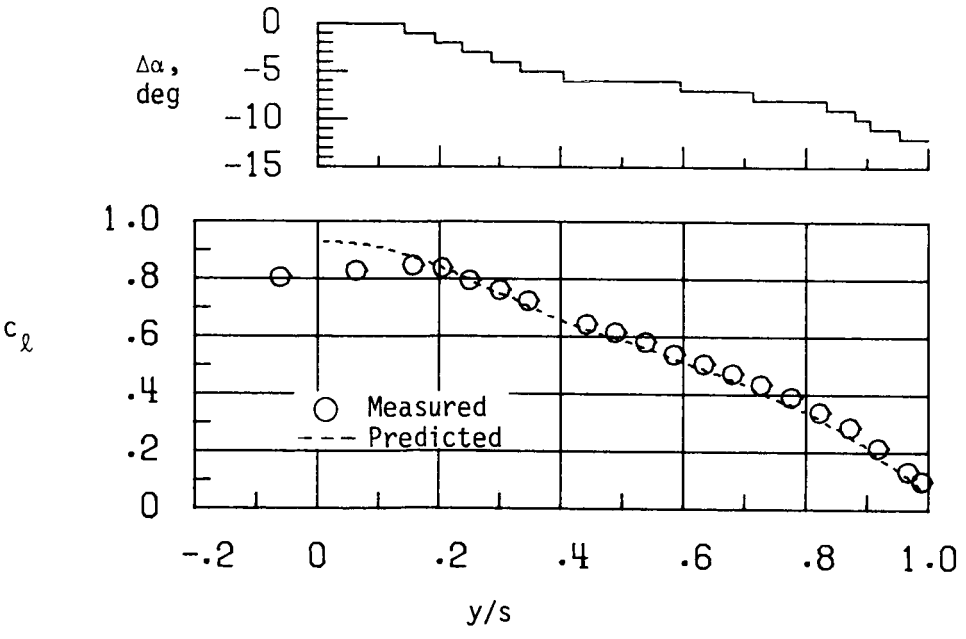


(d) VTW4.

Figure 13. Concluded.

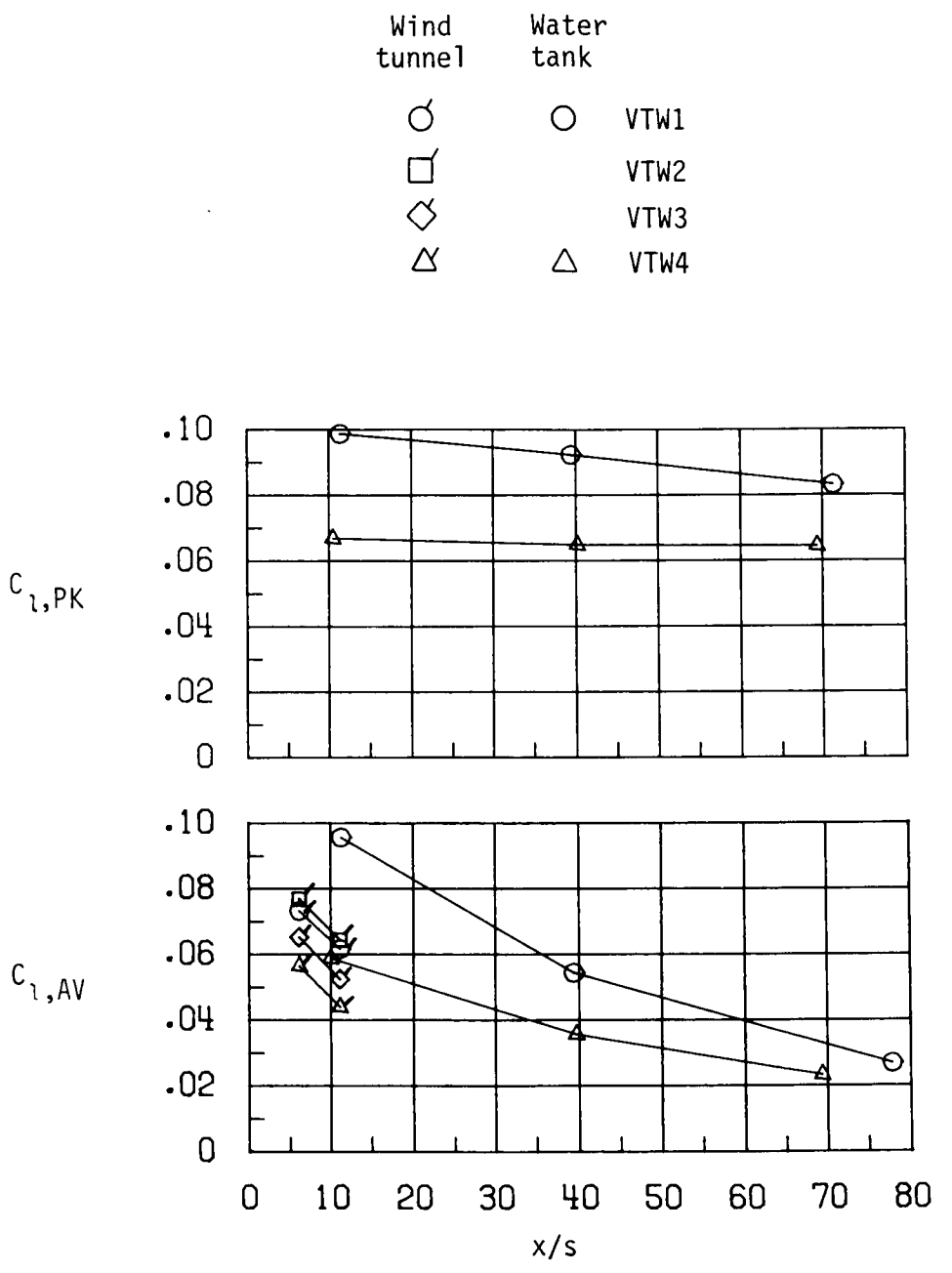


Figure 14. Trailing-wing rolling-moment data for VTW configurations in group I—continuous span load distributions.

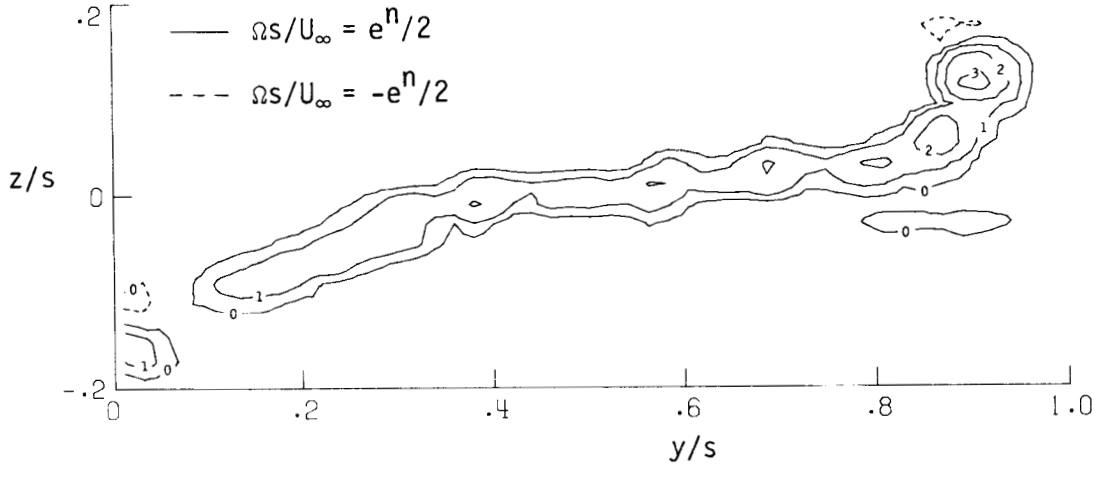


(a) $x/s = 1$.

Figure 15. Normalized vorticity contours in semispan wake of VTW4. Contours are labeled with the exponent $n$.

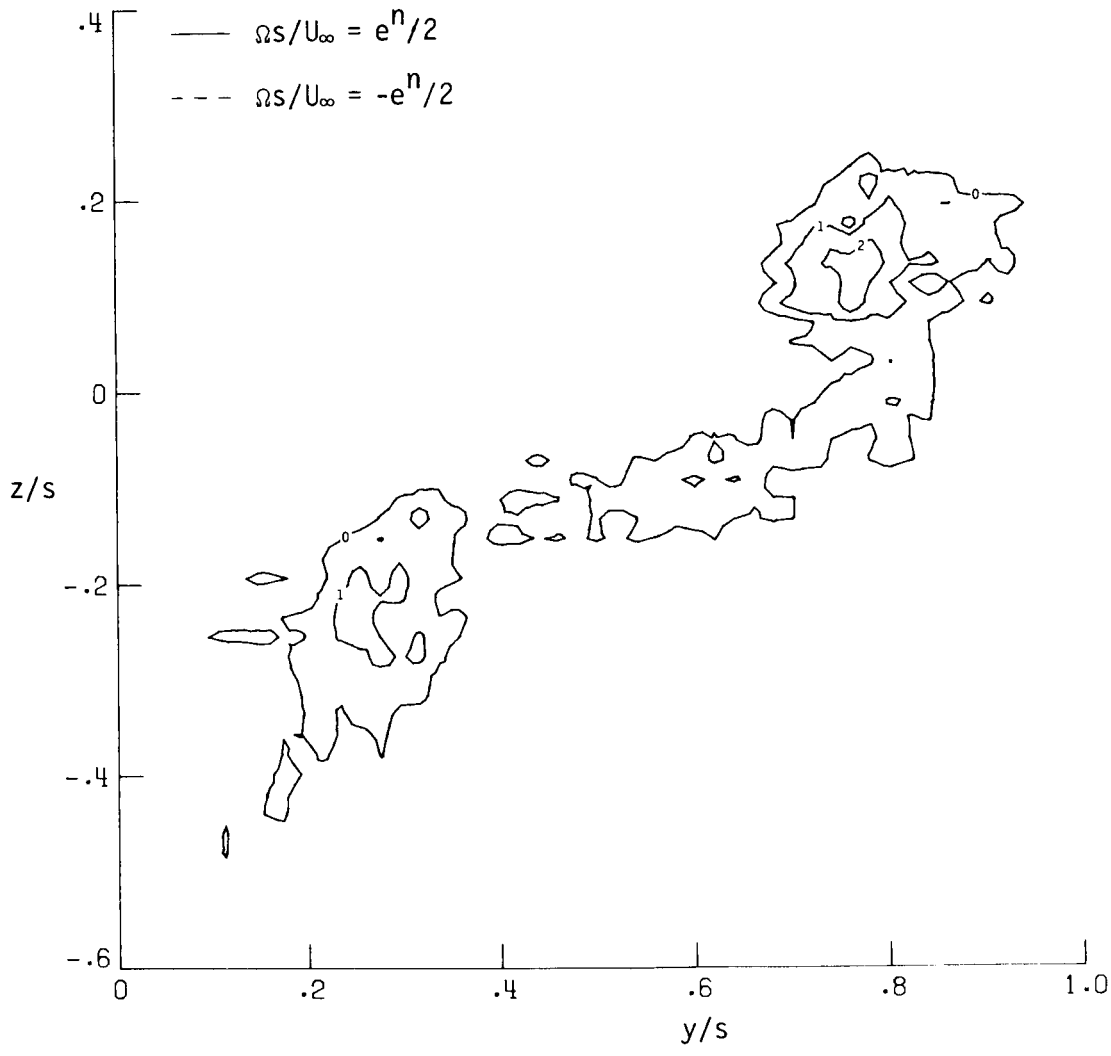


(b) $x/s = 6$.

Figure 15. Continued.

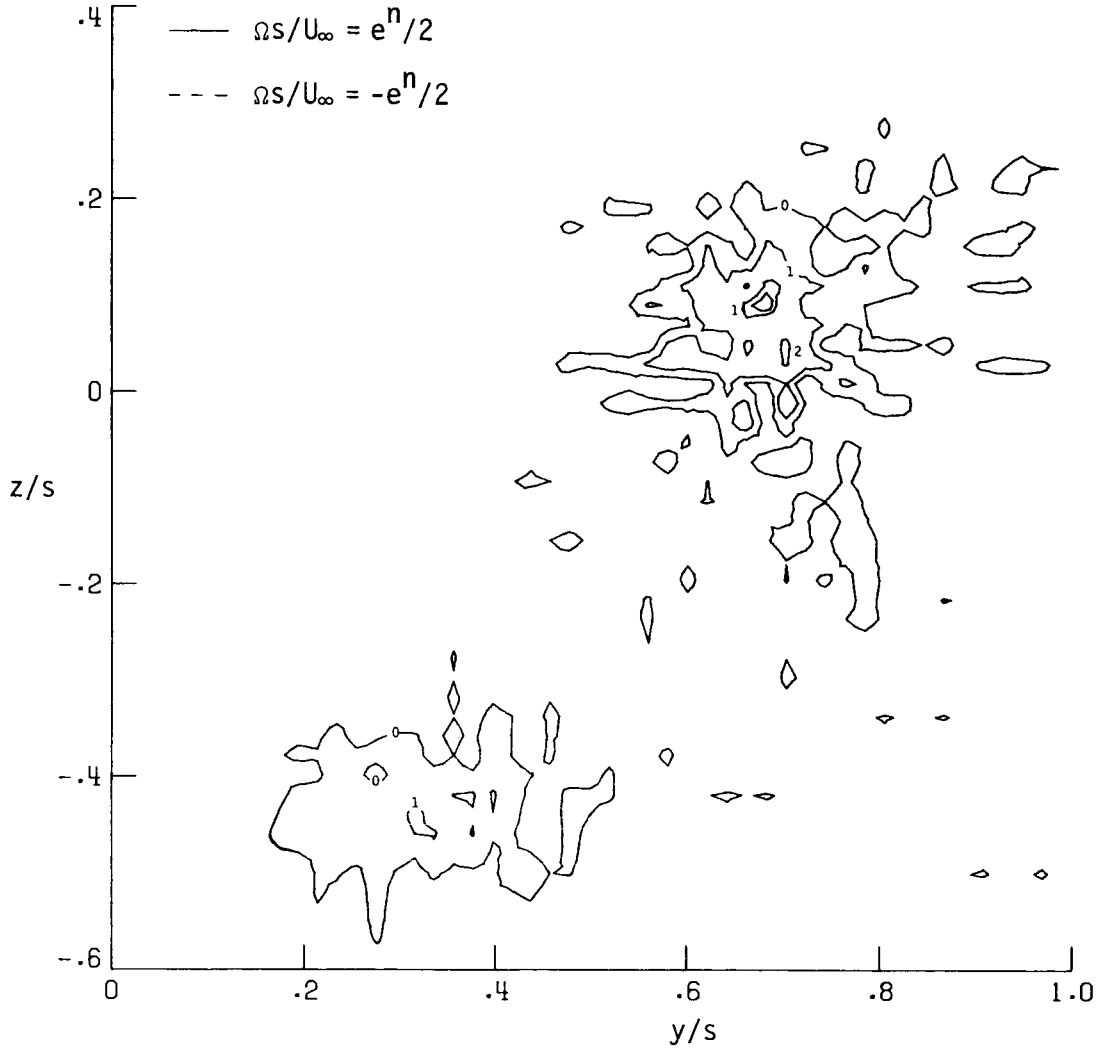


(c) $x/s = 11$.

Figure 15. Concluded.

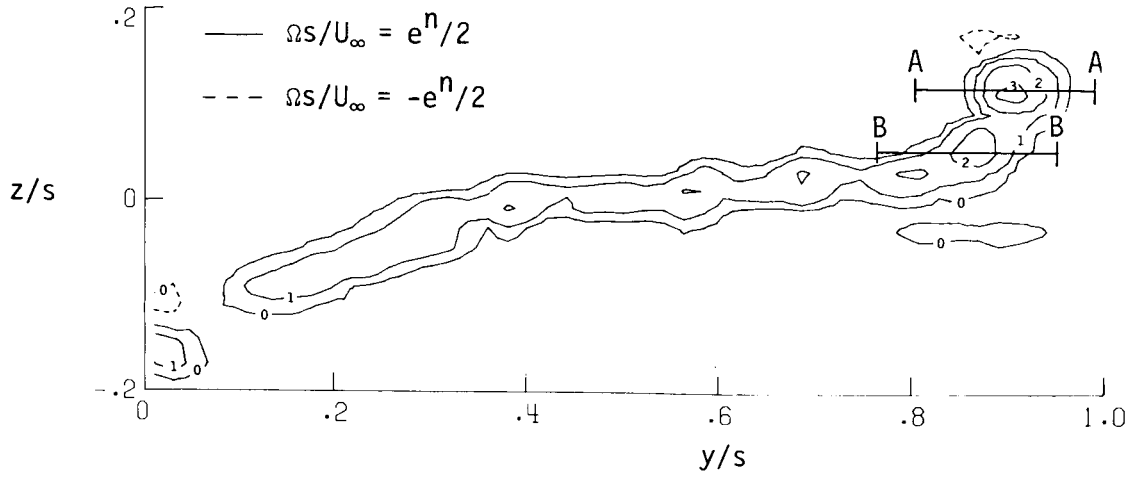


(a) Normalized vorticity field showing spatial position of velocity profiles. Contours are labeled with the exponent $n$.

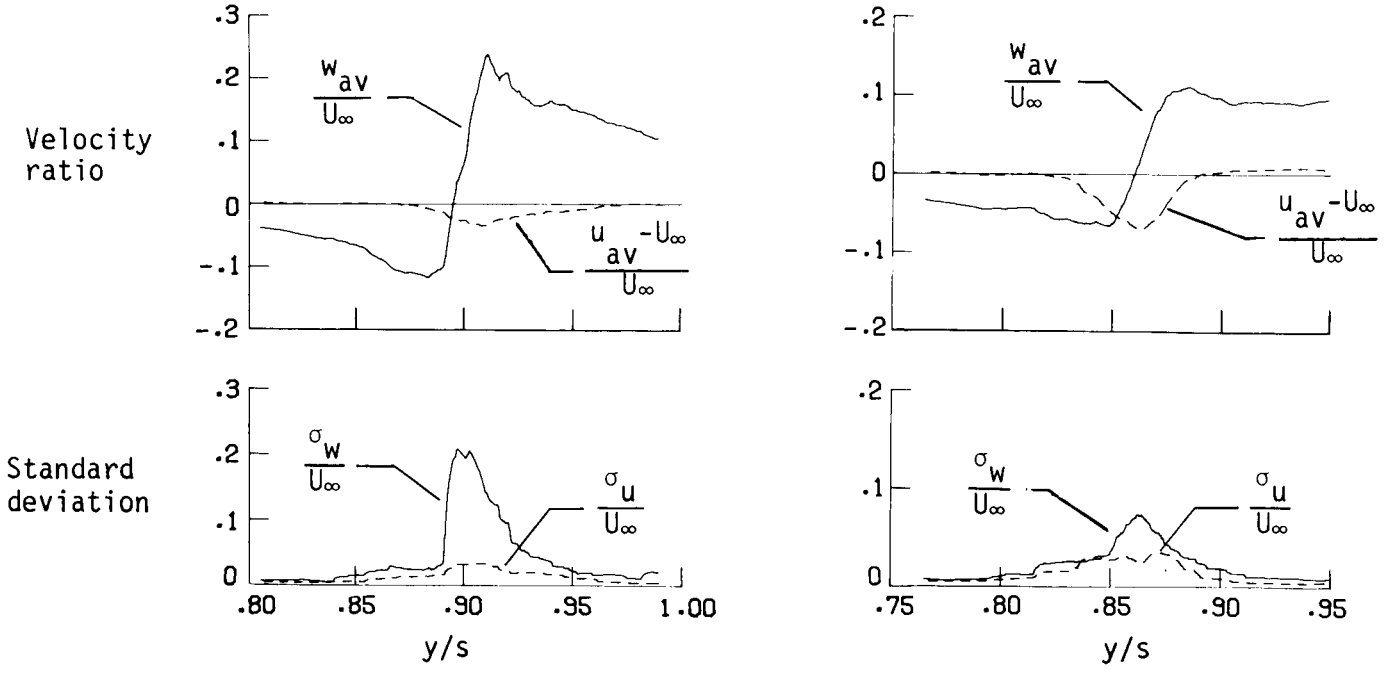


(b) Velocities along path A-A.

(c) Velocities along path B-B.

Figure 16. Normalized vorticity contours and vertical and axial velocity profiles for VTW4 at $x/s = 1$.

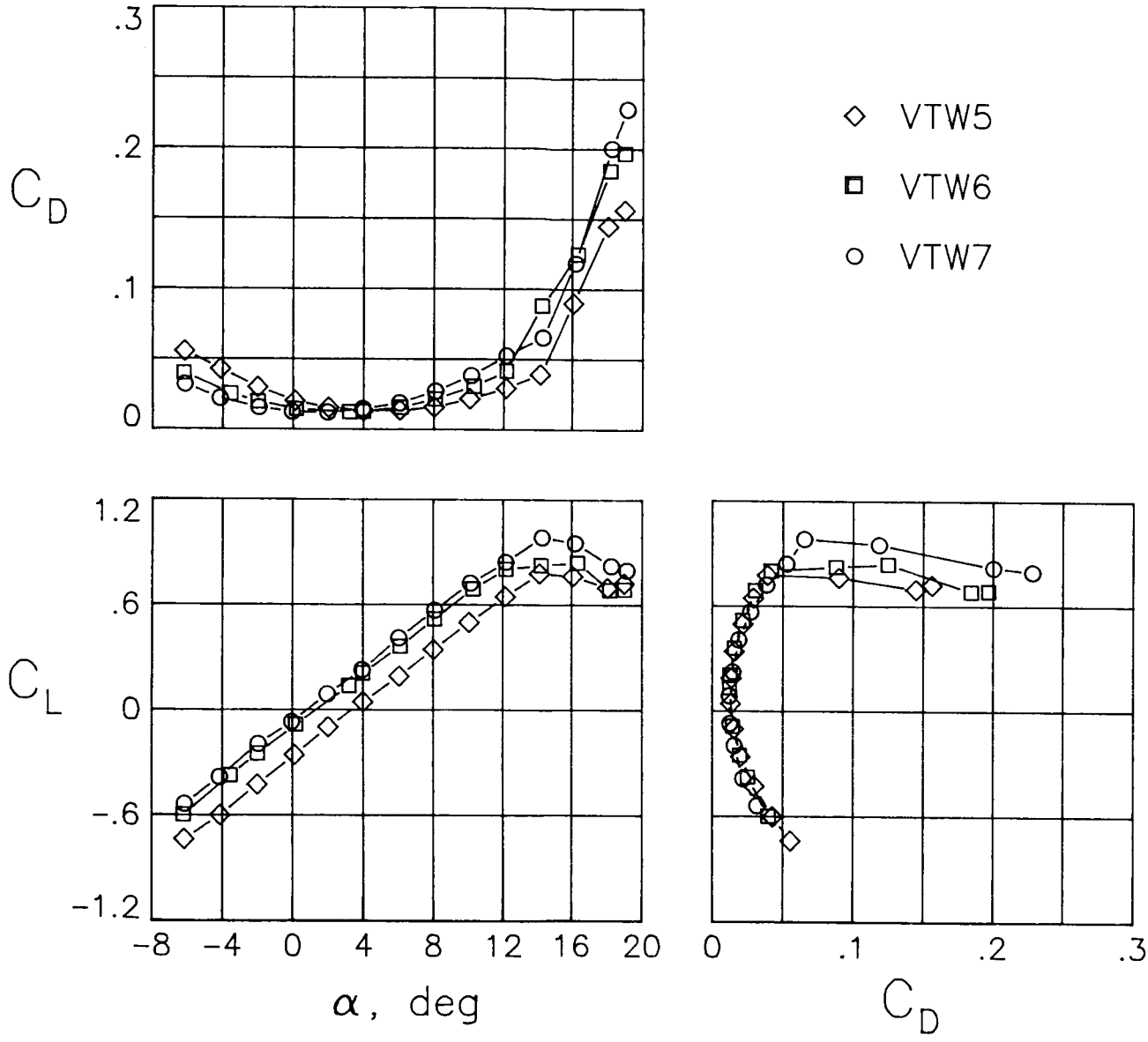


Figure 17. Aerodynamic data for VTW configurations in group II—partial-span-flap span load distributions.

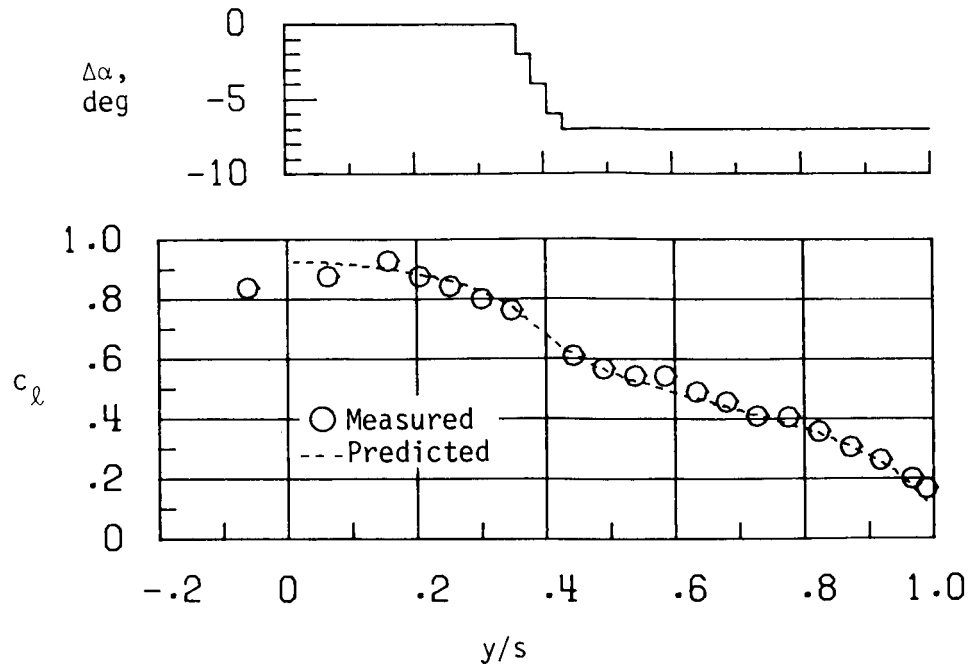


(a) VTW5.

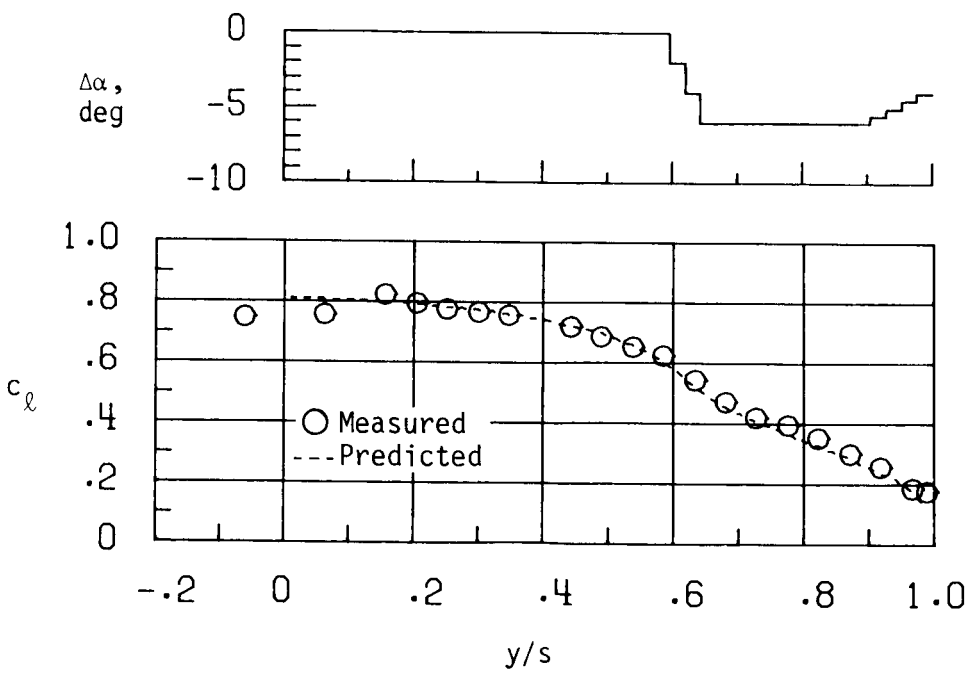


(b) VTW6.

Figure 18. Measured and vortex-lattice-predicted span loads for VTW configurations in group II—partial-span-flap span load distributions.

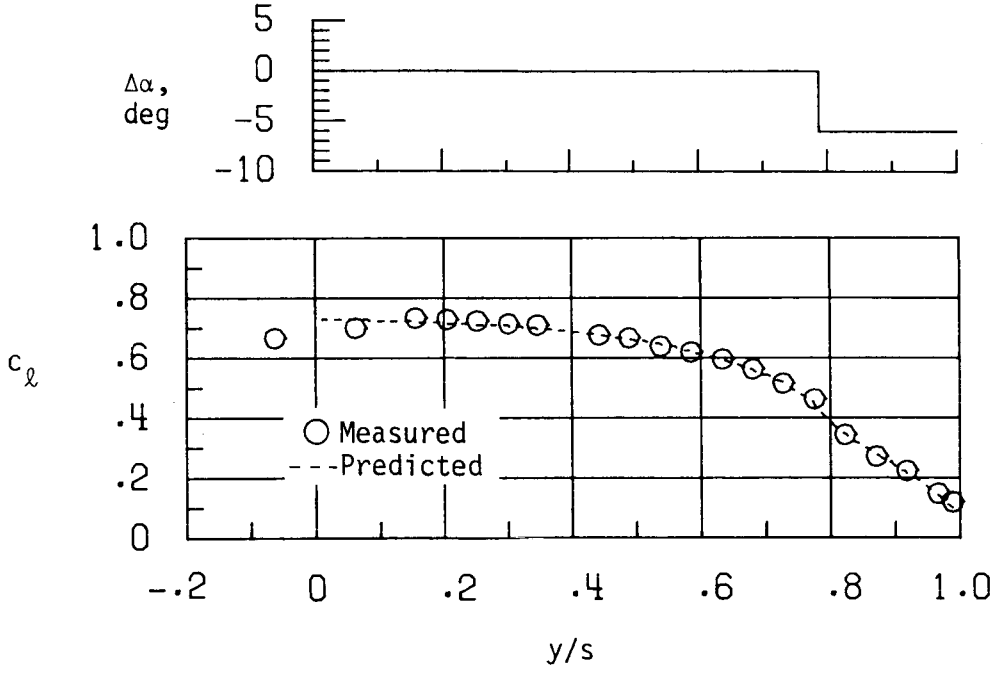


(c) VTW7.

Figure 18. Concluded.

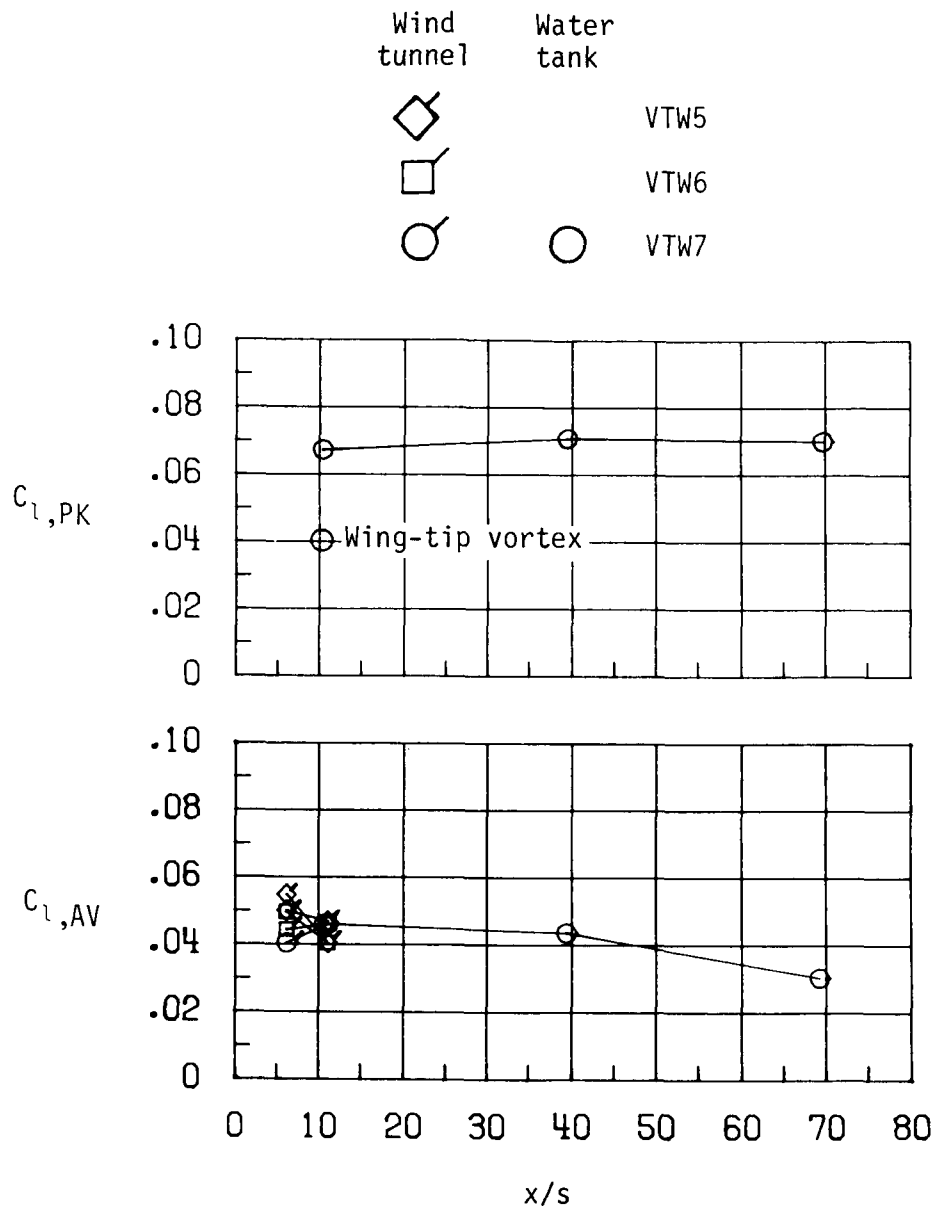


Figure 19. Trailing-wing rolling-moment data for VTW configurations in group II—partial-span-flap span load distributions.

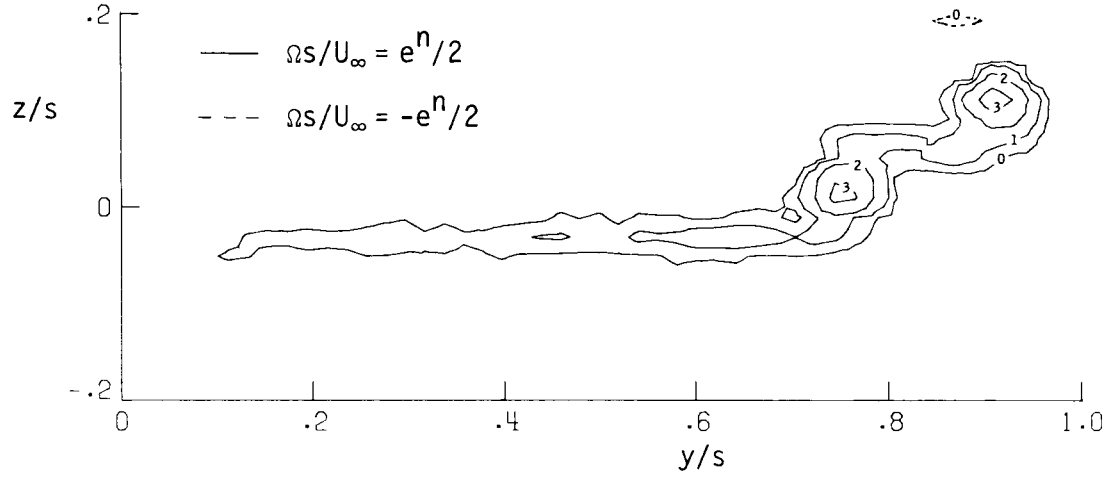


(a) $x/s = 1$.

Figure 20. Normalized vorticity contours in semispan wake of VTW7. Contours are labeled with the exponent $n$.

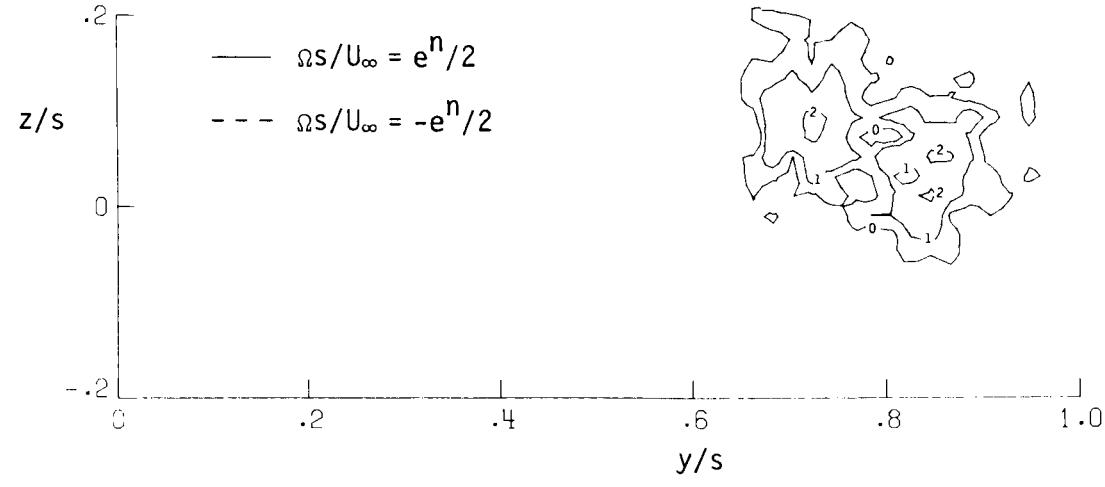


(b) $x/s = 6$.

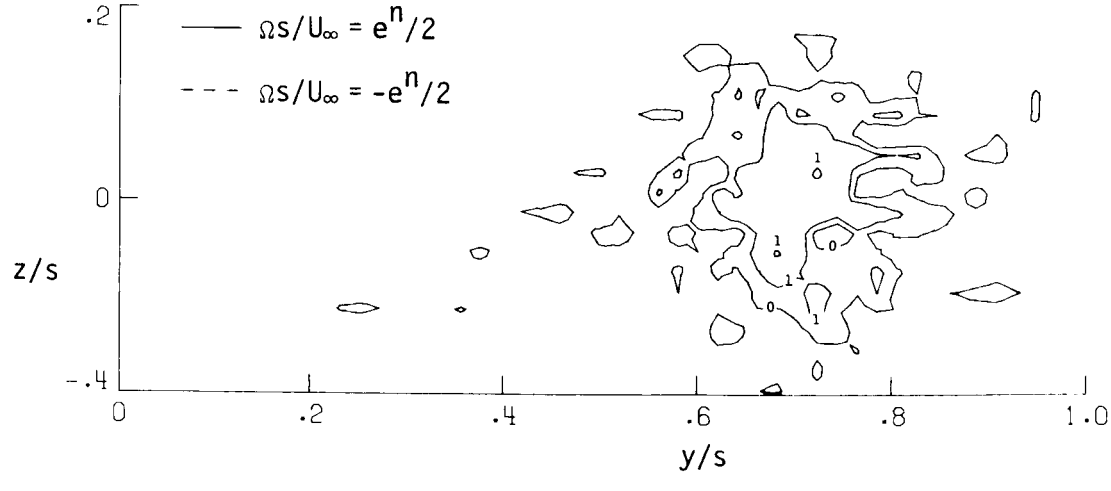


(c) $x/s = 11$.

Figure 20. Concluded.

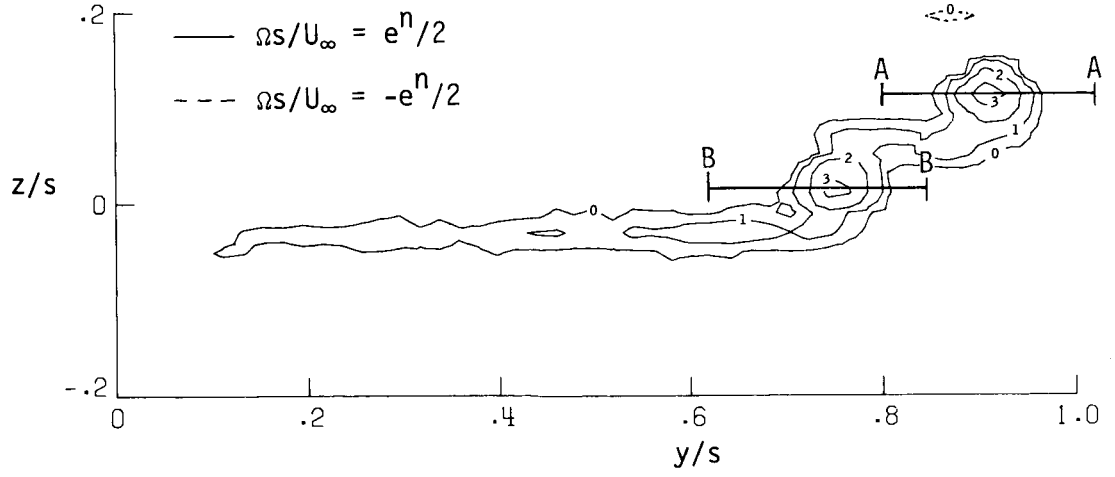


(a) Normalized vorticity field showing spatial position of velocity profiles. Contours are labeled with the exponent $n$.

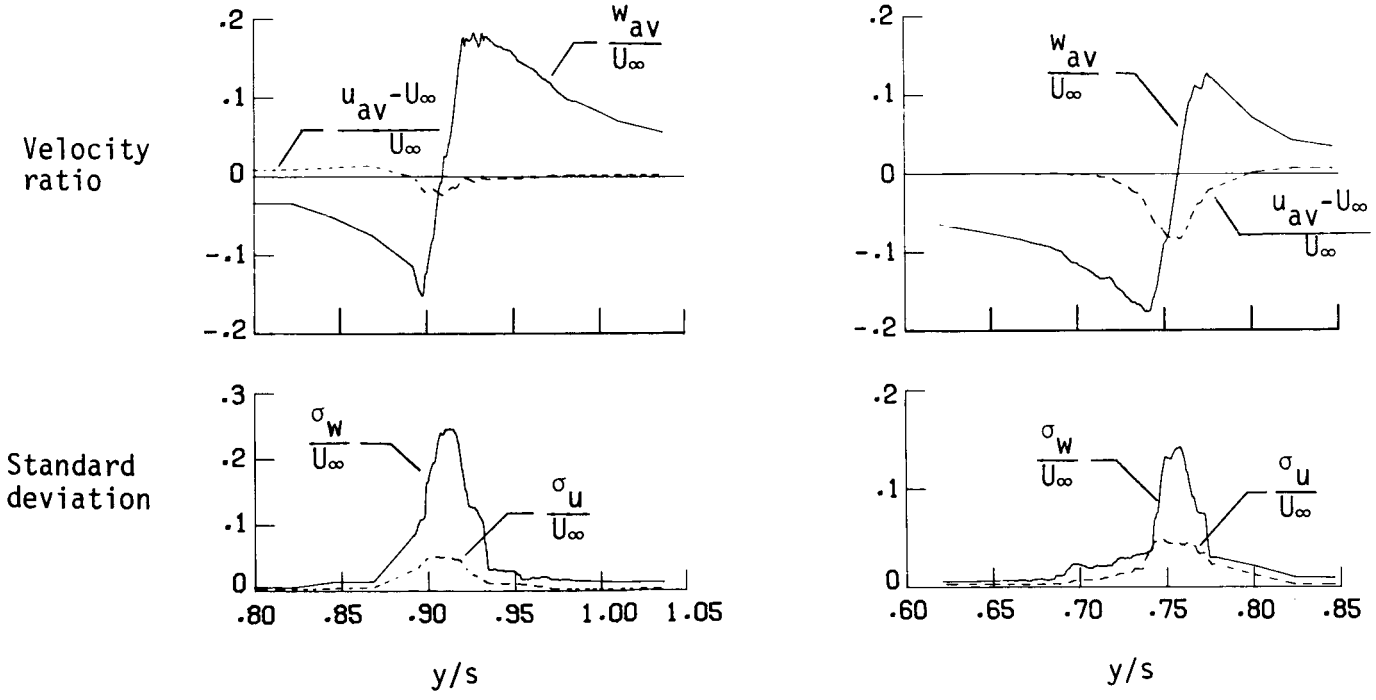


(b) Velocities along path A-A.

(c) Velocities along path B-B.

Figure 21. Normalized vorticity contours and vertical and axial velocity profiles for VTW7 at $x/s = 1$.

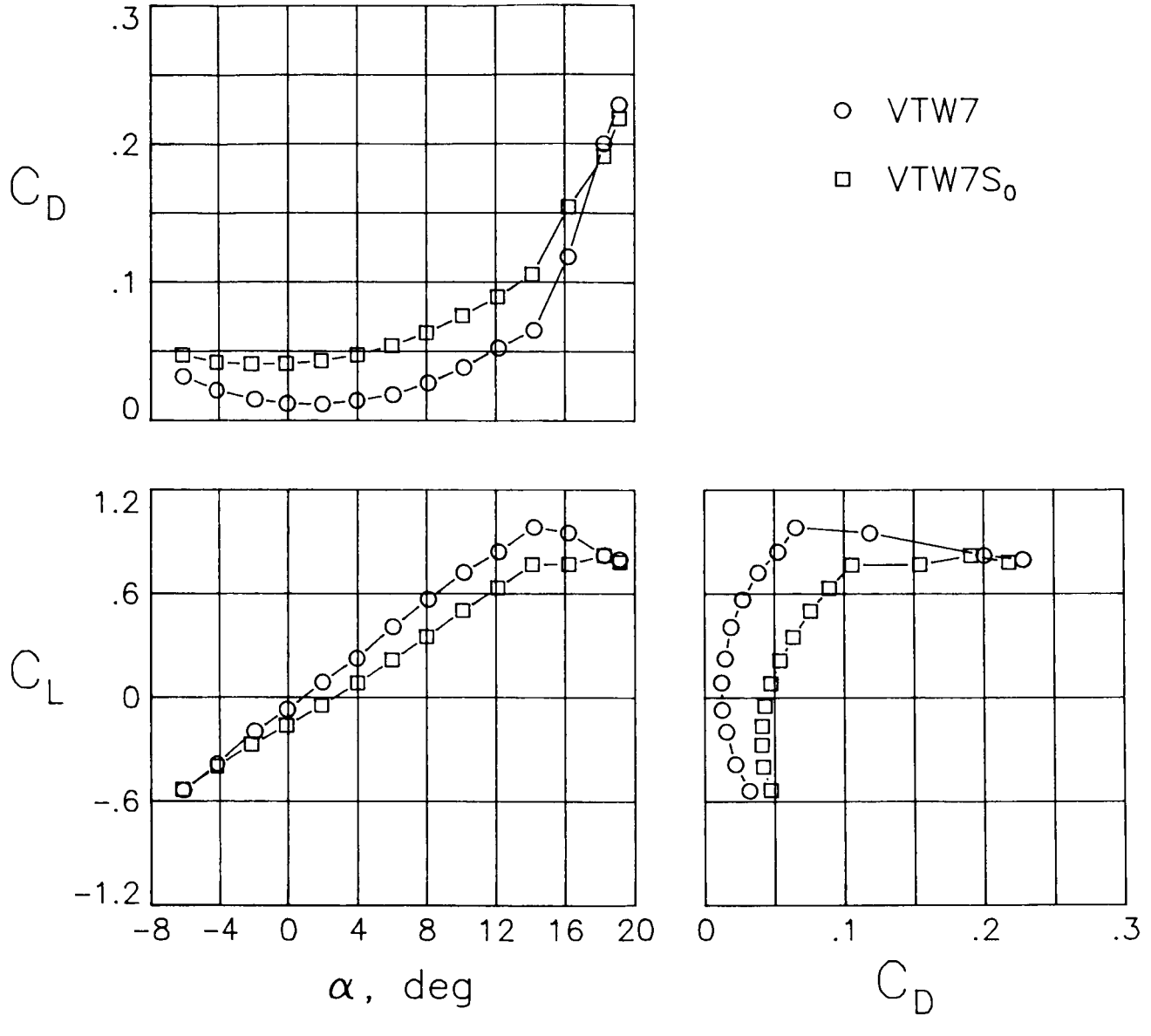


(a) Baseline unalleviated $VTW_7$ and spoiler-alleviated $VTW7S_0$.

Figure 22. Aerodynamic data for VTW configurations in group III alleviated vortex wake configurations.

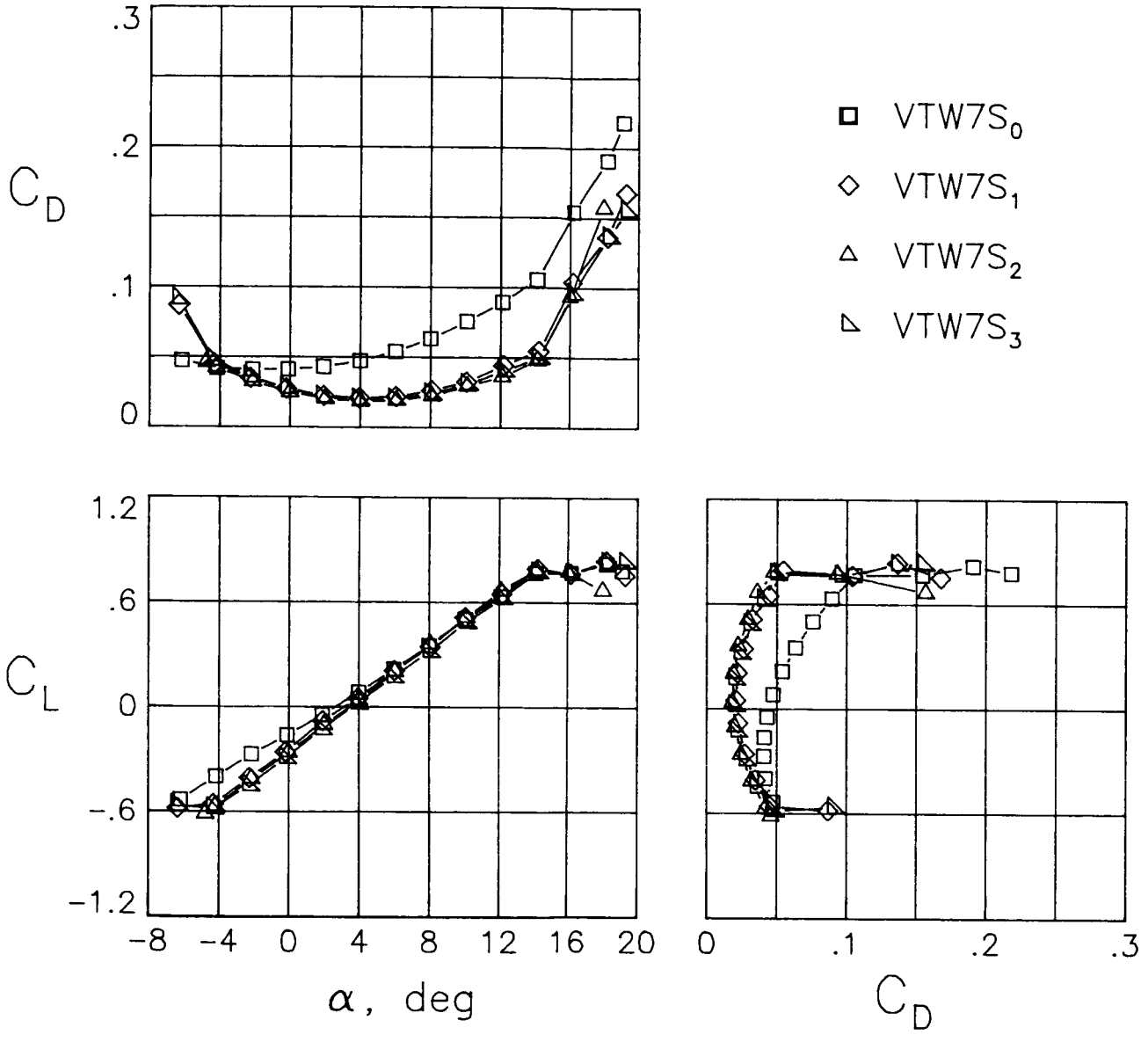


(b) VTW7S$_0$ and configurations using only wing twist to simulate VTW7S$_0$.

Figure 22. Continued.

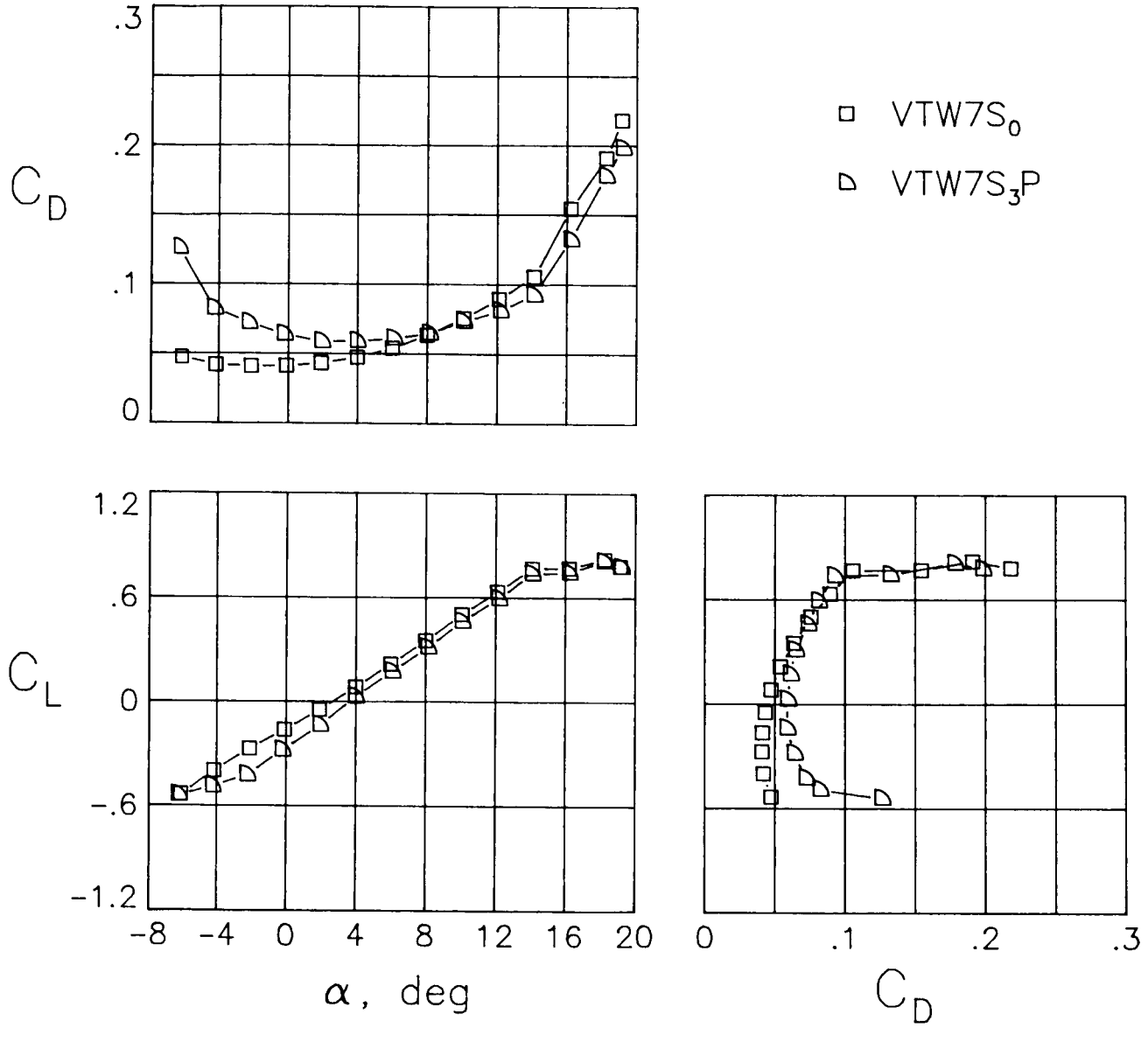


(c) VTW7S$_0$ and VTW7S$_3$P, which used wing twist and drag plates to simulate VTW7S$_0$.

Figure 22. Concluded.

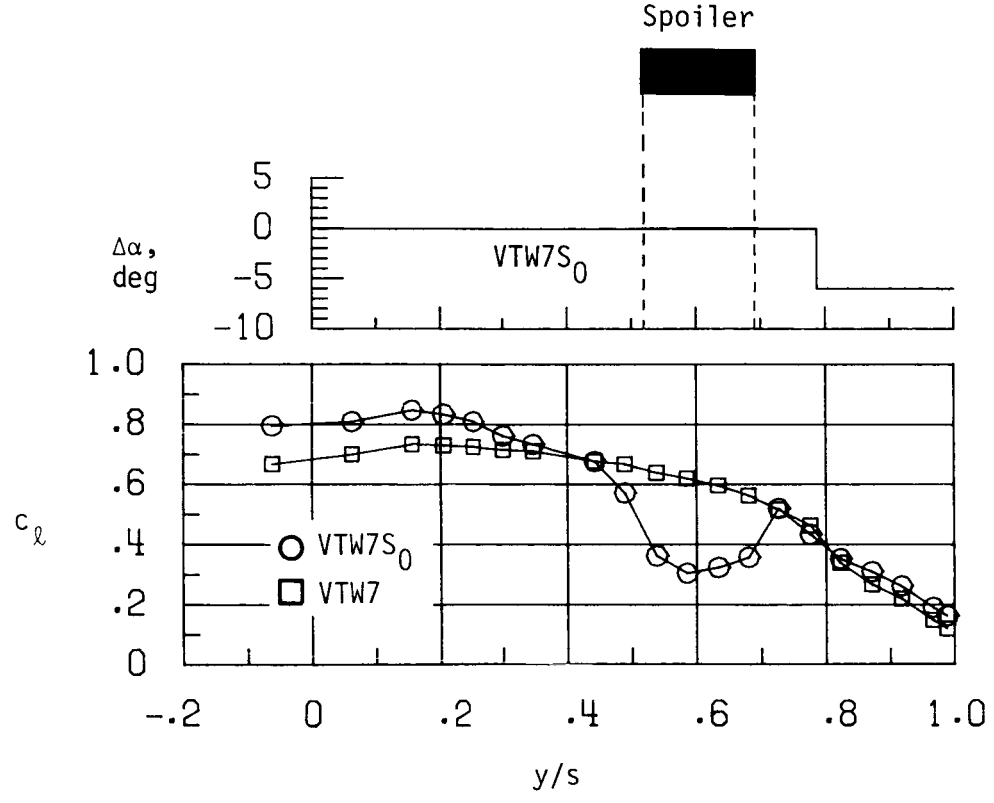


(a) Spoiler-alleviated VTW7$S_0$ and baseline unalleviated VTW7. Prediction not applicable because of spoiler-produced flow separation.

Figure 23. Measured and vortex-lattice-predicted span loads for VTW configurations in group III—alleviated vortex wake configurations.

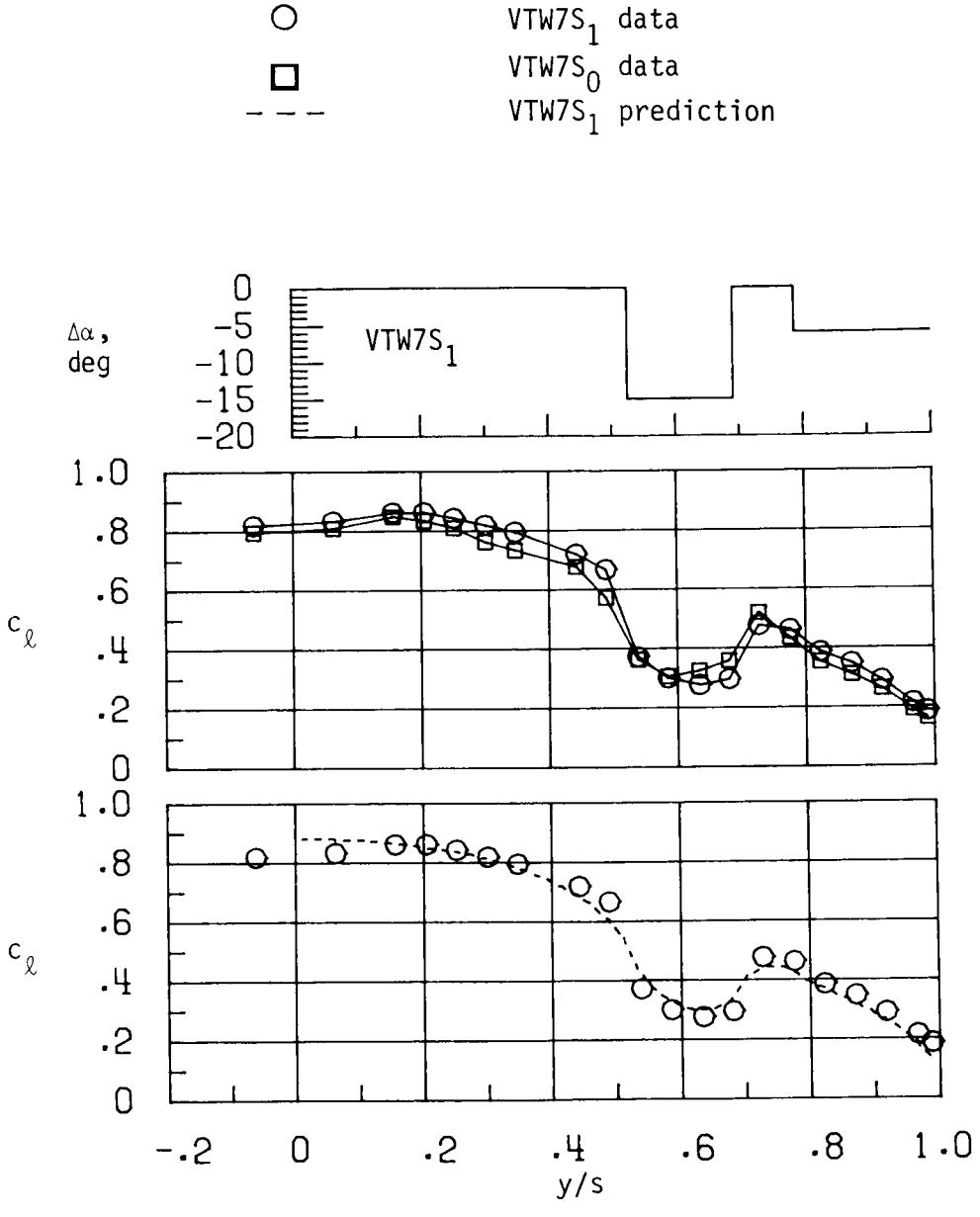


(b) VTW7S$_1$.

Figure 23. Continued.

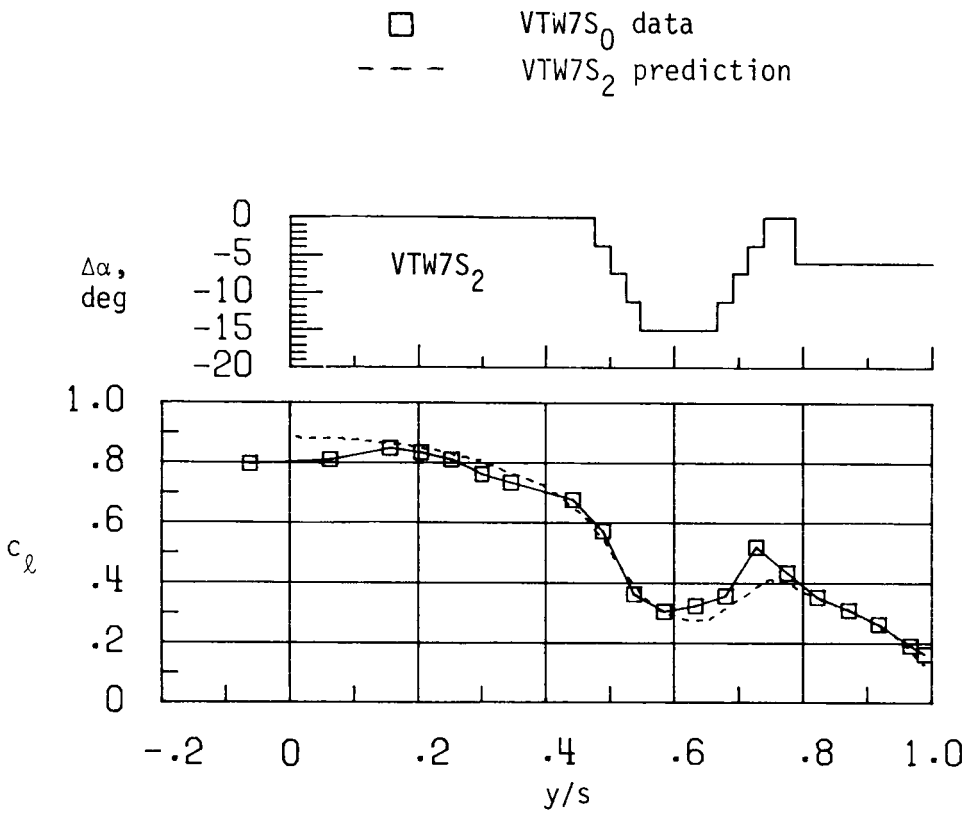


(c) VTW7$S_2$. Span load measurements not made.

Figure 23. Continued.

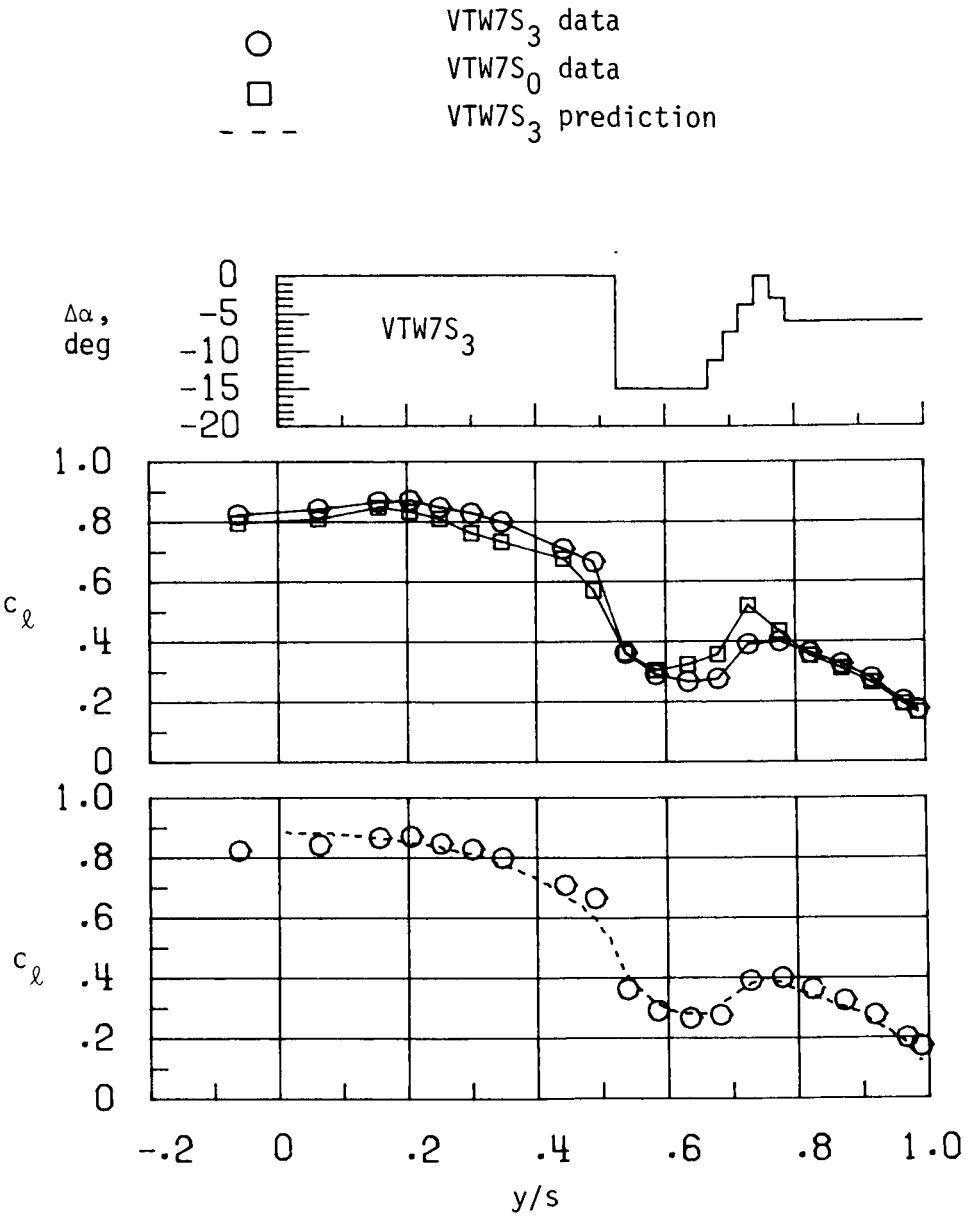


(d) VTW7S$_3$.

Figure 23. Continued.

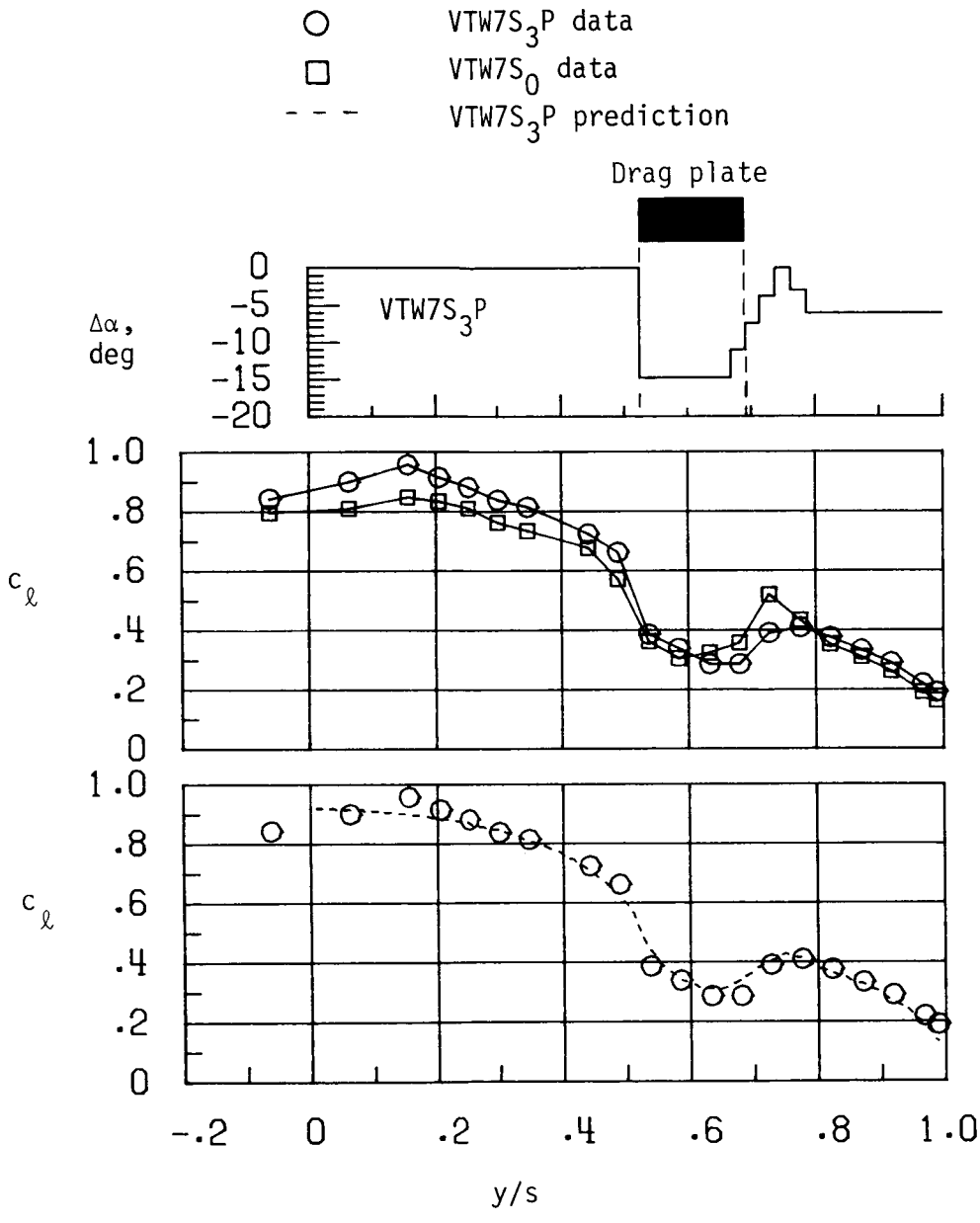


(e) VTW7S$_3$P. Prediction assumes that drag plates do not influence span load.

Figure 23. Continued.

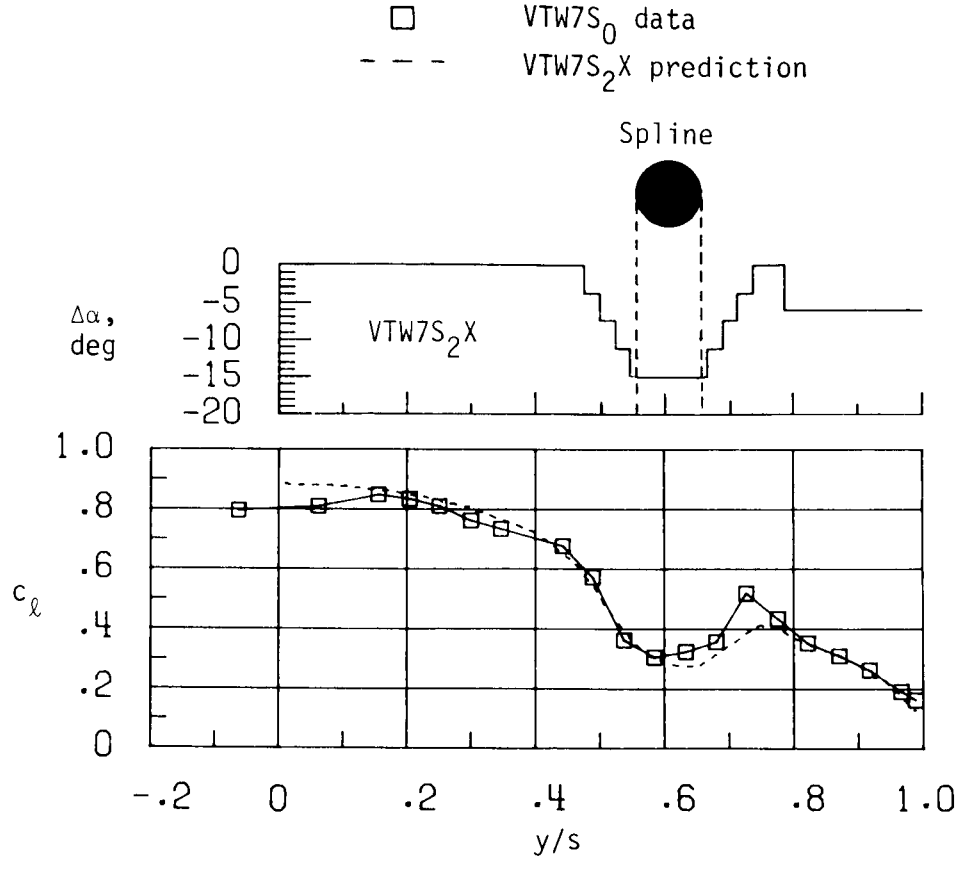


(f) VTW7S$_2$X. Span load measurements not made. Prediction assumes that splines do not influence span load.

Figure 23. Continued.

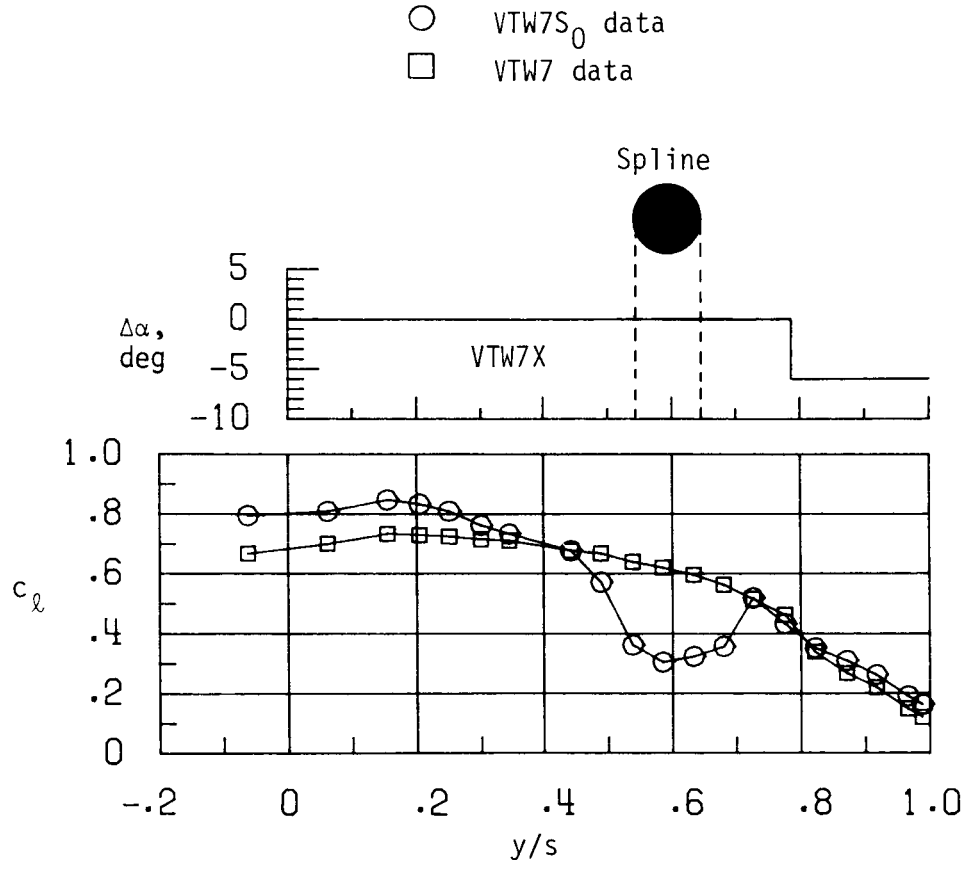


(g) VTW7X. Span load not measured on VTW7X but should be identical to that of VTW7. (VTW7 had the same twist distribution as VTW7X but without the spline.)

Figure 23. Concluded.

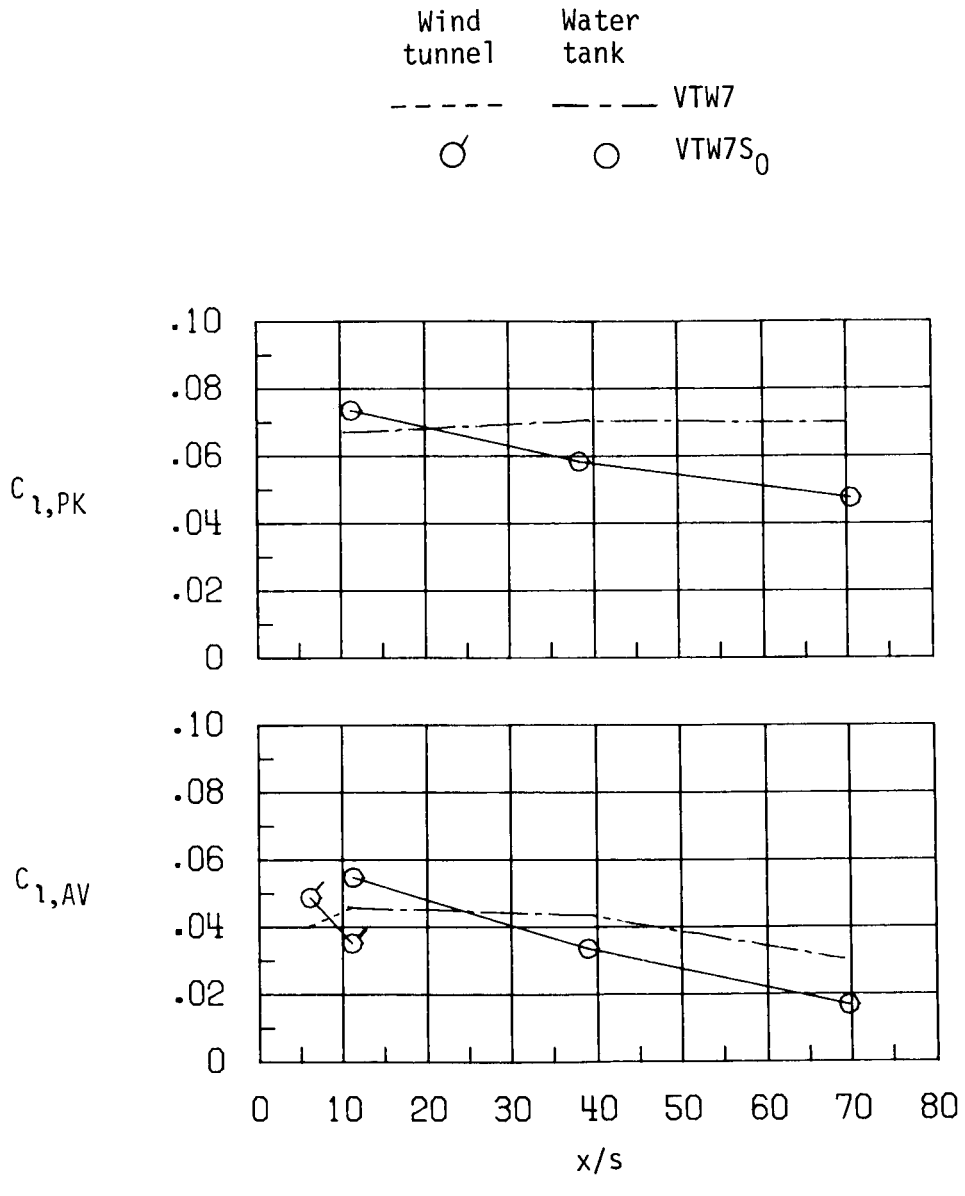


(a) Alleviation produced by addition of spoilers.

Figure 24. Trailing-wing rolling-moment data for VTW configurations in group III—alleviated vortex wake configurations.

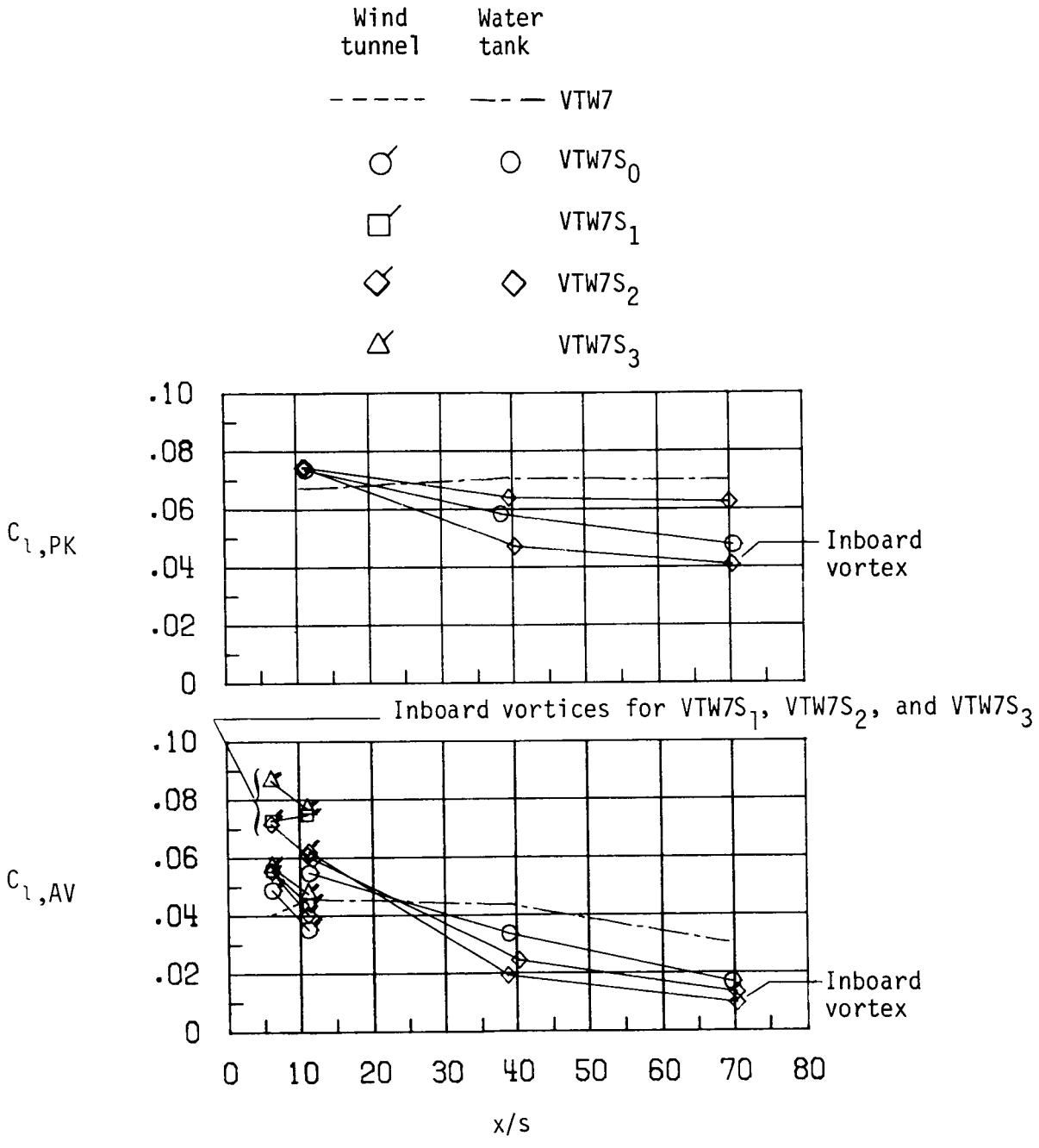


(b) Baseline unalleviated VTW7, spoiler-alleviated $VTW7S_0$, and configurations using only wing twist to simulate $VTW7S_0$.

Figure 24. Continued.

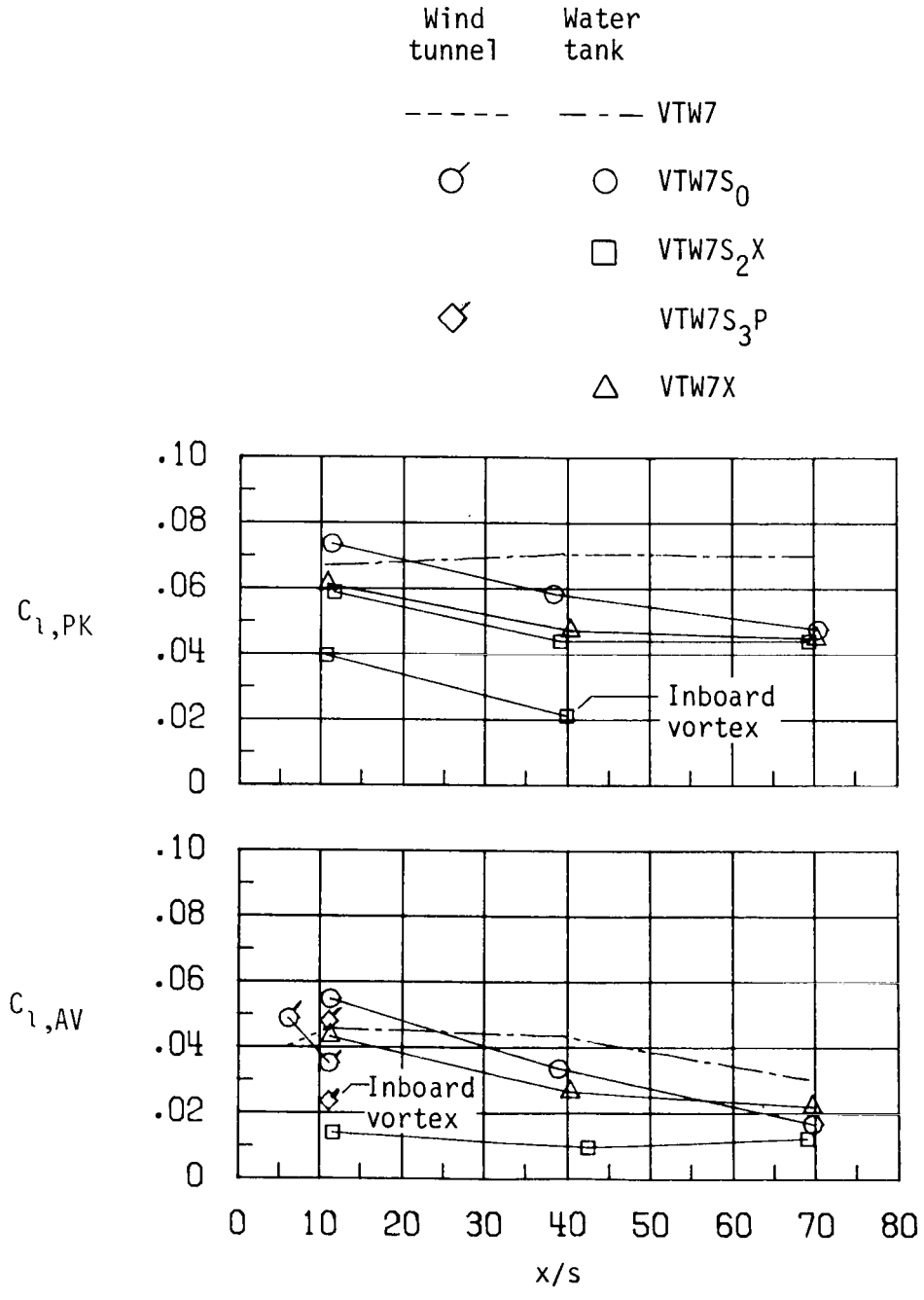


(c) Baseline unalleviated VTW7, spoiler-alleviated VTW7S$_0$, and configurations using splines or drag plates to simulate VTW7S$_0$.

Figure 24. Concluded.

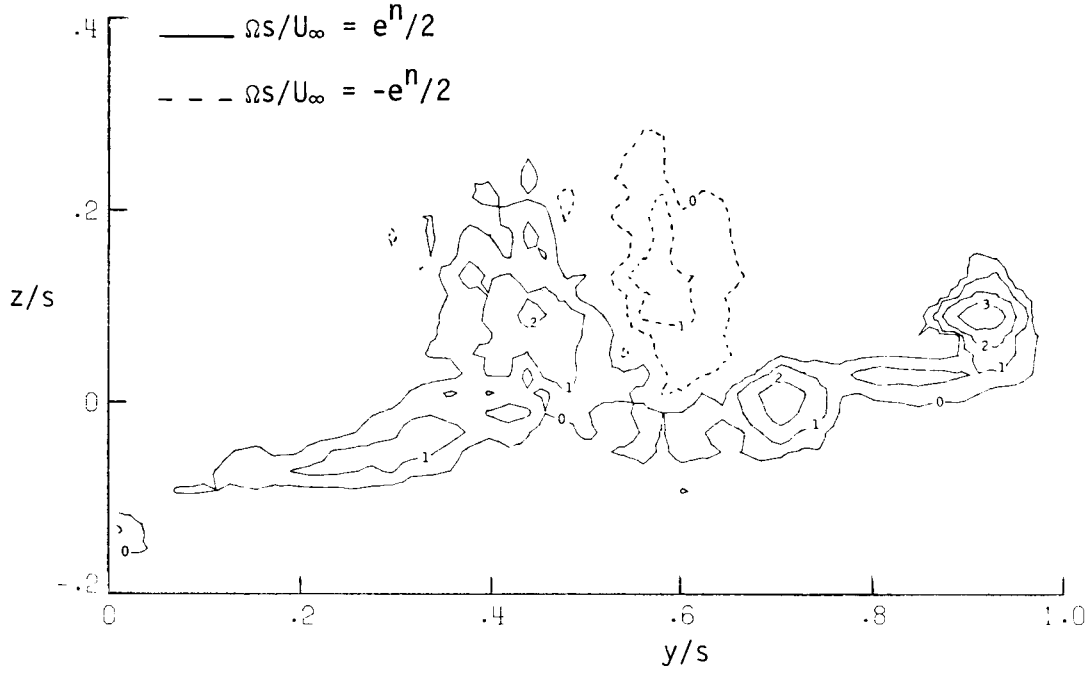


(a) $x/s = 1$.

Figure 25. Normalized vorticity contours in semispan wake of VTW7$S_0$. Contours are labeled with the exponent $n$.

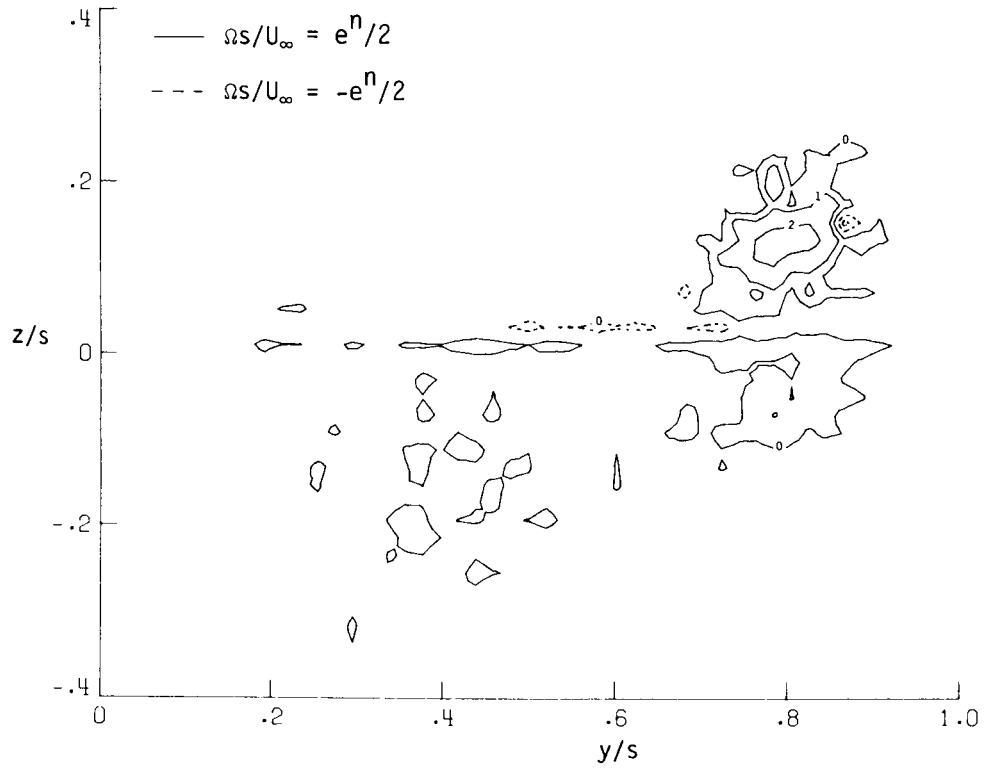


(b) $x/s = 6$.

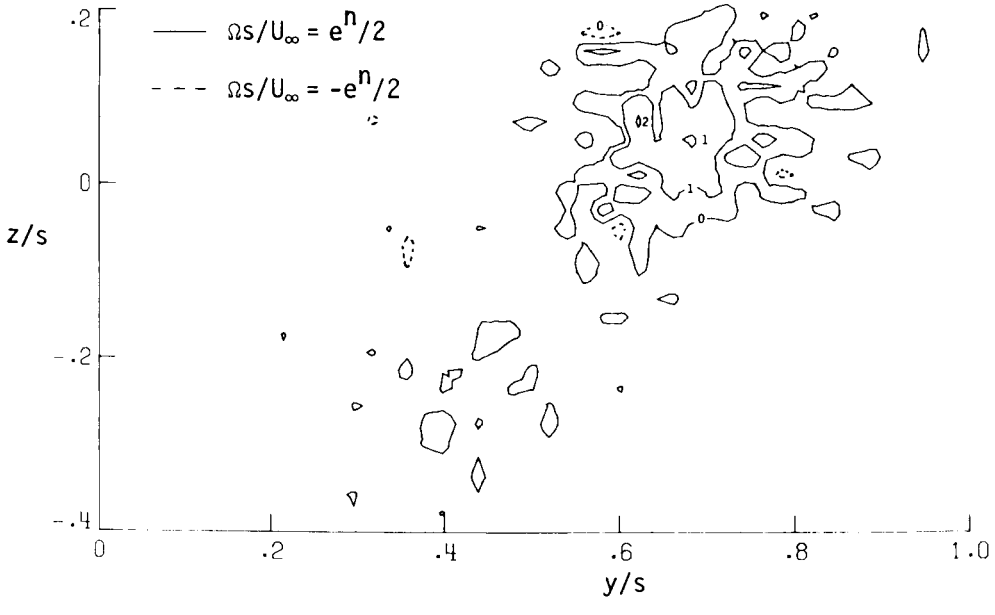


(c) $x/s = 11$.

Figure 25. Concluded.

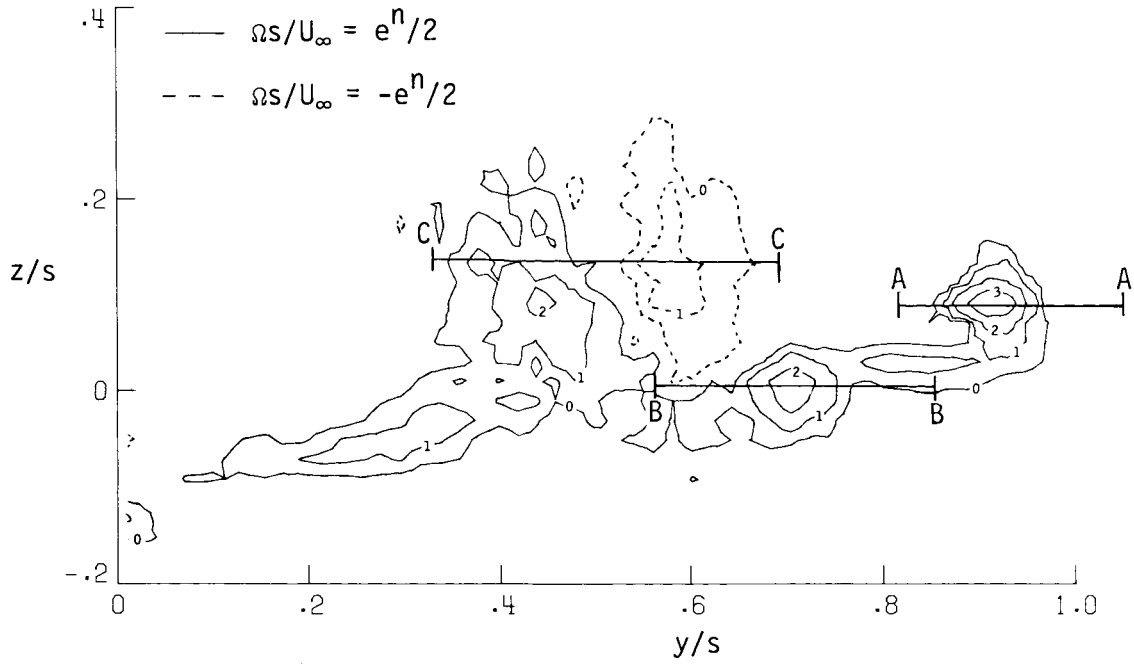


(a) Normalized vorticity field showing spatial position of velocity profiles. Contours are labeled with the exponent $n$.

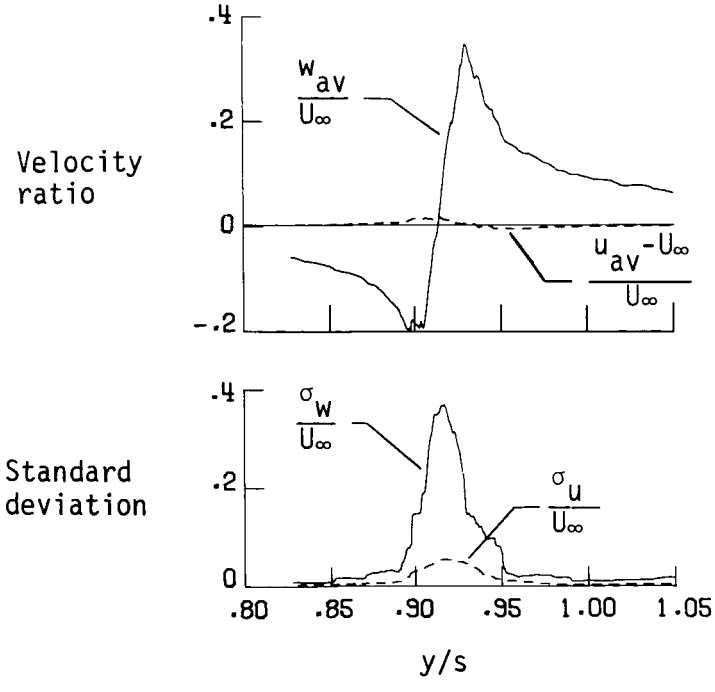


(b) Velocities along path A-A.

Figure 26. Normalized vorticity contours and vertical and axial velocity profiles for VTW7S$_0$ at $x/s = 1$.

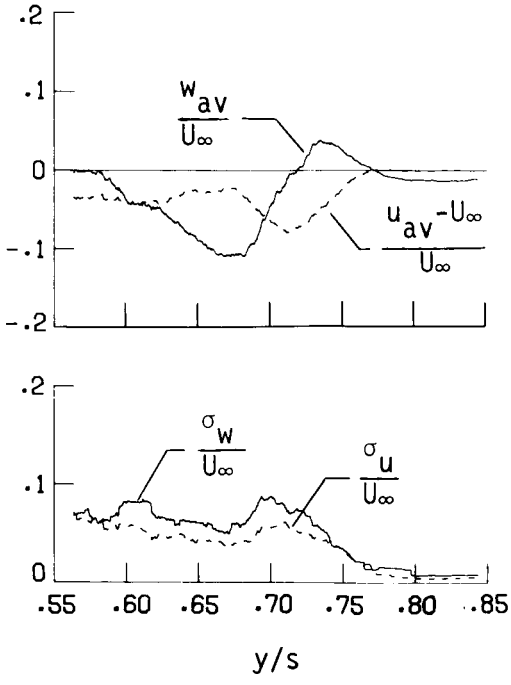


(c) Velocities along path B-B.

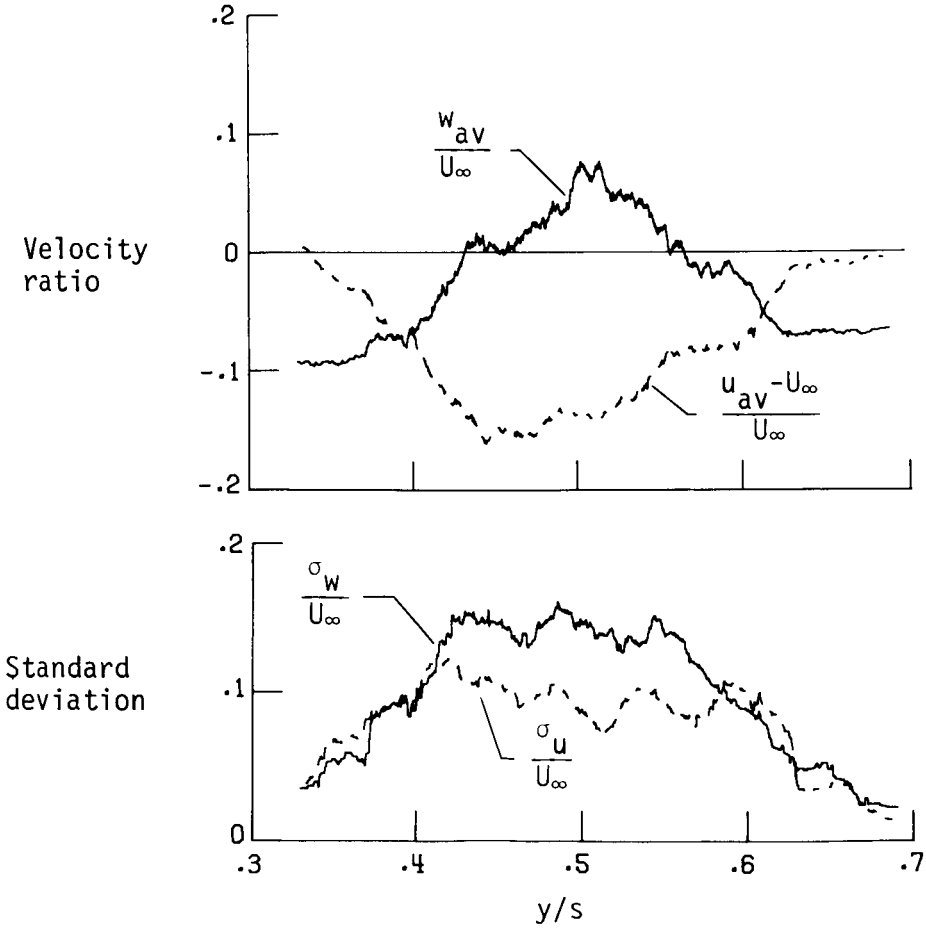


(d) Velocities along path C-C.

Figure 26. Concluded.

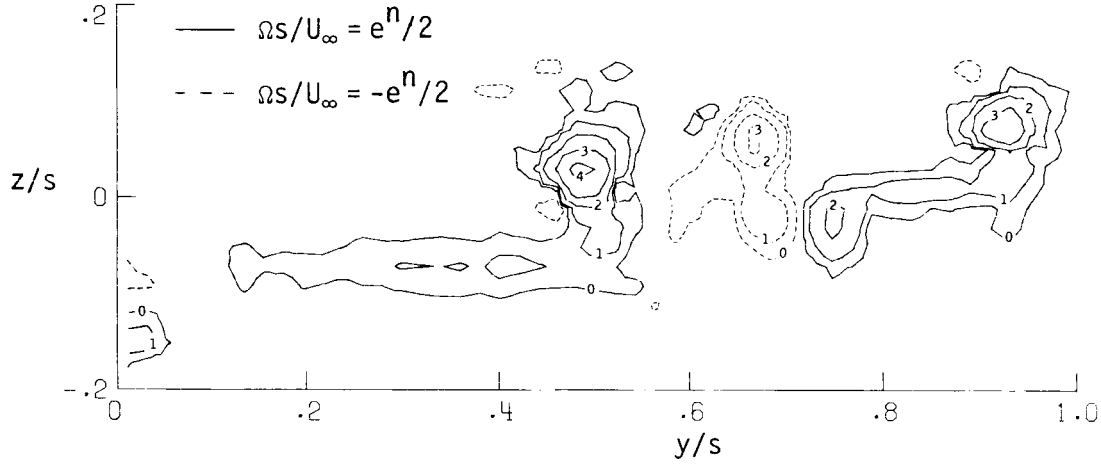


(a) $x/s = 1$.

Figure 27. Normalized vorticity contours in semispan wake of VTW7S3. Contours are labeled with the exponent $n$.

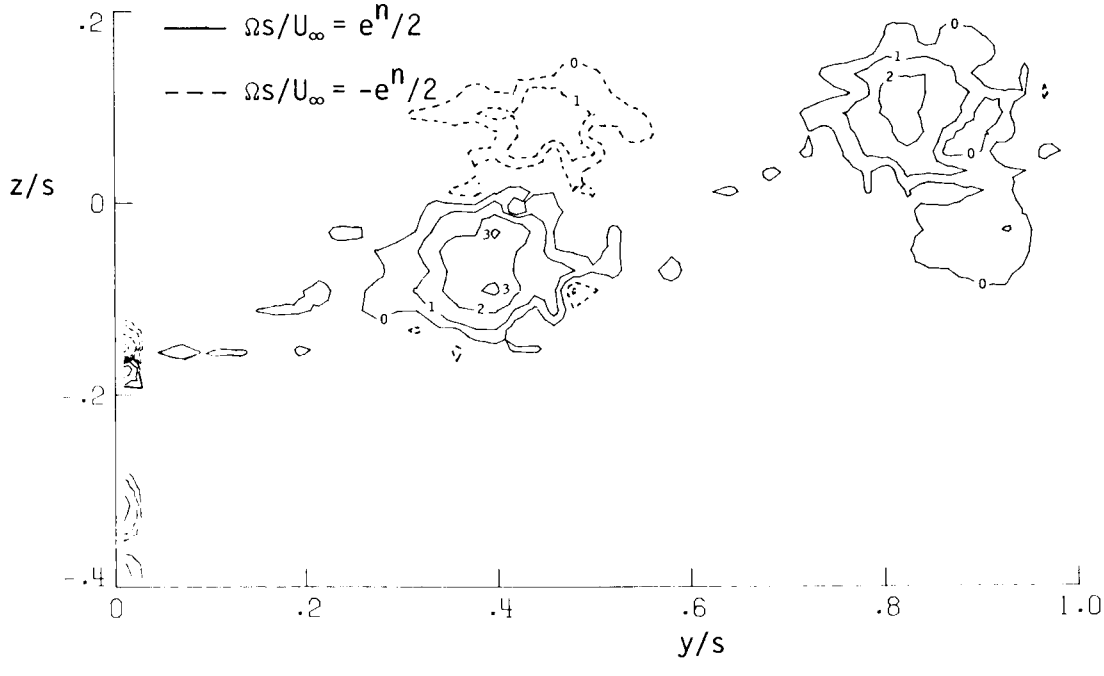


(b) $x/s = 6$.

Figure 27. Continued.

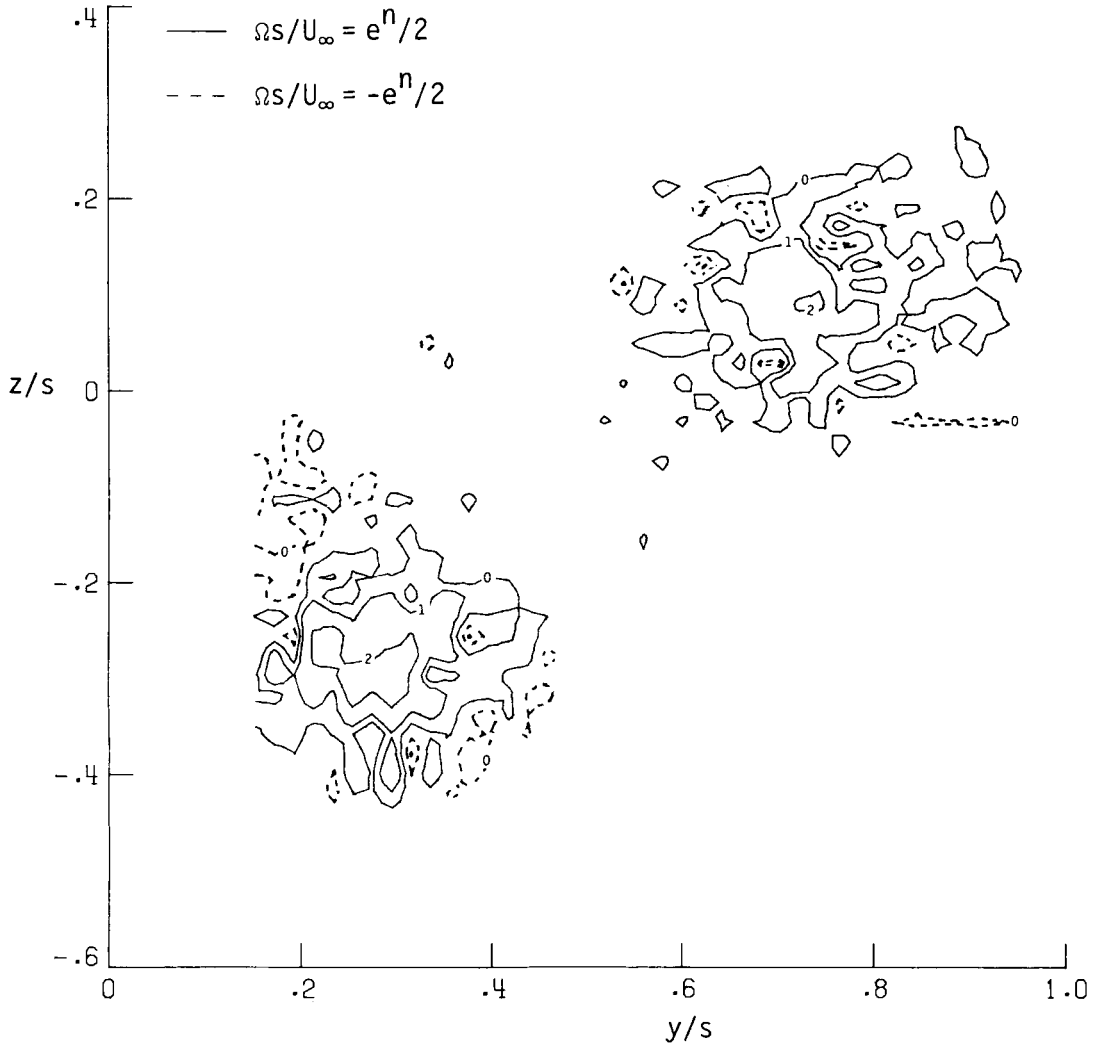


(c) $x/s = 11$. (Data not available inboard of $x/s = 0.15$.)

Figure 27. Concluded.

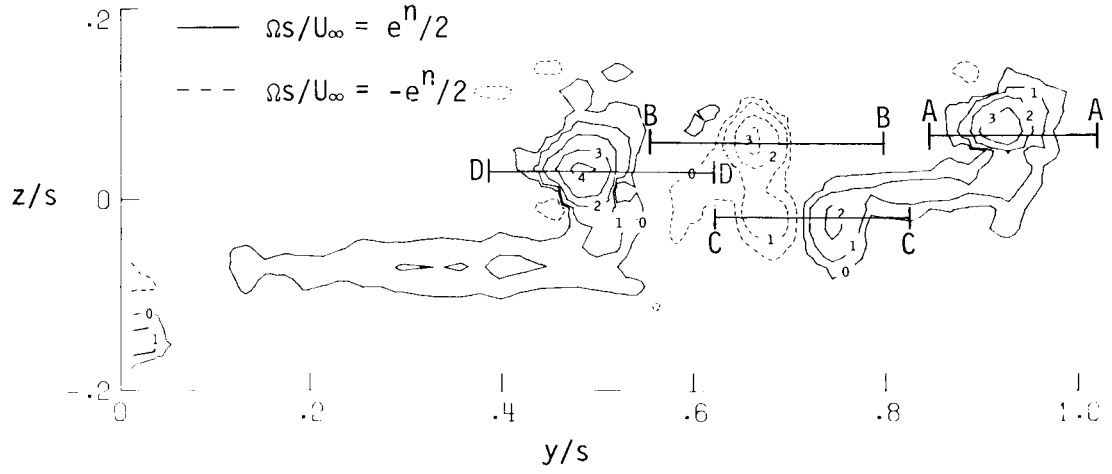


(a) Normalized vorticity field showing spatial position of velocity profiles. Contours are labeled with the exponent $n$.

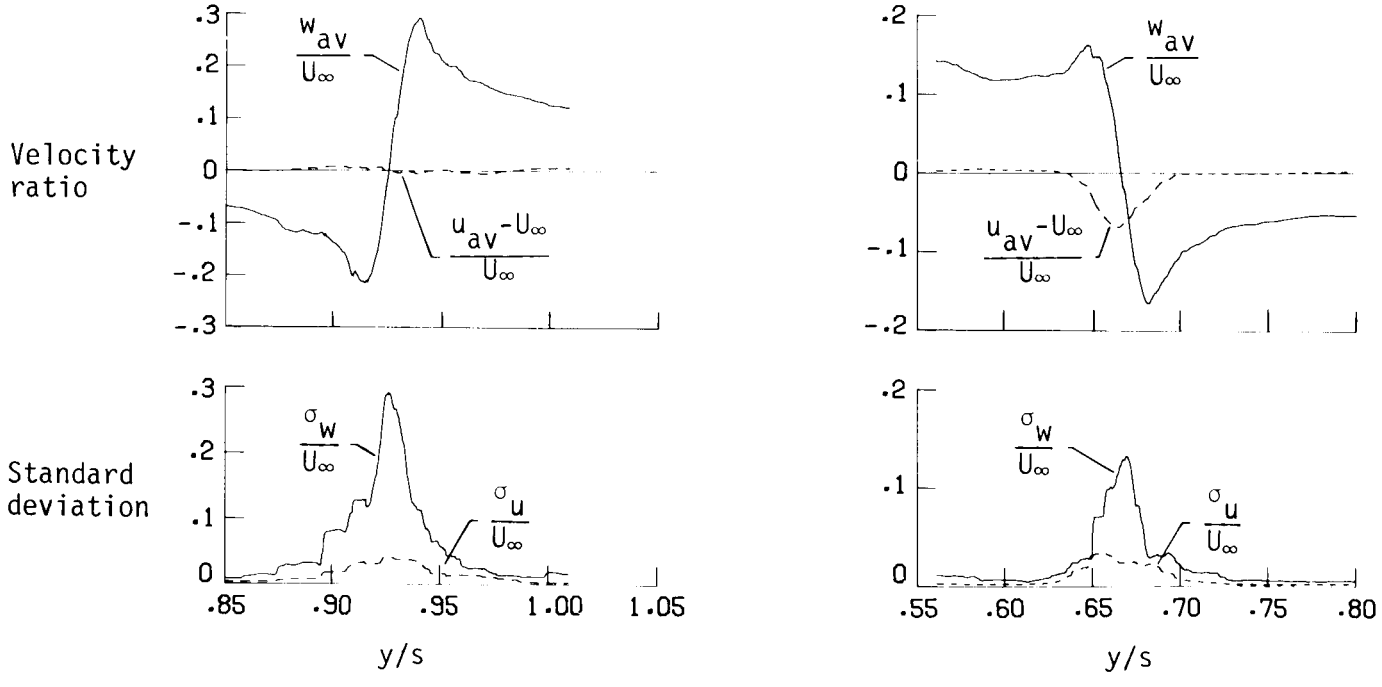


(b) Velocities along path A-A.

(c) Velocities along path B-B.

Figure 28. Normalized vorticity contours and vertical and axial velocity profiles for VTW7S$_3$ at $x/s = 1$.

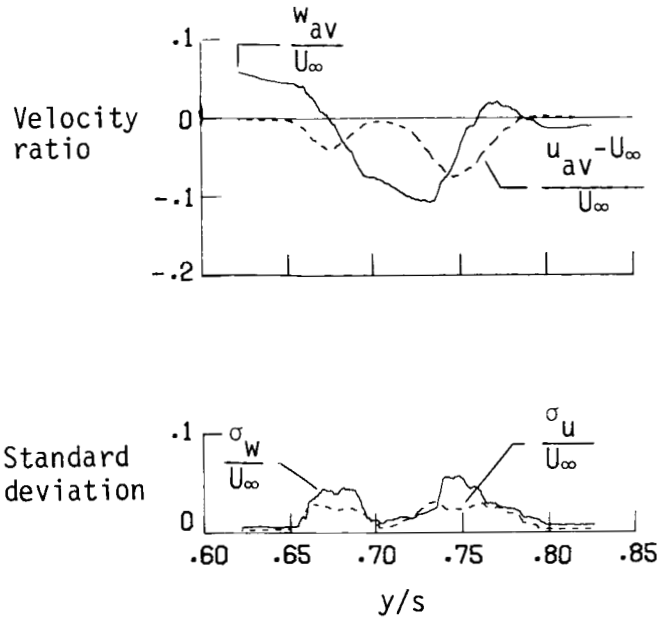


(d) Velocities along path C-C.

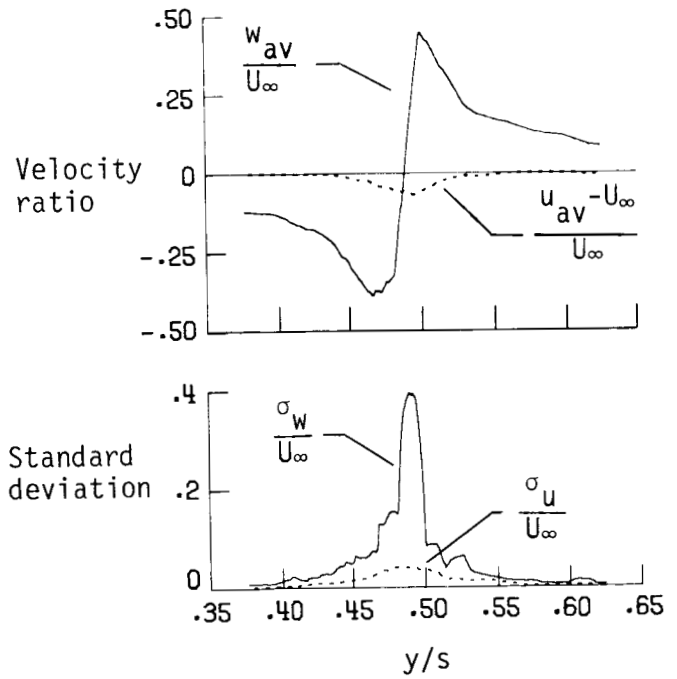


(e) Velocities along path D-D.

Figure 28. Concluded.

# Appendix A

## Test Method Details

The following sections describe in depth the measurement techniques used in the wind tunnel and the water tank.

### Aerodynamic Data

Longitudinal aerodynamic data ($C_L$ and $C_D$) were taken from an $\alpha$ of $-4°$ to beyond stall in $\alpha$ increments of 2° in the wind tunnel for each VTW configuration. With the exception of the untwisted wing configuration (VTW1), longitudinal aerodynamic data were taken only at a $C_L$ of 0.6 in the water tank test.

Figure A1 presents a comparison of the relative positions of the VTW model to the wind tunnel and water tank walls. Blockage and jet boundary corrections were applied to the wind tunnel data according to the methods of references 35 and 36, respectively. Because these corrections were negligible and the test section dimensions were similar, the corrections were not applied to the water tank data.

Significant drag errors were possible in both test facilities because of the high design loads of the normal and axial beams used in the force balances. Maximum balance errors in normal force (directed perpendicular to the VTW center chord) and in axial force (directed parallel to the VTW center chord) were ±5.0 and ±2.5 lbf, respectively, in the wind tunnel and ±5.0 and ±7.5 lbf, respectively, in the water tank. At a Reynolds number of $1 \times 10^6$, $C_L = 0.6$, $C_D = 0.033$, and $\alpha = 12.5°$, these measurement errors translate into possible lift and drag error ranges of ±4.5 and ±53 percent, respectively, in the wind tunnel and ±1.1 and ±25 percent, respectively, in the water tank. The particularly poor drag resolution represents a possible $C_D$ error of ±0.018 in the wind tunnel and ±0.008 in the water tank.

The data signals in both test facilities were low-pass filtered and averaged over long time periods to remove the effects of model vibrations, flow turbulence, and $q_\infty$ fluctuations. In the wind tunnel, a 50-point average was taken by sampling 10 points per second for 5 seconds from a 0.1-Hz low-pass-filtered data signal. In the water tank, a 6500-point average was taken by sampling 650 points per second for 10 seconds from a 30-Hz low-pass-filtered data signal. Although these techniques could not improve the measurement accuracy, they brought the overall repeatability for $C_L$ to within ±3 percent in both facilities and improved the $C_D$ repeatability to within ±7 percent in the wind tunnel and ±3 percent in the water tank.

### Span Load Data

Pressure distribution measurements were taken on all but one of the wind-tunnel-tested VTW configurations (VTW7S$_2$). Electronic scanning pressure transducers were incorporated within VTW wing segments to allow computer-program-controlled recording of all 580 pressure orifice values in about 0.1 sec. This report emphasizes span load data derived from the pressure distribution measurements. Complete chordwise and spanwise $c_p$ measurements for the wind-tunnel-tested VTW configurations are given in reference 28.

VTW wing lift distributions were derived from the pressure distribution data by cosine transformation of each chordwise-integrated $c_n$ through its local angle of attack ($\alpha + \Delta\alpha$) to get local $c_\ell$ values. Each chordwise $c_n$ was arrived at by chordwise trapezoid integration of the 29 $c_p$ measurements at that spanwise station, with a trailing-edge $c_p$ value assigned as the mean of the most aft upper and lower surface $c_p$ measurements. A cubic spline fit of the 19 spanwise $c_\ell$ measurements obtained for the right wing was then integrated with the centerline $c_\ell$ set equal to the measured $c_\ell$ at $y/s = 0.0612$ and the wing-tip $c_\ell$ set equal to zero. This integration of $C_{L,p}$ thus assumed no lift on the body-of-revolution wing-tip caps, no modification due to the presence of the body, and equal lift on the right and left wings. The latter assumption was justified by the measurement of negligible rolling moment on the VTW during the test runs. Left-of-centerline $c_\ell$ values measured at $y/s = -0.0612$ were disregarded since their values were lowered by centerbody blockage of local lower-surface wing flow, which was caused by a small right-to-left flow angularity (as determined by the wake survey data in appendix B). Since no pressure distribution measurements were made on the centerbody or along the wing centerline, the effect of the centerbody was not included in the $C_{L,p}$ integration.

The accuracy of the electronic scanning pressure transducers was specified as ±96 Pa with about 80 percent of the transducers having no more than ±46 Pa error. If the transducer errors were randomly distributed over the wing, the integrated $c_n$ values should be correct to within ±0.02 and the integrated $C_{L,p}$ should be correct to within ±0.006 (±1 percent of the nominal 0.6 $C_L$). An additional source of $c_\ell$ and $C_{L,p}$ error was due to ignoring the local chordwise (or axial) forces in the integrations. Examination of the chordwise contribution to both high- and low-drag VTW configurations at wing segments with small and large $c_\ell$ values and at wing segments with the spoilers installed revealed a resultant error typically in the range of ±1 percent but not more than

±3 percent. Thus overall error in the $C_{L,p}$ values can typically be expected to be ±2 percent but not more than ±4 percent. These error ranges are with respect to lift on the wing alone and do not account for neglect of the centerbody lift, which was a function of the angle of attack and thus varied for each VTW configuration.

Pressure distribution measurements enabled the computation of several two-dimensional span load parameters which interrelate the wing lift distribution and the downstream wake vorticity distribution. (See ref. 11.) Specifically, the lift centroid $\bar{s}$, wing centerline circulation $\Gamma_o$, vorticity centroid $\bar{b}/2$, and vorticity dispersion radius $\bar{d}$ were calculated from a spline fit to the right-wing lift distribution measurements by:

$$\frac{\bar{s}}{s} = \frac{1}{C_{L,p}} \int_0^1 (y/s)\, c_\ell\, d(y/s)$$

$$= \frac{s}{(\bar{b}/2)\Gamma_o} \int_0^1 (y/s)\, \Gamma'\, d(y/s)$$

$$\frac{\Gamma_o}{U_\infty s} = \frac{-1}{U_\infty s} \int_0^s d\Gamma' = \frac{-c}{b} \int_0^s dc_\ell = \frac{c_{\ell,o}}{A}$$

$$\frac{\bar{b}}{b} = \frac{-1}{c_{\ell,o}} \int_0^1 (y/s)\, \frac{dc_\ell}{d(y/s)}\, d(y/s)$$

$$= \frac{-1}{\Gamma_o} \int_0^1 (y/s)\, \frac{d\Gamma'}{d(y/s)}\, d(y/s)$$

$$= \frac{(\bar{b}/2)\Gamma_o}{s\Gamma_o} = \frac{C_{L,p}}{c_{\ell,o}}$$

$$\frac{\bar{d}}{s} = \left\{ \frac{-1}{c_{\ell,o}} \int_0^1 [(y/s) - (\bar{b}/b)]^2\, \frac{dc_\ell}{d(y/s)}\, d(y/s) \right\}^{1/2}$$

$$= \left\{ \frac{-1}{\Gamma_o} \int_0^1 [(y/s) - (\bar{b}/b)]^2\, \frac{d\Gamma'}{d(y/s)}\, d(y/s) \right\}^{1/2}$$

Generally, $\bar{s}$ and $\Gamma_o$ define the distribution of the wing lift with a total lift set by $C_{L,p}$, whereas $\bar{b}/2$ and $\bar{d}$ define the distribution of the vorticity with the net semispan vorticity set by the wing centerline circulation $\Gamma_o$. The dispersion radius was calculated to only two significant digits because of the dominant radius-squared effect at the high-gradient wing-tip region. All parameters were computed with the wing lift distribution measurements scaled to reflect a $C_{L,p} = 0.6$ test condition. This adjustment was made to facilitate comparisons between VTW configurations. Similarly, $\bar{b}$ and $\Gamma_o$ measured on the wing can be compared with $\bar{y}$ and $\Gamma$ measured in the downstream wake. The lift and vorticity distributions on the wing are linked by the product $(\bar{b}/2)\Gamma_o$, which is representative of the impulse exerted by the VTW on the flow field per unit volume of fluid. For a given model, $C_{L,p}$, and $U_\infty$, the value of $(\bar{b}/2)\Gamma_o$ is necessarily a constant regardless of the configuration lift distribution. This quantity is given by

$$(\bar{b}/2)\Gamma_o = \frac{C_{L,p} q_\infty sc}{\rho U_\infty}$$

$$= \frac{1}{2} C_{L,p} U_\infty sc$$

$$= \frac{C_{L,p} U_\infty s^2}{A}$$

In the wind tunnel investigation, with $C_{L,p} = 0.6$, the $(\bar{b}/2)\Gamma_o$ was about 5.4 $m^3$/sec.

At the time of this investigation, the wind tunnel computer system was incapable of generating a complete span load from all 580 pressure orifice data points while simultaneously operating the data acquisition program. Instead, an additional on-line computer program utilized about half of the chordwise and spanwise orifice measurements to produce rough plots of span load for each VTW configuration while it was being tested in the wind tunnel. The inherent lack of accuracy in the rough span load calculations resulted in the span loads of VTW configurations in group III not exactly matching that of $VTW7S_0$.

## Trailing-Wing Rolling-Moment Data

Trailing-wing data were taken in both test facilities with the VTW at $C_L = 0.6$. Trailing-wing rolling-moment measurements were made at four downstream distances; near-field data were taken in the wind tunnel, and far-field data (with a near-field overlap) were taken in the water tank. The trailing-wing internal roll balance signal was processed differently in each facility. These different processing techniques resulted in average coefficient data $C_{l,\mathrm{AV}}$ being obtained in both facilities and peak coefficient data $C_{l,\mathrm{PK}}$ being obtained only in the water tank.

In the wind tunnel, trailing-wing rolling-moment surveys were obtained at two downstream distances, $x/s = 6$ and 11. These distances correspond to two of the three downstream locations for wake velocity surveys. The rolling-moment signal was sent through a 0.1-Hz low-pass filter and then sampled at 10 points per second for 5 sec with the trailing wing at a fixed $x, y, z$ position. The resulting 50 points were then averaged and converted to coefficient form. This process was repeated over the cross plane at a sufficient number of positions to insure that the maximum value of average rolling-moment coefficient had been measured for each vortex of significant strength. The maximum average rolling-moment coefficients

for each wind tunnel $Y$-$Z$ cross plane are presented as $C_{l,\mathrm{AV}}$ data in this report.

In the water tank, trailing-wing rolling-moment surveys were obtained at three downstream distances, $x/s = 11$, 40, and 70. The near-field location ($x/s = 11$) corresponds to the furthest downstream survey location in the wind tunnel. The rolling-moment signal from an 18-sec portion of each test run down the length of the tank was recorded in analog form with an overall frequency response limitation of about 20 Hz. The 18-sec period was conservatively chosen to avoid the stopping wave from the VTW model. (See ref. 37.) During each run, the trailing-wing model traversed 46 cm vertically at 4 cm/sec through the VTW wake at a fixed lateral position. Between runs the trailing-wing lateral position could be changed. Runs were made with the trailing wing at a sufficient number of fixed lateral positions to insure that the maximum instantaneous rolling moment had been measured for each vortex of significant strength. These values were converted to coefficient form for each nominal downstream survey location in the water tank and are presented as $C_{l,\mathrm{PK}}$ in this report. Upon location of the $y, z$ position for each $C_{l,\mathrm{PK}}$, a separate run was made with the trailing wing fixed at that $y, z$ position to obtain an integrated, 18-sec rolling-moment average. This average is noted in coefficient form as $C_{l,\mathrm{AV}}$.

### Wake Velocity Data

Wake velocity surveys were made behind four wing twist configurations (VTW4, VTW7, VTW7$S_0$, and VTW7$S_3$) in the wind tunnel at $x/s = 1$, 6, and 11. As previously noted, the $x/s = 6$ and 11 positions matched the trailing-wing survey positions. At each downstream survey position, $u$, $v$, and $w$ velocities were measured over a cross plane that typically encompassed $0.0 \leq y/s \leq 1.3$ horizontally for all downstream positions and $-0.3 \leq z/s \leq 0.3$ vertically for $x/s = 1$ and $-0.6 \leq z/s \leq 0.3$ vertically for $x/s = 6$ and 11.

Wake velocity measurements were made with three orthogonal hot films mounted to a 46-cm-long probe attached to the traverse mechanism on the wind tunnel survey rig. The three hot-film elements were small enough to be contained by a 3-mm sphere. This compactness allowed good spatial resolution and a minimum of flow field interference. Linearized hot-film voltages from the anemometer and $y, z$ digitally encoded outputs from the traverse mechanism were signal conditioned and recorded on magnetic tape at 15 in/sec in FM intermediate-band format to allow accurate data transcription up to 5 kHz. Additional details on the hot-film sensor, associated instrumentation, and recording techniques can be found in reference 38.

The hot-film probe traversed the cross plane continuously at 1.3 cm/sec along about 55 horizontal rows which were separated vertically by 1.3 cm ($0.01s$) in high-vorticity regions and spread to about 5 cm ($0.04s$) apart near the upper and lower cross plane boundaries. The traversing speed chosen was as low as possible to increase the measurement accuracy of the mean flow characteristics while allowing completion of a cross plane survey within 3 or 4 hours.

After the wind tunnel test, the analog hot-film voltage signals were sampled at 50 points per second, and 100-point running averages and standard deviations of the probe position and flow velocities were computed for each horizontal traverse of the cross plane by the hot-film probe. Since the hot-film probe traversed at 1.3 cm/sec, each 100-point average represented a 2.6-cm ($0.02s$) spatial average and 2.0-sec time average of the data and was separated horizontally by $0.0002s$ from the next 100-point average. Thus, the analog signals measured in each horizontal sweep of the VTW wake were transformed to about 6900 points, at which means and standard deviations of $y$, $z$, $u$, $v$, and $w$ were estimated. This averaging technique was chosen as a compromise between accurate estimation of the mean and fluctuating flow parameters and excessive digitization. Average velocity profiles presented in this report are extracted from this digitized data set.

In order to compute contours of streamwise vorticity at each cross plane, the irregularly spaced rows of $u_{av}$, $v_{av}$, and $w_{av}$ velocities were linearly interpolated to a uniform, $0.02s$-mesh grid of $\bar{u}$, $\bar{v}$, and $\bar{w}$ velocities. The line integral of velocity around the square per unit area was computed to yield streamwise vorticity $\Omega$ at the center of each grid square. This computation is identical to the more common formulation of streamwise vorticity obtained by differencing the $\partial w/\partial y$ and $\partial v/\partial z$ derivatives. As illustrated in figure A2, this calculation proceeds as follows:

$$\underset{\substack{\text{At grid}\\ \text{square center}}}{\Omega} = \frac{1}{(\Delta \ell)^2} \underset{\substack{\text{Around}\\ \text{grid square}}}{\oint} U \cdot d\ell$$

$$= \frac{\partial w}{\partial y} - \frac{\partial v}{\partial z} \simeq \frac{d\bar{w}}{dy} - \frac{d\bar{v}}{dz}$$

$$\Omega \simeq \frac{1}{2}\left[\left(\frac{d\bar{w}}{dy}\right)_i + \left(\frac{d\bar{w}}{dy}\right)_{i+1}\right] - \frac{1}{2}\left[\left(\frac{d\bar{v}}{dz}\right)_j + \left(\frac{d\bar{v}}{dz}\right)_{j+1}\right]$$

$$\Omega \simeq \frac{(\bar{w}_{i,j+1} - \bar{w}_{i,j}) + (\bar{w}_{i+1,j+1} - \bar{w}_{i+1,j})}{2(y_{i+1} - y_i)} - \frac{(\bar{v}_{i+1,j} - \bar{v}_{i,j}) + (\bar{v}_{i+1,j+1} - \bar{v}_{i,j+1})}{2(z_{j+1} - z_j)}$$

$$\Omega \simeq \frac{1}{2(0.02s)}[\bar{w}_{i,j+1} - \bar{w}_{i,j} + \bar{w}_{i+1,j+1} - \bar{w}_{i+1,j} - \bar{v}_{i+1,j} + \bar{v}_{i,j} - \bar{v}_{i+1,j+1} + \bar{v}_{i,j+1}]$$

Level values of normalized vorticity ($\Omega s/U_\infty$) were then plotted at each cross plane. Vorticity contour levels of

$$\Omega s/U_\infty = \pm e^n/2, \; n = 0, \; 1, \; 2 \; \ldots$$

were chosen to reflect the qualitative nature of the data and avoid the difficulties of densely packed contours in high vorticity gradient regions.

The interpolated velocities were also used to compute the total circulation:

$$\Gamma = \iint_{\substack{\text{Cross} \\ \text{plane}}} \Omega \, dy \, dz = \oint_{\substack{\text{Cross} \\ \text{plane} \\ \text{boundary}}} U \cdot d\ell$$

and the lateral vorticity centroid position:

$$\bar{y} = \frac{(\bar{y}\Gamma)}{\Gamma} = \frac{1}{\Gamma} \iint_{\substack{\text{Cross} \\ \text{plane}}} \Omega \, dy \, dz$$

for comparison with their counterparts measured on the VTW ($\Gamma_o$ and $\bar{b}/2$, respectively).

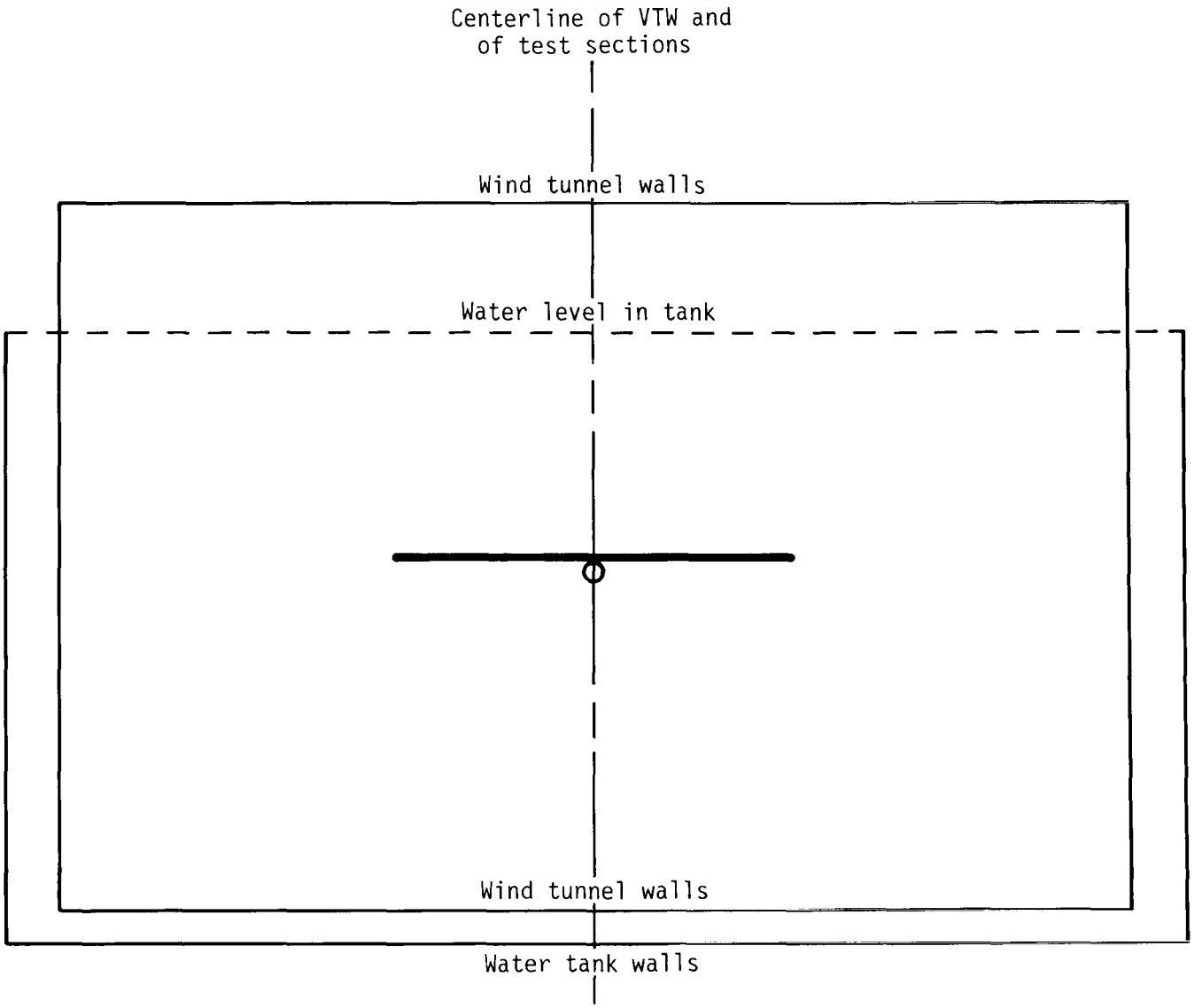


Figure A1. Comparative cross section views of VTW in wind tunnel and water tank test sections.

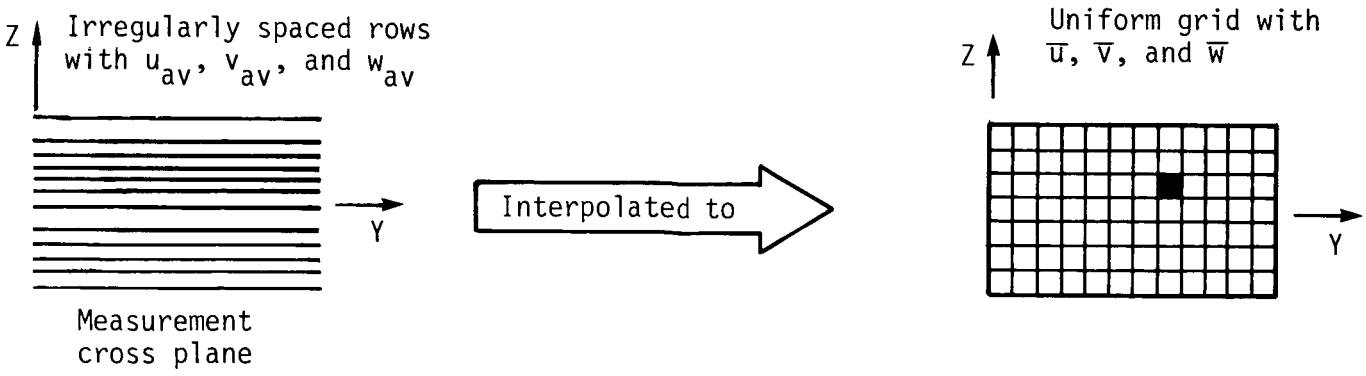


(a) Transformation of measured data to uniform grid.

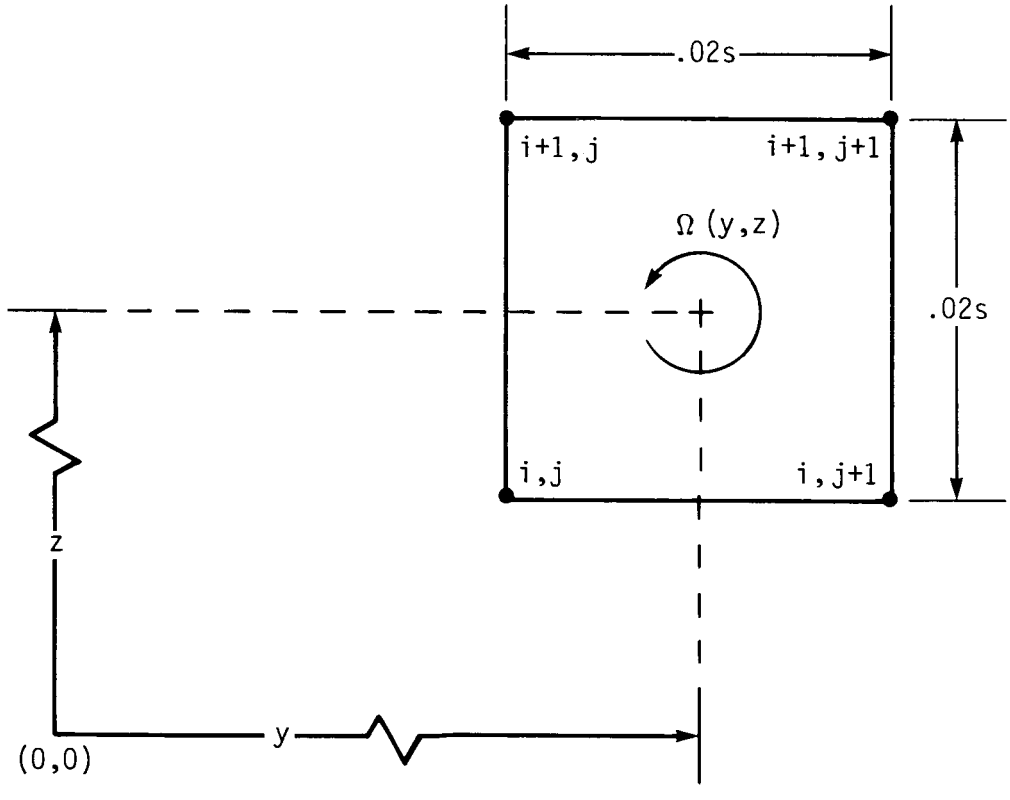


(b) Grid square element enlarged from (a) with $\bar{u}$, $\bar{v}$, and $\bar{w}$ at each corner.

Figure A2. Processing of wake velocity measurements to obtain distribution of streamwise vorticity.

# Appendix B

## Experimental Influences

The following sections describe in depth the results summarized within the section entitled Effects of Facilities and Measurement Techniques in the discussion.

### Aerodynamic Data

Force balance lift and drag data were obtained through an $\alpha$ range for the VTW1 configuration in both test facilities to assess any facility-produced effects on the initial wake roll up. The $C_D$ and $C_L$ data are plotted against $\alpha$ in figure B1(a) and against each other in figure B1(b). Notable in figure B1(a) are the higher lift curve slope obtained in the water tank and the near match of $\alpha$ at $C_L = 0.6$. Typically, at $C_L = 0.6$, $\alpha$ matched within 0.2° between facilities for each VTW configuration tested in both facilities. Since the water tank VTW was operating near the force balance design load at $C_L = 0.6$, the water tank aerodynamic data beyond this lift coefficient were taken at 67 percent of the normal free-stream velocity. The reduced lift curve slope in the water tank for $C_L > 0.6$ may have resulted from the growth, with reduced Reynolds number, of the laminar leading-edge separation bubble noted on the VTW model at a Reynolds number of $1 \times 10^6$ during the investigation reported in reference 39.

Given the rather coarse lift and drag resolutions of the force balances used in these tests, attempts at more closely correlating the data of figure B1(b) may seem unwarranted. However, the poor resolutions apply only for a single point measurement, not for the final filtered and averaged measurements. These sampling techniques damp out random balance "noise" and thereby enhance the measurement repeatability while resulting in a measurement which may still include a static offset, or bias. Thus, data trends will be smoothed without actually being more accurate. Indeed, the similar nature of the curves in figure B1(b) bears this out and points to possible $\alpha$ reference frame offsets or static force balance biases as the cause of the data disagreements.

As an example of simple flow angularity effects in the wind tunnel and $\alpha$ offset effects in the water tank, figure B1(c) presents the range of possible $C_D$ and $C_L$ data based on angle-of-attack inaccuracies between ±0.8° in both facilities. These curves were computed from the original VTW1 force balance measurements of normal and axial forces and then transformed to lift and drag data through the adjusted angle-of-attack range, $\alpha$ ±0.8°. In the wind tunnel, angle-of-attack inaccuracies could result from flow angularities at the VTW model location near the entrance cone to the test section. A vertical flow angularity of about 0.3° at this test section position was indicated in reference 33, in which positive lift at $\alpha = 0°$ was measured on a symmetric wing-body model similar in size to the VTW. Reference 39 reports on a test of the VTW1 configuration nearer the longitudinal midpoint of this wind tunnel test section in which zero lift was obtained at $\alpha = 0°$. This result conflicts with the positive $C_L$ obtained in this investigation, and this difference again indicates a vertical flow angularity at the front of the test section.

In the water tank, angle-of-attack inaccuracies were possible because $\alpha$ was set with reference to the angle between the VTW model carriage structure and the VTW vertical-blade mounting beams. This setup would have allowed an angle-of-attack offset to be carried through all water tank runs. As seen in figure B1(c), such angle-of-attack inaccuracies can easily allow correlation of the lift and drag data without regard to the possibility of balance bias. For example, figures B1(d) and B1(e) show $C'_L$ and $C'_D$ as computed from the original VTW1 data sets but based on a +0.5° flow angularity in the wind tunnel and a −0.5° reference frame offset in the water tank. With these corrections, the lift and drag data correlate well through $C'_L = 0.6$ and even produce the proper lower water tank $C'_D$ relative to the wind tunnel $C'_D$ (since centerbody forces were not measured in the water tank investigation). Figure B1(e) indicates minimal facility-induced effects on the VTW wake roll up since a given lift and drag are shown to correlate between the test facilities under plausible angle reference frame assumptions.

Even though $\alpha$ inaccuracies are indicated by other investigations and by the correlation of data from the two test facilities, direct flow angle measurements were not made in either facility. Because $C_D$ is very sensitive to $\alpha$ corrections (a 1° correction in angle of attack changes $C_D$ by 33 percent) and the exact $\alpha$ correction for each facility is unknown, the $C_D$ data cited in this report are uncorrected and are useful mainly in drag comparisons between VTW configurations in the same facility.

Figure B2 illustrates the effects of the wind tunnel survey rig on the aerodynamic data. With the survey rig at its closest location to the VTW (at $x/s = 1$ behind the right wing), the $\alpha$ required for a specified $C_L$ is reduced 0.6°, wing stall begins at 2° lower $\alpha$, and maximum $C_L$ is reduced by 0.04 when referenced to these measurements at $x/s = 6$ and 11. Pressure distribution measurements on the right wing with the survey rig at $x/s = 1$ and 11 verified the increased span load for a given $\alpha$ with the survey rig closer to

the model. Figure B2 also shows that for $C_L = 0.6$, $C_D$ was 21 percent lower for $x/s = 1$ than $x/s = 11$. This fact, along with the offset drag curves and a small negative rolling moment on the VTW, indicates that the proximity of the survey rig caused a vertical flow angularity across the right wing. The mean flow angularity difference across the entire wing between the near and far survey rig positions can be deduced from the difference in $C_D$ measurements at a given $C_L$. For $C_L = 0.6$ with the survey rig at $x/s = 11$ we have:

$$C_D = 0.030 = C_N \sin\alpha - C_A \cos\alpha \simeq 0.6\alpha - C_A$$

For $C_L = 0.6$ and the survey rig at $x/s = 1$ to induce a mean flow angularity ($\alpha_o$), we have:

$$C_D = 0.0237 = C_N \sin(\alpha + \alpha_o) - C_A \cos(\alpha + \alpha_o) \simeq 0.6(\alpha + \alpha_o) - C_A$$

Differencing these equations gives $\alpha_o = 0.6°$ and verifies the $\alpha$ offset shown in figure B2. Therefore, the survey rig at $x/s = 1$ was inducing a mean right wing upwash at the model of well above 0.6°. This upwash caused the offset drag curves and resulted in a lower maximum $C_L$ because of asymmetric stall.

The concern for the influence of the survey rig at its nearest position to the VTW was due to its possible effect on the wake development. This effect was negated for the most part by making the wake velocity measurements at the $\alpha$ required to give $C_L = 0.6$. This adjustment still left a residual swirl induced by the asymmetric loading of the VTW with the survey rig at $x/s = 1$. Aerodynamic and span load data, other than those of figure B2, were not influenced by the survey rig since these data were all obtained with the survey rig at $x/s = 11$.

### Span Load Data

Table V compares the force-balance-measured lift and pressure-integrated lift for VTW configurations tested in the wind tunnel. (Data for VTW7$S_2$ are not included since pressure distribution measurements were not taken.) Errors presented in columns 4 and 5 of this table are relative to the force-balance-determined lift coefficient. The fourth column gives the error in the wing integrated lift and the fifth column gives the error in the lift on the wing and centerbody combination.

Failure to incorporate the centerbody lift results in significant negative error. Extrapolation of centerbody lift from experimental measurements of cylindrical bodies alone (refs. 40 and 41) cannot account for the lift deficit shown. To account for the influence of the wing on the centerbody, a potential-flow panel method (ref. 42) was used to model the VTW wing and centerbody combination. Runs were made for VTW1 at $\alpha = 0°$ and 8° and the predicted centerbody lift contributions at both angles of attack were used to determine $dC_{L,\mathrm{CB}}/d\alpha$, which was then multiplied by $\alpha$ at $C_L \simeq 0.6$ for each VTW configuration to approximate $C_{L,\mathrm{CB}}$. The predicted $dC_{L,\mathrm{CB}}/d\alpha$ (about 0.002 per degree, based on the VTW wing reference area) is substantially above experimental body-alone measurements, and its inclusion in the comparison of $C_{L,p}$ with $C_L$ brings the agreement between these lift values well within the pressure instrumentation and force balance accuracy envelope.

The span load measurements were used to compute the value of $\bar{s}$, $\Gamma_o$, $\bar{b}/2$, and $\bar{d}$. Table VI(a) presents these parameters for the VTW span loads measured in the wind tunnel; table VI(b) presents the same quantities for elementary span loads for comparison. Since pressure distribution measurements were not made on the centerbody, the parameters of table VI(a) cannot include this contribution. As a result, the wing centerline circulation and dispersion radius were underestimated and the centroidal lift and vorticity positions for the wing and centerbody combination were overestimated.

Figure B3 illustrates the typical span load asymmetry found at the wing centerline in the wind tunnel tests. The twist distribution and span load are presented for VTW3; however, the asymmetry was noted for all measured span loads. This asymmetry was not due to asymmetric wing twist or wind tunnel swirl flow, because the VTW rolling-moment coefficient was negligible. Therefore, the asymmetry was likely due either to a localized flow asymmetry at the wing centerline or to defective pressure instrumentation. The data of table VI(a), combined with the wake velocity and trailing-wing data, revealed that the span load asymmetry was caused by a tunnel flow asymmetry. This result will be discussed along with the wake velocity data.

### Trailing-Wing Rolling-Moment Data

Historically, the trailing-wing rolling-moment survey technique has been utilized as a simple method to quantify local regions of angular momentum within aircraft-generated wakes. These measurements have commonly been applied to indicate the roll upset hazard presented to a small aircraft in the vortex wake of a large aircraft. (See refs. 16 to 27.) Typically, experimental tests have utilized trail-to-lead aircraft (or model) span ratios from 17 percent to 23 percent; however, for this investigation the ratio of the trailing-wing span to the VTW span was

only about 13 percent. This relatively smaller trailing wing can be immersed more completely within the viscous vortex core region of the wake, so that the rolling-moment measurements are more sensitive to vortex core changes. Along with the increased sensitivity come a higher variation in rolling moment with trailing-wing position relative to the vortex core and a lowered capability to measure the roll hazard to larger encountering aircraft. Thus the assessment of test facility effects on the unsteady trajectory of the vortices is imperative to determine the correlation and importance of peak and long-time-average rolling-moment data.

Downstream distance effects on peak and average $C_{l,\mathrm{TW}}$ data measured in the water tank are illustrated in figure B4. Peak data $C_{l,\mathrm{PK}}$ were derived with the trailing wing traversing vertically, as shown in figures B4(a), (c), and (e). The oscillations apparent at $x/s = 70$ in figure B4(e) were a result of the vortex meandering about the traversing wing, not multiple vortices, since these data are for the untwisted wing (VTW1), which developed a single vortex per semispan. Development of vortex meander with downstream distance is more apparent in figures B4(b), (d), and (f), in which $C_{l,\mathrm{AV}}$ data were taken by fixing the trailing-wing $y, z$ position to that at which $C_{l,\mathrm{PK}}$ was obtained and averaging $C_{l,\mathrm{TW}}$ over an 18-sec period. At $x/s = 11$, the nearly constant $C_{l,\mathrm{TW}}$ signal at the center of the vortex indicates negligible meander levels. VTW configurations with wing twist exhibited slightly higher $C_{l,\mathrm{TW}}$ fluctuations at $x/s = 11$, but $C_{l,\mathrm{AV}}$ was still at 70 to 95 percent of $C_{l,\mathrm{PK}}$. As the vortex wake progressed downstream, meander became much more significant; $C_{l,\mathrm{AV}}$ was typically reduced to 40 to 60 percent of $C_{l,\mathrm{PK}}$ at $x/s = 40$ and 20 to 40 percent of $C_{l,\mathrm{PK}}$ at $x/s = 70$. By $x/s = 70$, $C_{l,\mathrm{TW}}$ was cyclic with a wavelength of about $14s$. This pattern correlates with the Crow instability, the predominant long-wavelength disturbance of vortex wakes in free air under neutrally stable atmospheric conditions. (See refs. 43 and 44.)

As shown in figure B4, $C_{l,\mathrm{TW}}$ fluctuations over the 18-sec averaging period used to obtain $C_{l,\mathrm{AV}}$ (equivalent to three periods of the Crow instability) were dominated by the long-wavelength Crow instability rather than the smaller scale turbulence produced at the wing. Vortex meander amplitude can be approximated from the length of the trailing-wing vertical traverse between $C_{l,\mathrm{TW}}$ peaks. Measurement of this traverse length yields an amplitude of $0.1s$ to $0.2s$ at $x/s = 70$. Because meander amplitude was affected by the presence of the trailing-wing model, a conservative estimate would place the meander amplitude at about a trailing-wing semispan, or $0.13s$, in order to cause $C_{l,\mathrm{TW}}$ sign reversals between $C_{l,\mathrm{TW}}$ peaks. Thus, water tank $C_{l,\mathrm{TW}}$ data such as those shown in figure B4 identify a nearly negligible level of vortex meander at $x/s = 11$ which amplifies to a substantial (and, as will be discussed, unexpectedly high) level at $x/s = 40$ and 70.

Vortex meander was also of concern in the wind tunnel for both rolling-moment and wake velocity surveys. Two previous vortex wake investigations noticed significant meander near $x/s = 6$ in this wind tunnel. In reference 45, an unsteady 10-sec trailing-wing rolling-moment average was noted in the wake of a wing-tip blowing model lifting at about $C_L = 0.6$, and in reference 14, vortex meander was visually estimated to be about 0.3 m in amplitude downstream of a 1.6-m-semispan multisegmented flapped wing, also lifting at about $C_L = 0.6$. Indeed, the hot-film measurements taken downstream of the VTW during this investigation indicate a meander amplitude ranging from a low of about $0.2s$ at $x/s = 1$ up to about $0.2s$ at $x/s = 11$. Because of the 0.1-Hz low-pass filtering applied to the $C_{l,\mathrm{TW}}$ data, the predominant meander wavelengths could not be determined; however, the 5-sec sampling period (about 12 periods of the Crow instability) assures that any unsteadiness in the $C_{l,\mathrm{AV}}$ measurement must be due to longer wavelength disturbances originating within the wind tunnel circuit.

Clearly, a valid comparison cannot be made of wind tunnel and water tank $C_{l,\mathrm{AV}}$ data at $x/s = 11$ (the only common downstream measurement location) since the vortex meander level was much greater in the wind tunnel. As a result of the disproportionate meander, wind tunnel $C_{l,\mathrm{AV}}$ data were typically much lower than those measured in the water tank. Also $C_{l,\mathrm{AV}}$ measured within each facility cannot be used as a relative indicator of the vortex upset because the averaging period for these data (several cycles of the Crow instability) was far beyond reasonable response times for encountering aircraft. Scaling the water tank and wind tunnel averaging periods such that the VTW represents a full-scale transport airplane yields times of about 18 and 64 sec, respectively, as the characteristic response time for a general aviation aircraft intercepting a wide-body transport aircraft wake. A comparison of these averaging periods with the typical 1- to 3-sec period of a vortex encounter shows that the experimental averaging periods are far from characteristic aircraft roll response times. Specifying a full-scale response time of 0.5 sec correlates with an experimental downstream wake averaging length of about 1.3 VTW semispans. Incorporation of the 0.1-Hz low-pass filter in the wind tunnel data system rendered $C_{l,\mathrm{TW}}$ variations undetectable for signal fluctuations at wave-

lengths less than about 100 VTW semispans. In comparison, the water tank data system limitation of 20 Hz corresponded to wavelengths of about 0.13 VTW semispans. Thus the water tank $C_{l,\mathrm{PK}}$ data contained rolling-moment fluctuations with a period equivalent to about 0.05 sec at full scale.

It should be noted that the amplification of the Crow instability found in the water tank was much greater than that called for in reference 43. However, this prediction assumes an unbounded wake and no direct relation between atmospheric turbulence and the amplification rate. References 3, 46, and 47 all demonstrate that Crow's mutual induction instability should grow more rapidly with increasing turbulence level, and reference 48 demonstrates that the amplification should increase as the ground plane is approached. Experimental verification of these analyses is contained in reference 49. Results of these studies and the VTW investigation suggest that model studies cannot be expected to properly reproduce the long wavelength instabilities found in free air without very small scale models (relative to the test facility) and without accurately scaling the test section turbulence to the desired free-air condition. Unless these criteria are met, average trailing-wing rolling moments are unreliable because they represent a long time average taken over a spatial region of the model vortex flow field which may not match that of the full-scale aircraft.

All these considerations limit the applicability of the $C_{l,\mathrm{AV}}$ data. Instead of quantifying the roll hazard posed to a following aircraft, these data when referenced against $C_{l,\mathrm{PK}}$ data are a better indicator of the vortex meander level. Therefore, $C_{l,\mathrm{PK}}$ data (where available) will be emphasized over $C_{l,\mathrm{AV}}$ data in evaluating the attainment of downstream vortex alleviation by a VTW configuration.

Another concern regarding the trailing-wing rolling-moment surveys has been the possibility of the trailing wing stalling while embedded in the high tangential velocities of the vortex core. In a previous investigation, the possibility of stall was lessened when the trailing wing was centered in the vortex by counter twisting the right and left wing panels of the trailing wing to oppose the vortex rotational flow and reduce the net angle of attack along the wing. (See ref. 8.) Trailing-wing stall was not a problem during the VTW investigation, as evidenced by figure B4(a), in which the trailing-wing rolling moment increases and decreases smoothly as the trailing model ascends directly through the center of the most intense vortex measured. (VTW1 at $x/s = 11$ had the highest measured $C_{l,\mathrm{PK}}$.) Figure B4(b) shows the trailing wing constantly centered in the vortex (with negligible meander), and the resulting flat $C_{l,\mathrm{TW}}$ time history does not resemble the unsteady signal that would be expected with a highly stalled wing. Simple rolling-moment calculations indicate that a stalled trailing wing would have a $C_{l,\mathrm{PK}}$ of at least 0.13, which is 30 percent higher than any $C_{l,\mathrm{PK}}$ obtained in these tests. This calculation is based on an elliptical load distribution on each semispan with a minimum and maximum $c_\ell$ of $\pm 0.65$ (at the midsemispan) chosen conservatively to reflect the $1.7 \times 10^5$ chord Reynolds number of the trailing wing (ref. 50). Many of the previous investigations were conducted at transport aircraft landing approach lift conditions ($C_L \geq 1.2$). The much lower $C_L$ of 0.6 used in the VTW investigation resulted in reduced tangential velocity fields and made stall much less likely.

By 70 semispans downstream, the wakes of three VTW configurations (VTW4, VTW7$S_0$, and VTW7$S_2$) had descended to nearly a semispan above the water tank floor. Below this height, wake decay can be substantially affected by the ground plane; however, the trailing-wing measurements indicated that this effect was negligible through $x/s = 70$. The $C_{l,\mathrm{PK}}$ data for VTW4 (fig. 14) remained essentially constant with downstream distance rather than showing any enhanced decay, as would be caused by ground effect between 40 and 70 semispans downstream. It is possible that the outer perimeter of the wake oval had been influenced by the ground plane, but the effects had not yet propagated into the relatively small vortex core region surveyed by the trailing-wing model.

### Wake Velocity Data

This section addresses the effects of the wind tunnel and measurement techniques on the accuracy of the wake velocity data. Accuracy of the data local to vortex cores will be considered first, along with problems with the hot-film probe and vortex meander and their interrelation with the velocity data averaging technique. Next, similar accuracy evaluations will be made for the low-velocity gradient regions well outside the vortex cores. Finally, overall accuracy at the three downstream measurement planes will be examined by referencing wake-integrated parameters to the corresponding parameters derived from wing span load measurements.

Typical hot-film probe traverses through the wakes of two VTW configurations in the wind tunnel at $x/s = 1$ and 11 are shown in figures B5 through B7. These figures show the $w$ and $u$ velocity components as sampled at 50 points per second and as 100-point averages, and also present the standard deviation corresponding to the averaged signal. Each traverse was made horizontally and crossed near the mean center position of a vortex of major strength.

Identical scales are maintained for each of the $w$ component figures and for each of the $u$ component figures to facilitate comparisons. Figures B5 and B6 contrast the dominant vortices of VTW7$S_0$ and VTW7$S_3$ at $x/s = 1$. The turbulent spoiler wake of VTW7$S_0$ is also crossed near its center in figure B5. The effects of vortex meander and downstream distance on the velocity data (in this case presented for the wake of VTW7$S_0$) are apparent in figure B7.

Vortex cores and the turbulent spoiler wake presented an unsteady high-velocity gradient flow to the hot-film probe, and as a result the measured velocity data were contaminated by probe oscillation at about 15 Hz and by flow field meander with its dominant frequencies well below 5 Hz. The probe oscillation was noted visually throughout the wind tunnel test; its frequency was determined by power spectral analysis of a sample of hot-film voltages digitized at 8000 points per second (ref. 38). Maximum probe tip velocity was estimated to be $\pm 0.1 U_\infty$ based on a conservative $0.08s$ peak-to-peak probe oscillation amplitude in high-velocity gradients. For the hot-film probe traversing at $.01s$/sec (1.3 cm/sec), the peak probe oscillation velocities would then be expected at intervals of approximately $0.0003s$. These probe oscillation velocities would thus be separated from the lower-frequency and much higher amplitude velocity excursions produced by both flow field meander near vortex cores and the spoiler wake. Meander caused velocity fluctuations approaching $\pm 0.5 U_\infty$ at $x/s = 1$, where a vortex with a vertical velocity differential of approximately $U_\infty$ over a core diameter of about $0.03s$ could sweep through a meander amplitude of about $0.02s$. As stated previously, observation of the wake velocity data at vortex intercepts determined a meander amplitude that rose from about $0.02s$ at $x/s = 1$ to approximately $0.2s$ at $x/s = 11$. This meander amplification is detectable in figures B6 to B8 by a comparison of the lateral spreads of the large velocity fluctuations around vortex cores between $x/s = 1$ and $x/s = 11$.

Figures B5 through B7 are examples of the hot-film measured velocities with the interwoven effects of probe oscillations, vortex meander, vortex decay, and the 100-point averaging technique. Although at first glance the averaged velocities might give the impression that they represent a good "smoothed" determination of the velocity field, further analysis shows that the averaging technique and vortex meander significantly affected the measured velocities, vorticity, and circulation local to a vortex core. Figure B8 illustrates a simulated hot-film averaged measurement of an axisymmetric vortex with a Gaussian vorticity distribution which resulted in a core radius of $0.02s$, a maximum tangential velocity of $0.5 U_\infty$, and a large-radius circulation of $0.088 U_\infty s$. These values are similar to those for the vortices of several VTW configurations. Meander was modeled as a pure lateral translation of the flow field with respect to the hot-film probe, probe oscillation was not modeled, and $w_{av}$ was computed as a running average over the averaging length and meander amplitude. Neglecting probe oscillation and the vertical components of meander certainly causes this simulation to understate the problem, but as shown in figure B8, increasing meander forces the averaged velocity, vorticity, and circulation profiles to mimic rapid vortex decay.

Flow field meander has long plagued vortex wake investigations and has instigated the development of several measurement systems, such as rapid-sweeping hot wires (ref. 51) and rapid-scanning laser velocimeters (refs. 52 and 53), which are capable of relatively high frequency response measurements over a very limited region of the flow. However, to the knowledge of the authors, nonintrusive techniques are not yet available for near-instantaneous mapping of an entire velocity cross plane. As a result, the alternative low-speed traverse measurement technique utilized in this investigation suffers from significant error local to vortex cores. The best of the core measurements at $x/s = 1$ with the smallest meander amplitude ($0.02s$) can be expected to show a 20-percent loss in the peak core velocity, a 40-percent loss in the peak vorticity, and a small local circulation overshoot. The circulation overshoots are damped to the large-radius circulation via integration of the very small negative predicted vorticity at large radius. Both local circulation overshoots and peak vorticity offsets from vortex centerlines predicted by the simulation are exhibited in VTW wakes by $x/s = 11$. These correlations confirm that the implied rapid vortex decay by this downstream distance was a measurement fallacy. Other filtering, sampling, and averaging techniques were investigated, but hot-film probe oscillations and flow field meander overwhelmed attempts to obtain highly accurate and detailed vortex core flows at the downstream distances surveyed.

In contrast to the high-velocity gradient regions, outside of vortex cores and turbulent spoiler wakes, the effects of hot-film probe oscillations, flow field meander, and the 100-point averaging technique were negligible. Here the minimal probe oscillation was essentially filtered out by the averaging technique, and flow field meander forced spatial averaging over an essentially linear gradient field. As a result, mean values representative of the actual velocity at the center of the averaging volume were produced. These points are evident in the wake velocity traces of figures B5 through B7 and in the simulated wake

measurements shown in figure B8. At one semispan downstream, figure B8 indicates that the effects of the averaging technique and flow field meander are negligible beyond $0.03s$ away from vortex centers. But by 11 semispans downstream, the measurements are contaminated with these effects at vortex radii of up to $0.2s$.

Overall flow field measurement accuracy was assessed by comparing the wake-integrated values of $\Gamma$ and $\bar{y}$ with the corresponding two-dimensional inviscid invariants $\Gamma_o$ and $\bar{b}/2$ derived from the span load measurements. Because of viscous decay and the three-dimensional nature of the wake roll up, the wake-integrated parameters $\Gamma$ and $\bar{y}$ are not necessarily invariant. However, these effects are small over the wind-tunnel-tested $x/s$ range and would certainly lower $\Gamma$ values as vorticity was diffused and cancelled across the wake centerline, and would also cause $\bar{y}$ to vary inversely with $\Gamma$ to conserve the initial impulse per unit fluid volume, $\bar{y}\Gamma$. However, the comparison of wake-integrated and span-load-measured circulation and vorticity centroid (fig. B9) shows a contrary trend, with $\Gamma$ increasing well beyond $\Gamma_o$ and $\bar{y}$ remaining at about 0.85 to 0.95 $\bar{b}/2$ as $x/s$ increases. Plotted ratios of $\Gamma/\Gamma_o$ were adjusted to account for small $C_L$ and $U_\infty$ differences between wake velocity runs and span load measurement runs. These differences had no effect on the $\bar{y}/(\bar{b}/2)$ ratio since each parameter is dependent on the ratio of two similarly varying quantities: $\bar{y}\Gamma$ versus $\Gamma$ for $\bar{y}$, and $C_{L,p}$ versus $c_{\ell,o}$ for $\bar{b}/2$. Both wake-measured parameters ($\Gamma$ and $\bar{y}$) inherently included the effect of the centerbody, whereas the wing-span-load-measured $\Gamma_o$ and $\bar{b}/2$ neglected centerbody effects.

The $\Gamma$ and $\bar{y}$ measurements, along with the previously mentioned wing centerline span load asymmetry, were indications of a minor wind tunnel flow asymmetry, possibly combined with a small model installation asymmetry. Recall that wind tunnel swirl was judged to be negligible since force balance measurements of VTW rolling moment were insignificant. Trailing-wing rolling-moment data and vorticity contours provided the information esssential to deduce the mechanism for the unexpected wake circulation and vorticity centroid results.

Figure B10 shows the differences in vortex core positions as determined by wake velocity measurements ($y_\Omega$) and trailing-wing measurements ($y_{\mathrm{TW}}$). All wake velocity surveys were made behind the right wing; however, for three of the four VTW configurations with wake velocity measurements, trailing-wing measurements were obtained behind the left wing. The core positions obtained with each technique agreed only for VTW7S$_3$, the configuration on which both trailing-wing and wake velocity data were taken behind the right wing. The other three configurations show a significant and enlarging difference in measured core positions with downstream distance in figure B10. The increasing difference indicates a right-to-left flow angularity which forces the right wing vortex inboard (as determined by $y_\Omega$) and the left wing vortex outboard (as determined by $y_{\mathrm{TW}}$). The data trends shown in figure B10 indicate a mean angularity of 0.4° along the test section length. Span load asymmetry at wing centerline thus resulted from centerbody blockage of lower wing surface flow just left of centerline.

The net effect of the lateral flow angularity on the wake velocity measurements is believed to be more complicated. Lateral flow provided several mechanisms for the circulation and vorticity centroid trends evidenced in figure B9. Figure B11(a) illustrates a possible wake development in which the first measurement cross plane essentially encompasses only the VTW vorticity field. The lateral flow now induces "lift" (side force) on the vertical VTW support blade. This lift then convects additional vorticity across the wake centerline—and eventually the wind tunnel centerline—with increasing downstream distance, and the measured $\Gamma$ is thus forced above that expected from the wing-alone $\Gamma_o$ value. The negative vorticity from the bottom of the blade was not measured since it was shed below the lower bounds of the velocity survey region. Additionally, the centerbody, even though carrying only 1 to 3 percent of the total model lift, may have shed significant vorticity because of its long slender profile. This too would increase $\Gamma$ with downstream distance as the centerbody wake was convected across the wind tunnel centerline into the downstream measurement cross planes. Measurements of $\bar{y}$ would be expected to remain below the $\bar{b}/2$ dictated by span load data because of the addition of vorticity at small $y$ displacements and because the $\bar{y}$ was computed with respect to the wind tunnel centerline rather than the continually leftward shifting wake centerline. This type of scenario is borne out by several downstream measured vorticity cross planes, such as that of VTW7S$_3$ shown in figure B11(b) recontoured at lower $\Omega$ levels. By $x/s = 6$, the support blade vorticity (and possibly that of the centerbody) was substantially wrapped into the right-wing wake, with its residual vorticity at such low levels that it was not typically visible at the vorticity contour levels chosen for the VTW wakes in the remainder of this report.

In view of the inherent accuracy limitations of the wake velocity data near vortex cores and the possible contamination of the wake survey region beyond $x/s = 1$ with VTW support blade and/or centerbody vorticity, the wake velocity data can be

treated as quantitatively accurate only at $x/s = 1$. Even here, 10 to 20 percent accuracy is the limit, as shown in figures B8 and B9. At the two further downstream measurement locations, $x/s = 6$ and 11, these data can be viewed as only qualitatively correct -- useful mainly in judging whether complete merger of multiple vortices within the wake had occurred. For these reasons, and to facilitate comparisons, the vorticity data derived from the wake velocity surveys are presented at identical contour levels for all VTW configurations and downstream survey locations. Normalized vorticity contour levels ($\Omega s/U_\infty = \pm e^n/2$, $n = 0, 1, 2, \ldots$) were chosen to reflect the qualitative nature of the data and avoid the difficulties of densely packed contours in high-vorticity gradient regions (as seen, for example, in fig. B11(b)). Averaged vortex velocities are presented only for $x/s = 1$, as are comparisons of predicted and measured wake development.

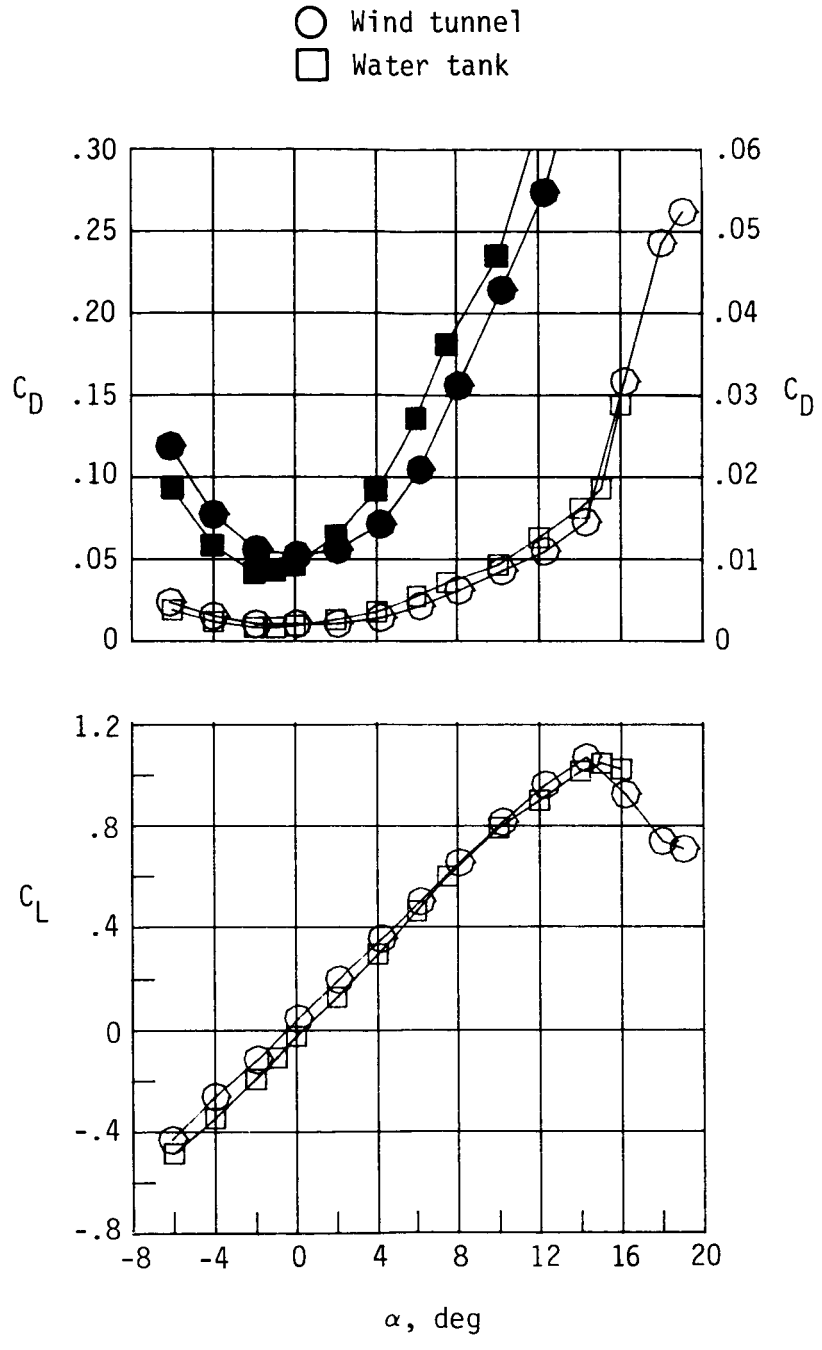


(a) Force balance measurements referenced to geometric $\alpha$. Open symbols are plotted on the left-hand $C_D$ scale and solid symbols are plotted on the expanded $C_D$ scale at the right.

Figure B1. Wind tunnel and water tank aerodynamic data for VTW1.

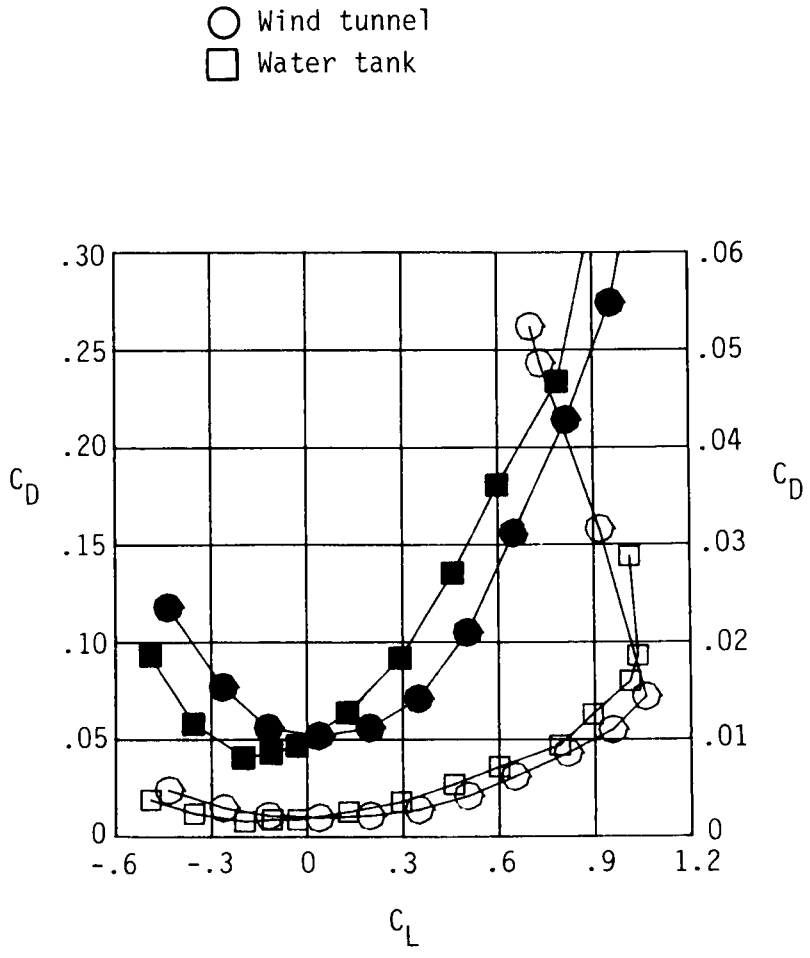


(b) Force balance measurements of $C_D$ versus $C_L$. Open symbols are plotted on the left-hand $C_D$ scale and solid symbols are plotted on the expanded $C_D$ scale at the right.

Figure B1. Continued.

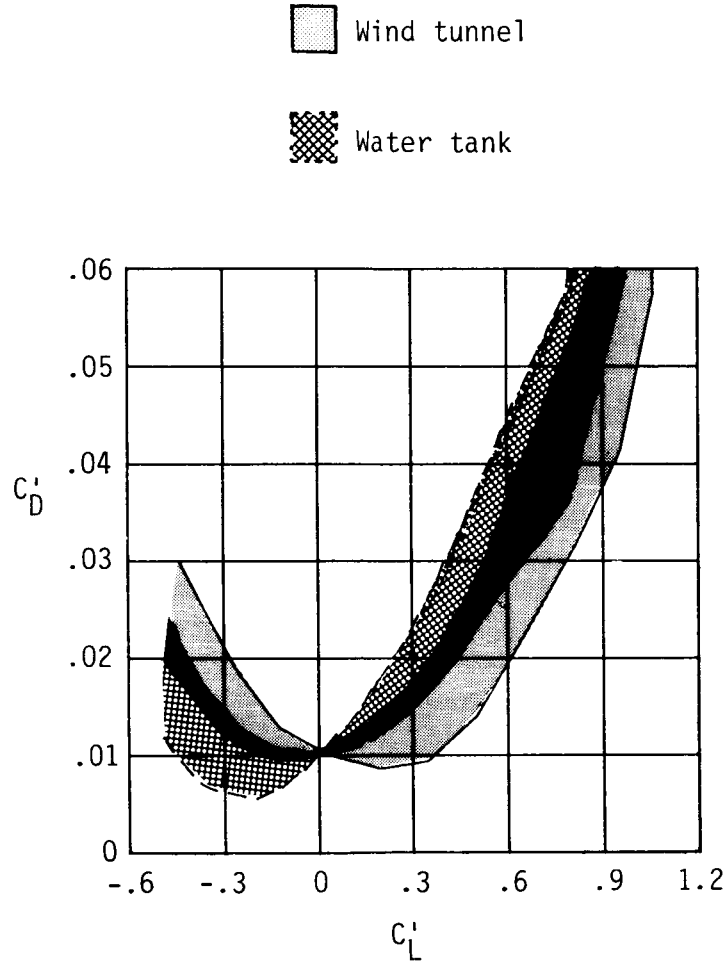


(c) Possible ranges of $C_L$ and $C_D$ data for VTW1 based on angle-of-attack inaccuracies between $\pm 0.8°$.

Figure B1. Continued.

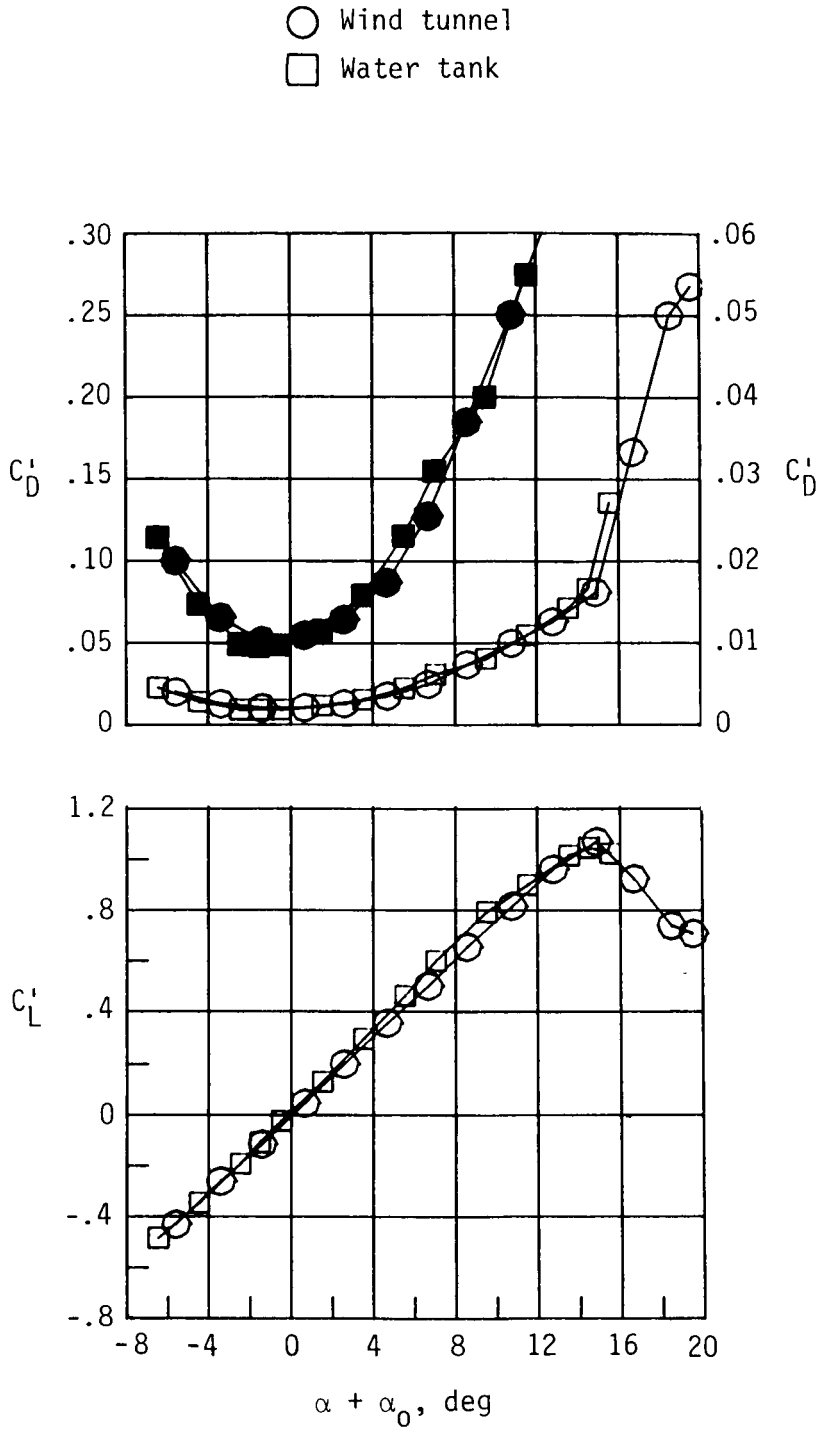


(d) Recomputed lift and drag coefficients based on $\alpha_o = +0.5°$ in the wind tunnel and $\alpha_o = -0.5°$ in the water tank. Open symbols are plotted on the left-hand $C_D$ scale and solid symbols are plotted on the expanded $C_D$ scale at the right.

Figure B1. Continued.

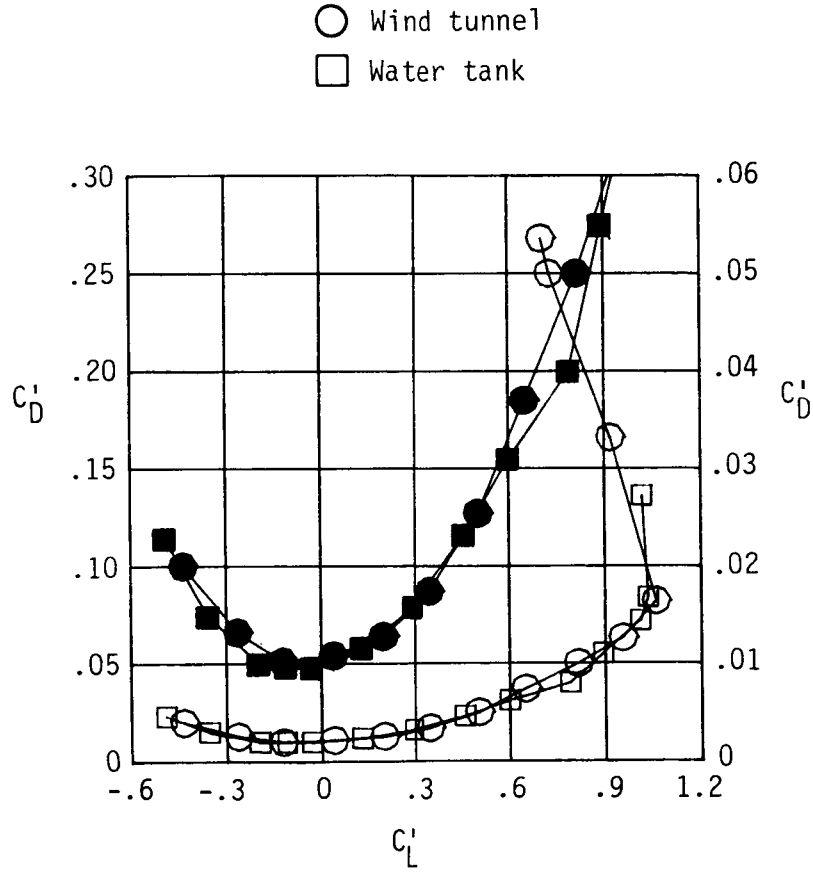


(e) $C'_D$ versus $C'_L$ based on $\alpha_o = +0.5°$ in the wind tunnel and $\alpha_o = -0.5°$ in the water tank. Open symbols are plotted on the left-hand $C_D$ scale and solid symbols are plotted on the expanded $C_D$ scale at the right.

Figure B1. Concluded.

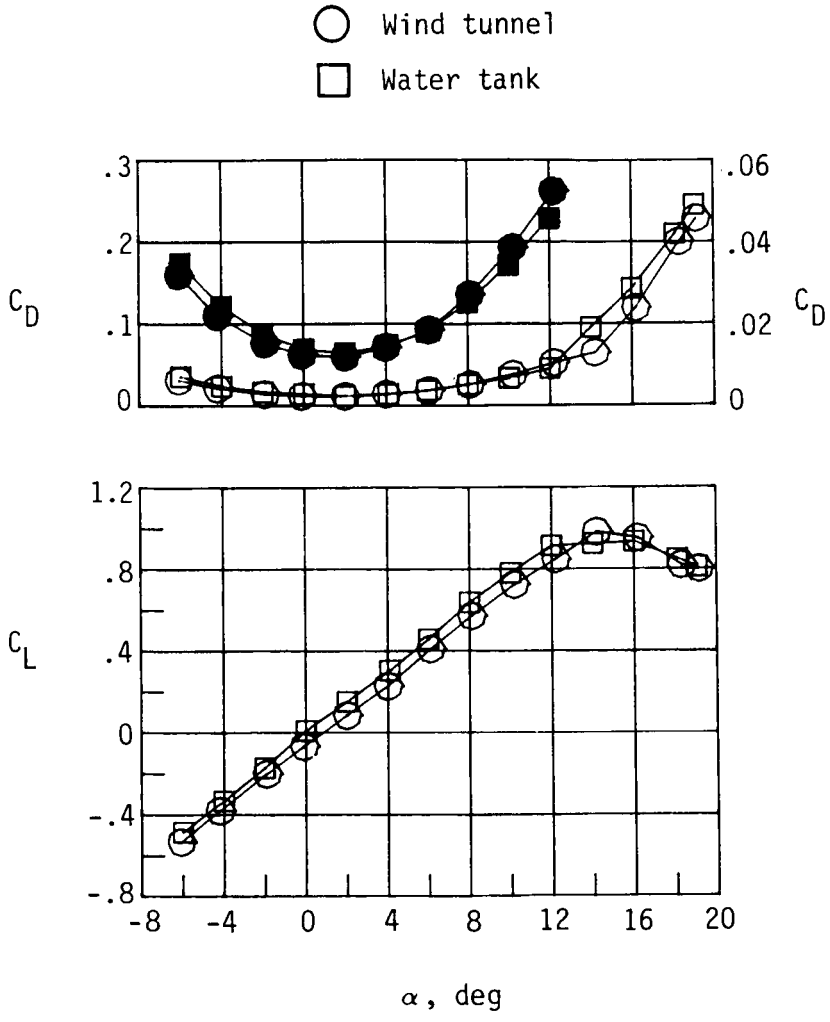


Figure B2. Effect of wind tunnel survey rig at $x/s = 1$ and 11 on aerodynamic data for VTW7. Open symbols are plotted on the left-hand $C_D$ scale and solid symbols are plotted on the expanded $C_D$ scale at the right.

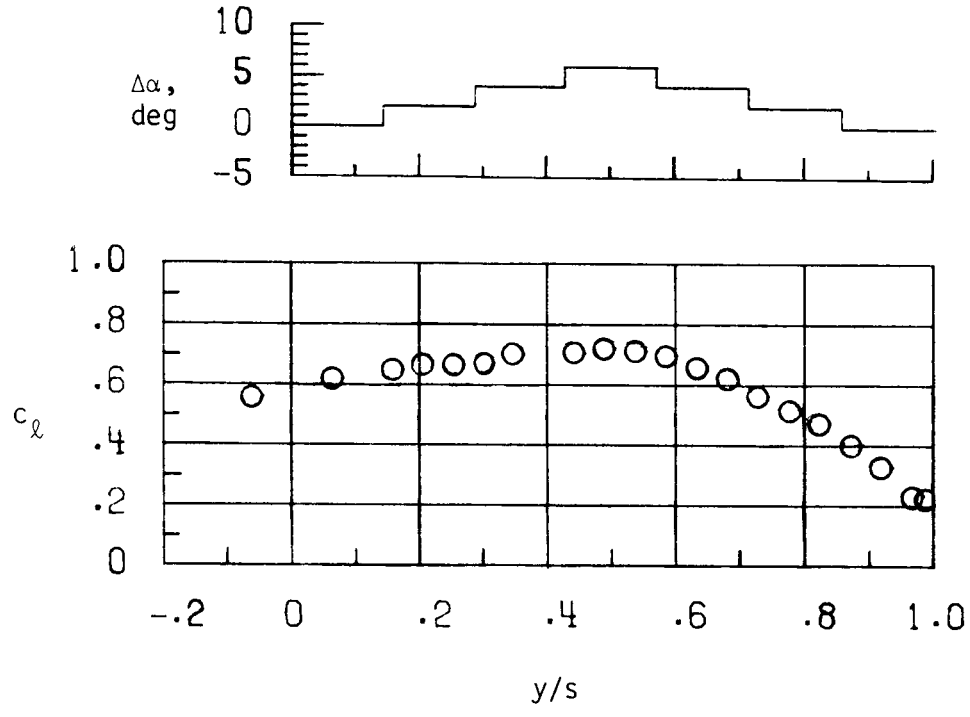


Figure B3. Typical span load data illustrating asymmetry of span load across wing centerline.

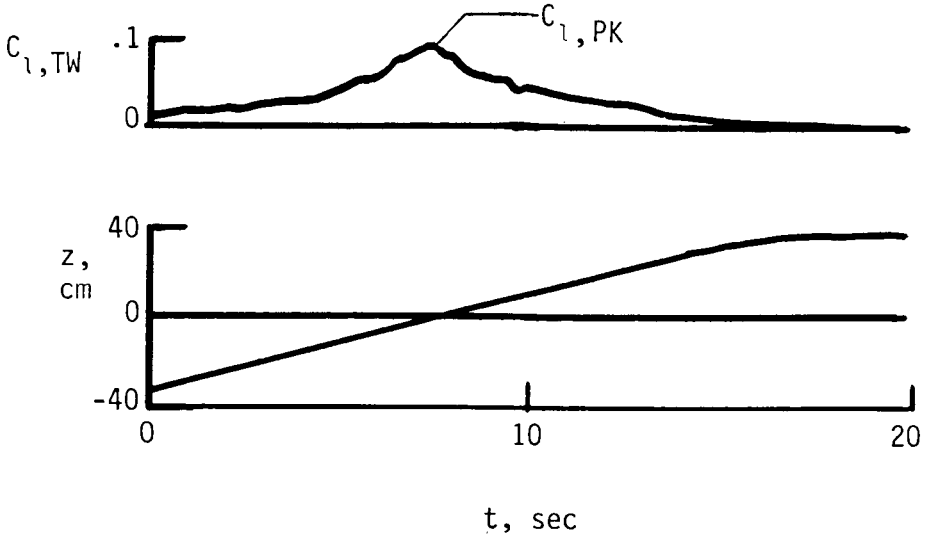


(a) $x/s = 11$, trailing wing traversing vertically.

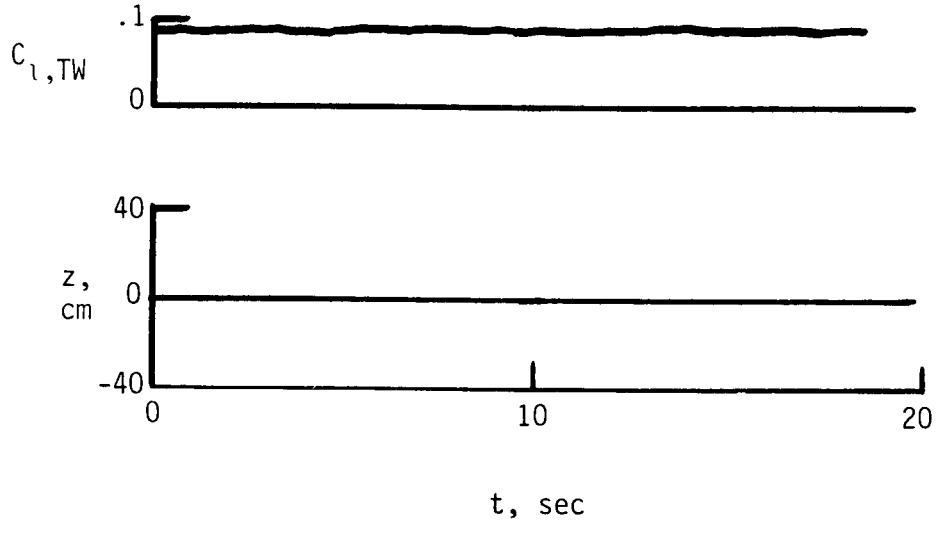


(b) $x/s = 11$, trailing wing at constant $z$.

Figure B4. Time histories of $C_{l,\mathrm{TW}}$ taken behind VTW1 in water tank at $x/s = 11$, 40, and 70.

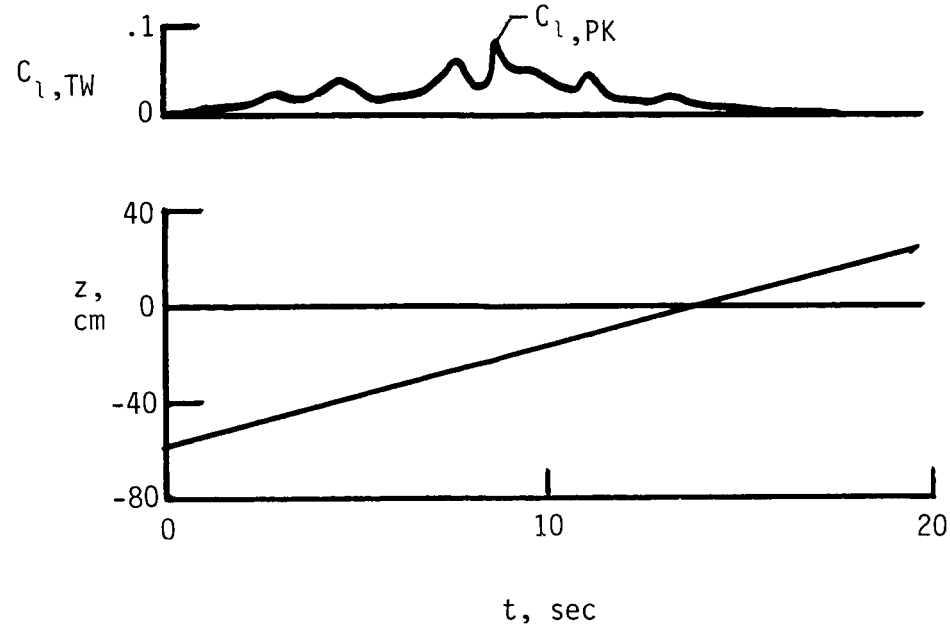


(c) $x/s = 40$, trailing wing traversing vertically.

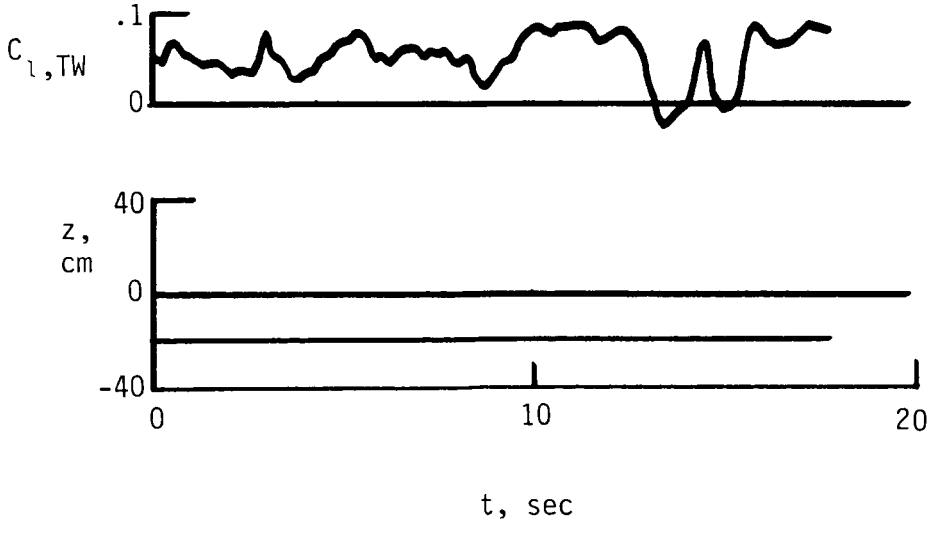


(d) $x/s = 40$, trailing wing at constant $z$.

Figure B4. Continued.

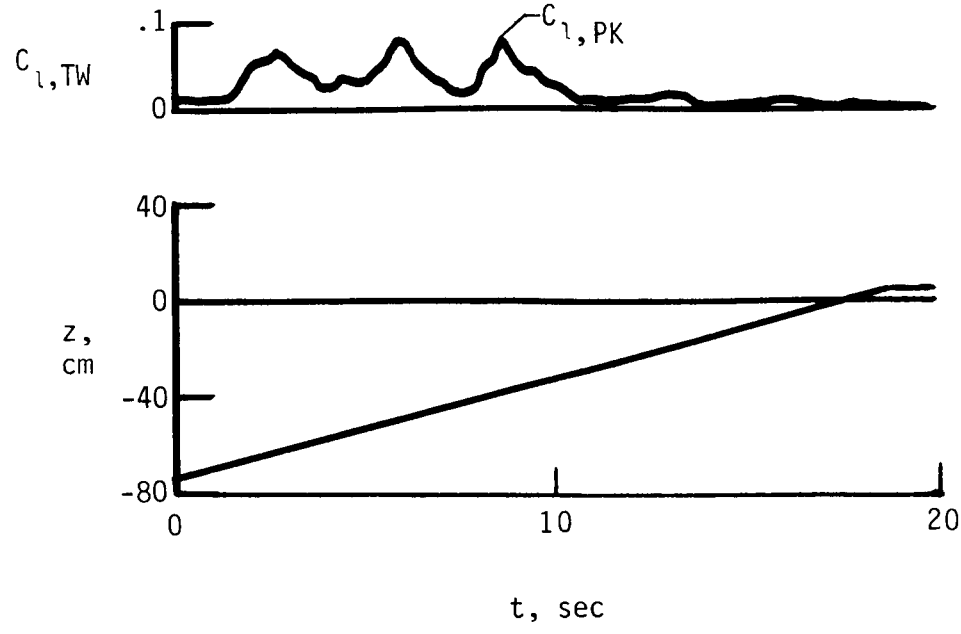


(e) $x/s = 70$, trailing wing traversing vertically.

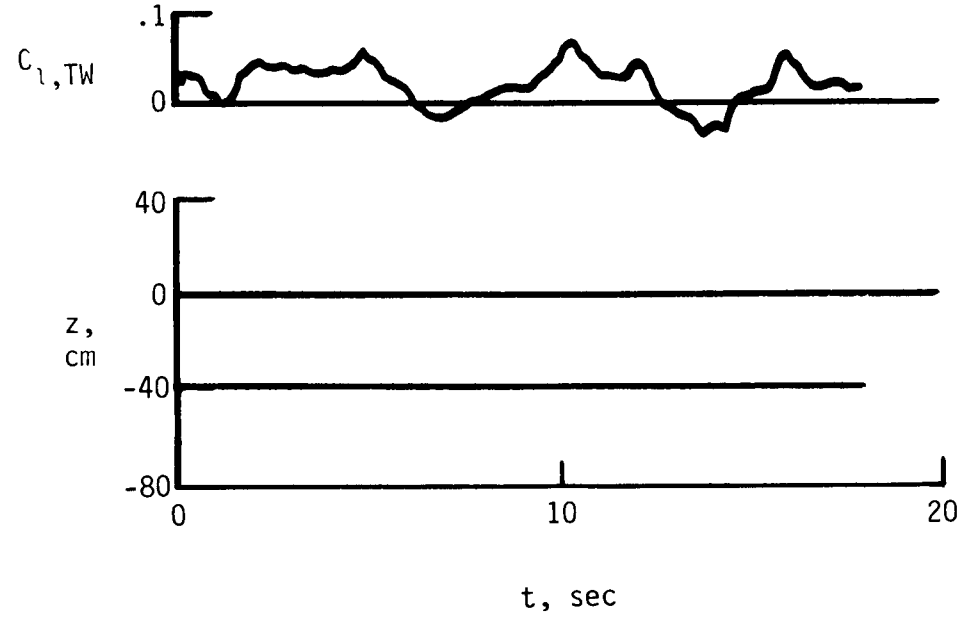


(f) $x/s = 70$, trailing wing at constant $z$.

Figure B4. Concluded.

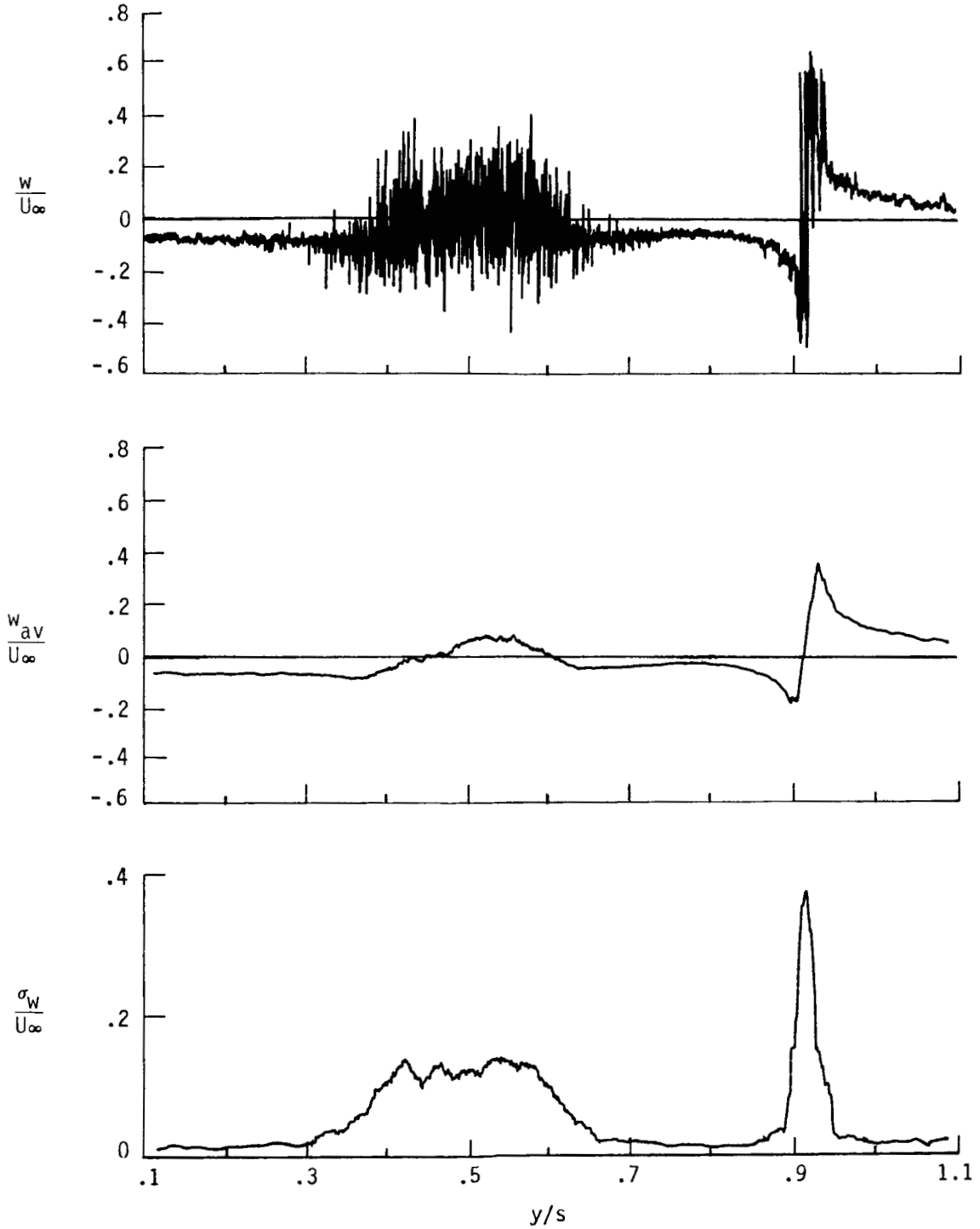


(a) Vertical velocity data.

Figure B5. Typical vertical and axial velocity profiles at $x/s = 1$ taken in the wake of VTW7S$_0$ at $z/s = 0.089$ through a high-turbulence region and a vortex core.

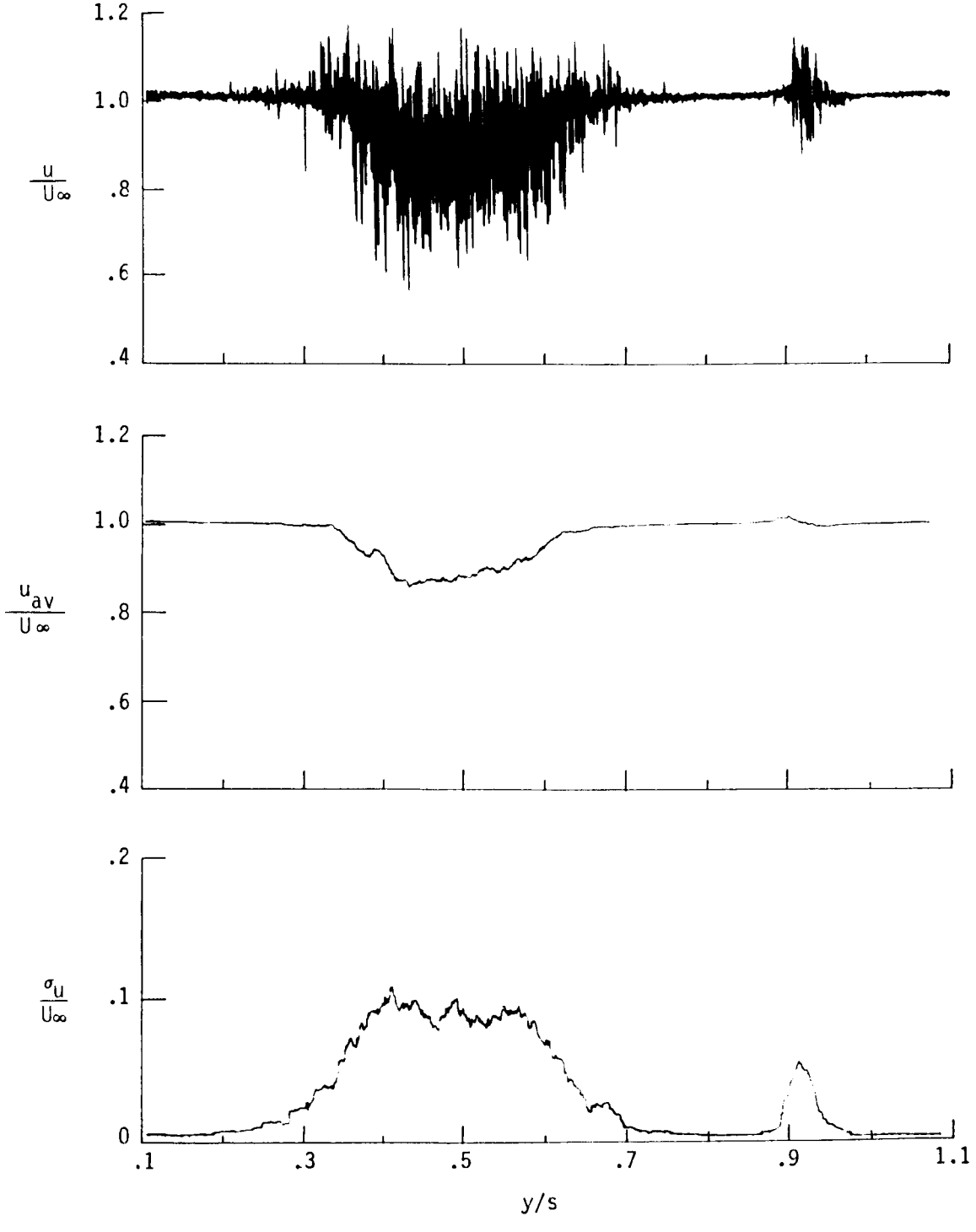


(b) Axial velocity data.

Figure B5. Concluded.

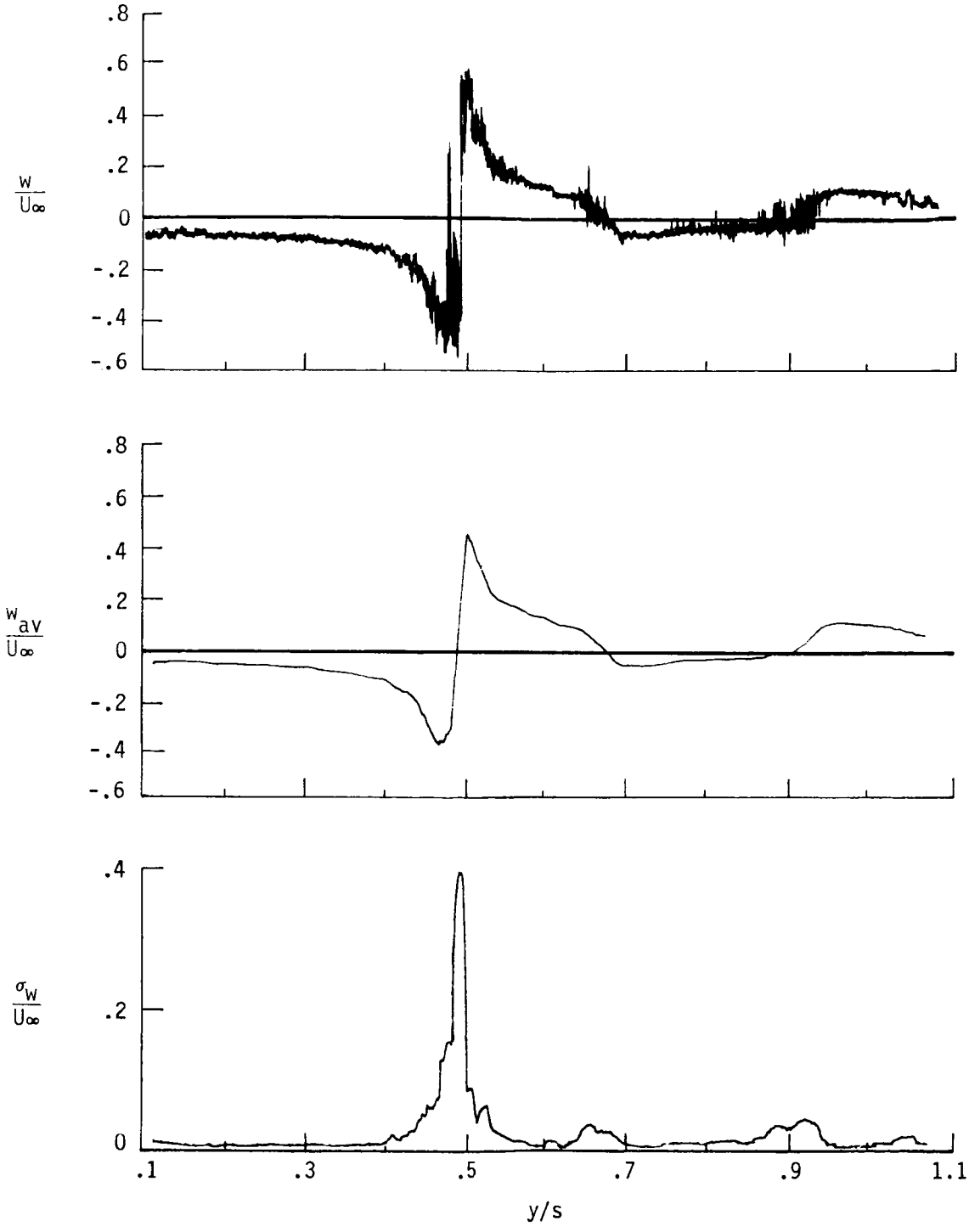


(a) Vertical velocity data.

Figure B6. Typical vertical and axial velocity profiles at $x/s = 1$ taken at $z/s = 0.024$ through a vortex core for a VTW configuration without spoilers, splines, or drag plates ($VTW7S_3$).

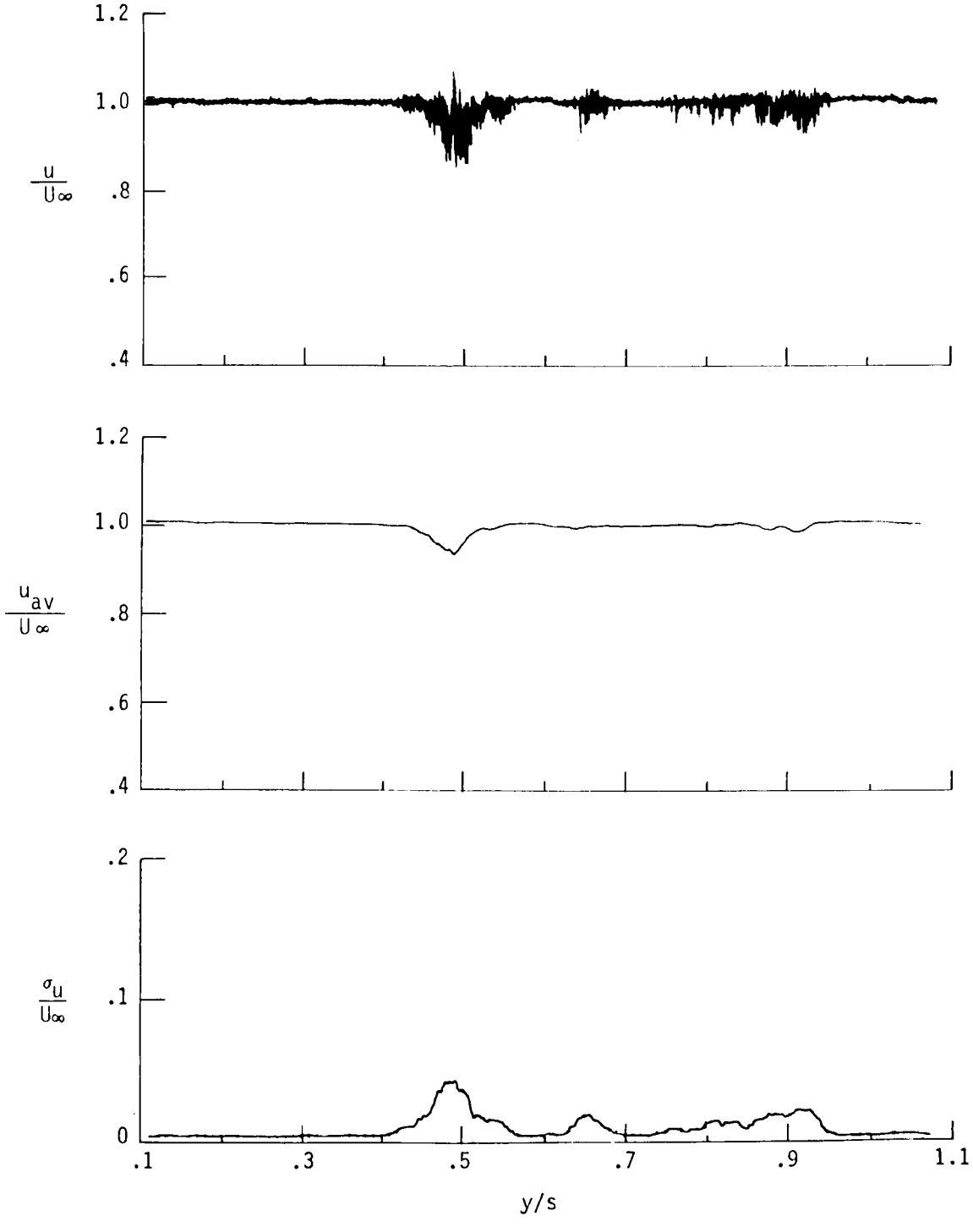


(b) Axial velocity data.

Figure B6. Concluded.

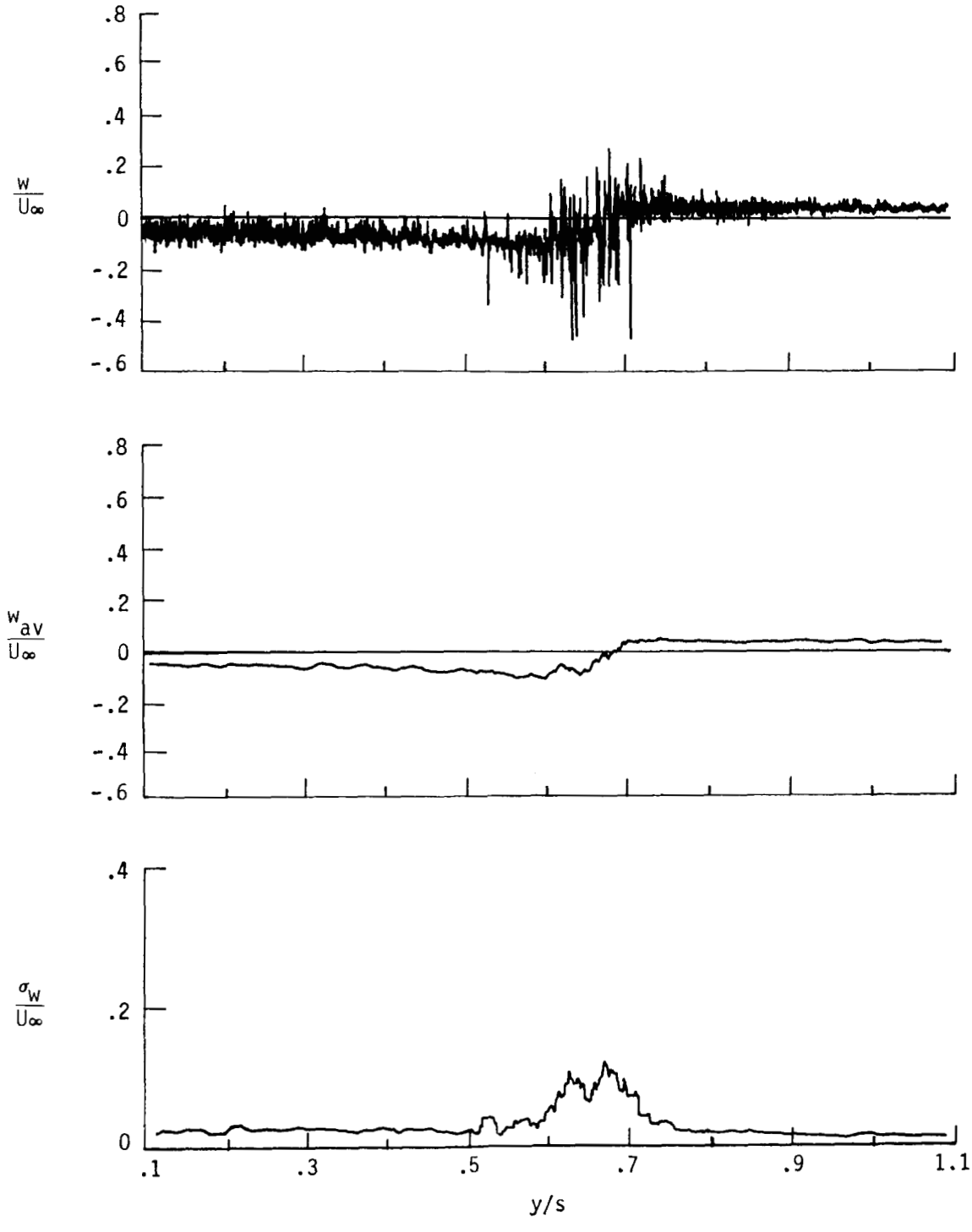


(a) Vertical velocity data.

Figure B7. Typical vertical and axial velocity profiles at $x/s = 11$ taken in the wake of VTW7S$_0$ at $z/s = 0.021$ through a vortex core.

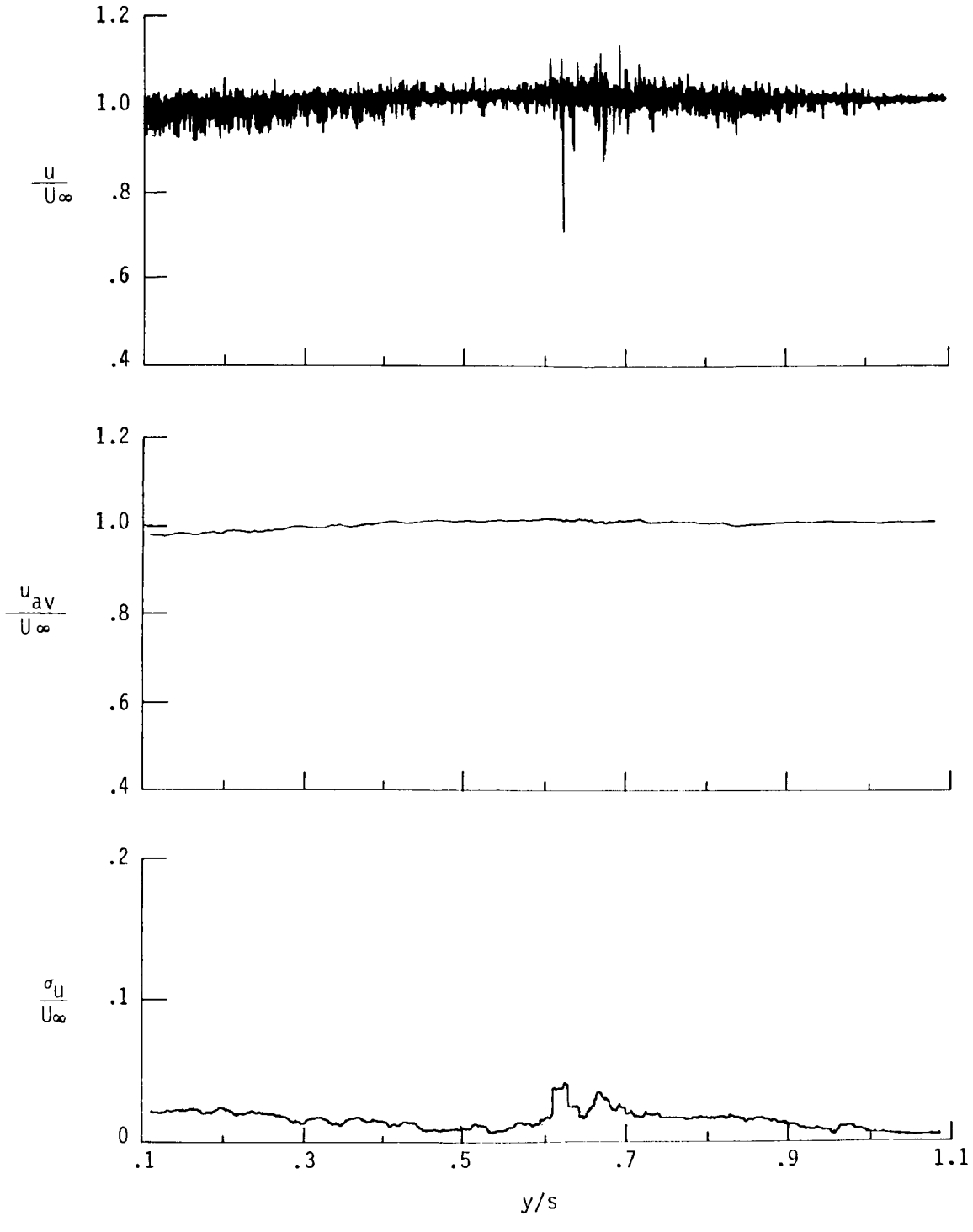


(b) Axial velocity data.

Figure B7. Concluded.

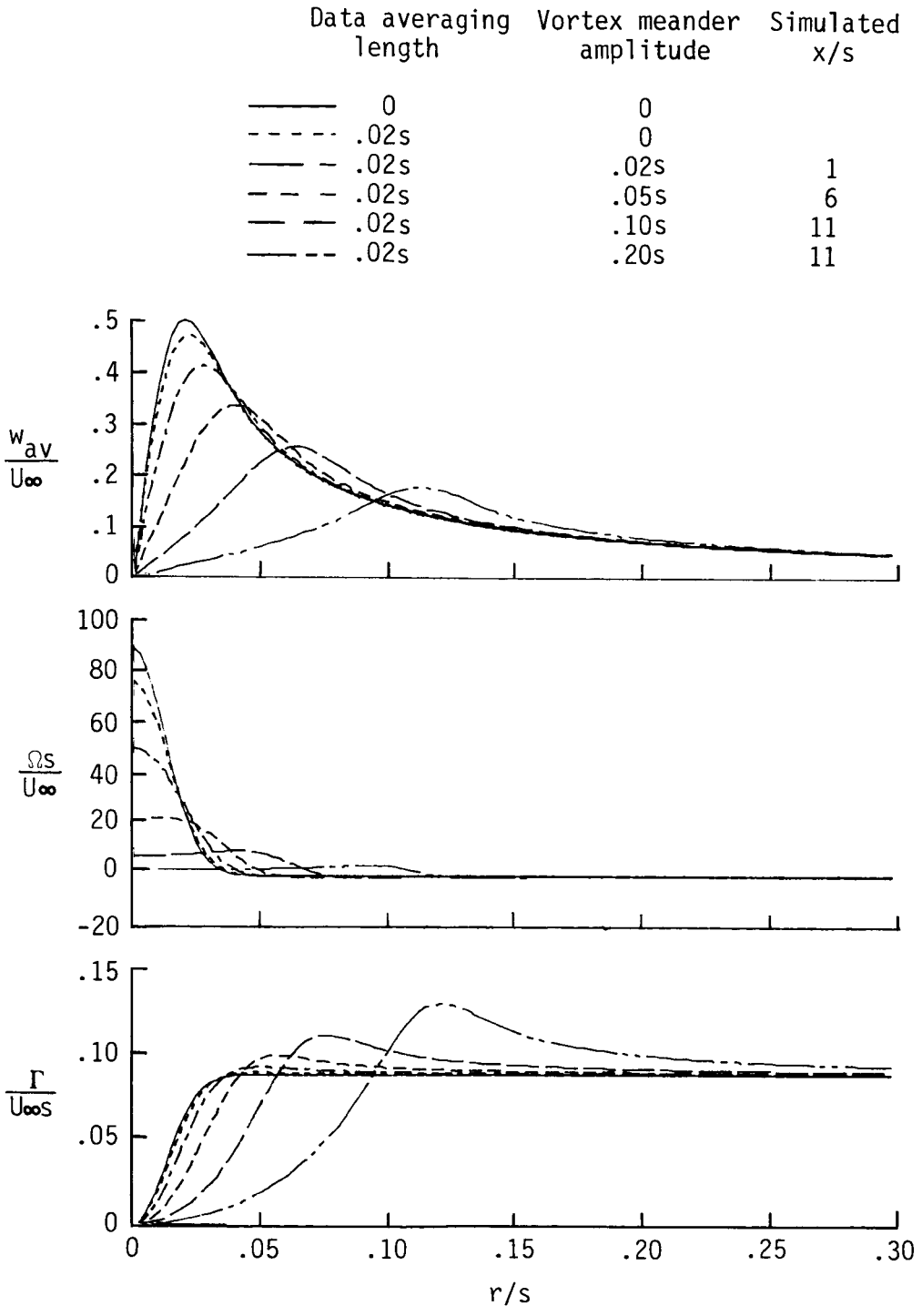


Figure B8. Simulated vortex wake measurements under varying levels of spatial averaging caused by vortex meander and data-averaging technique. True flow field is represented by zero averaging length and zero meander amplitude.

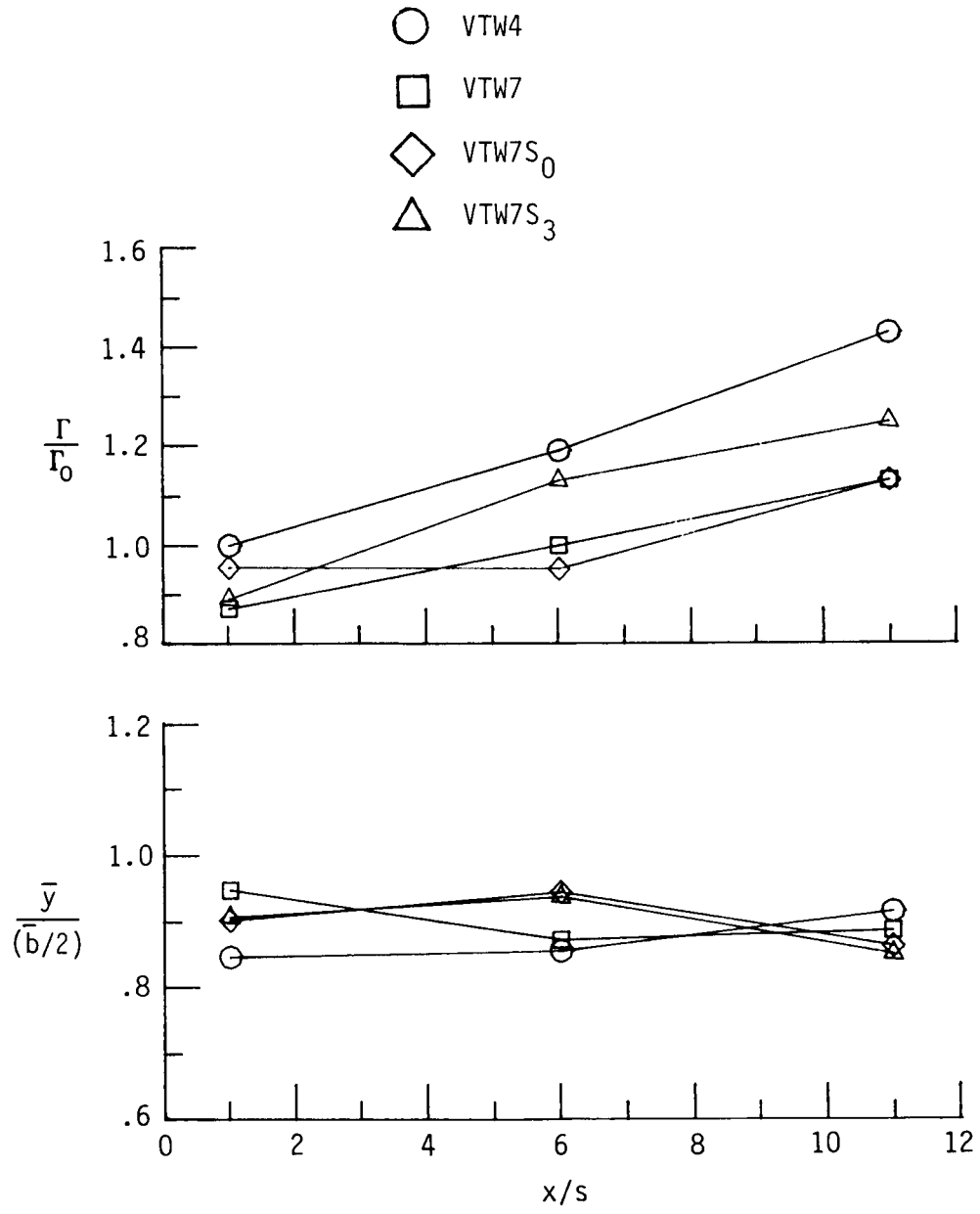


Figure B9. Ratios of wake-integrated and span-load-derived values of circulation and vorticity centroid.

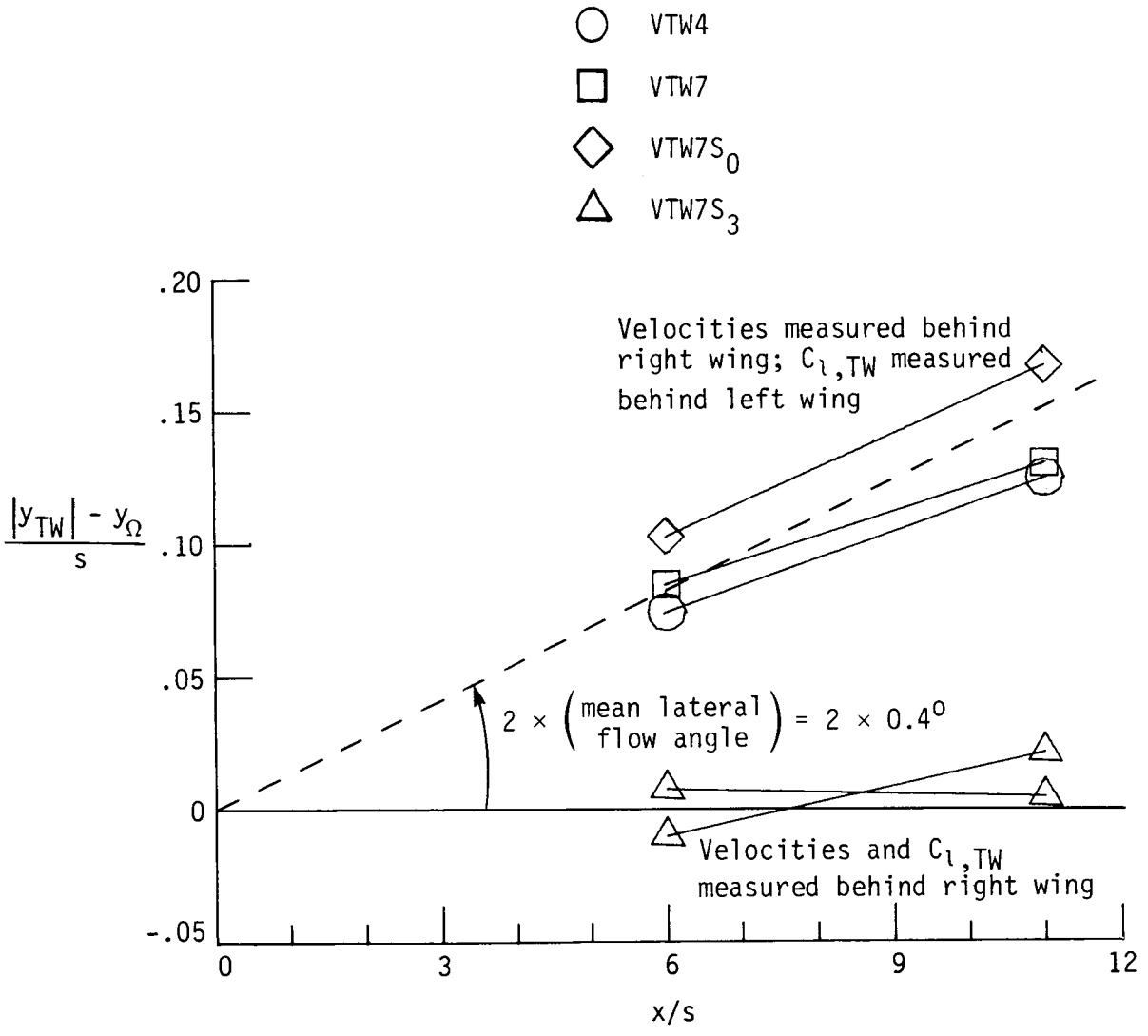


Figure B10. Differences between lateral vortex core positions as determined by wake velocity measurements ($y_\Omega$) and trailing-wing measurements ($y_{TW}$).

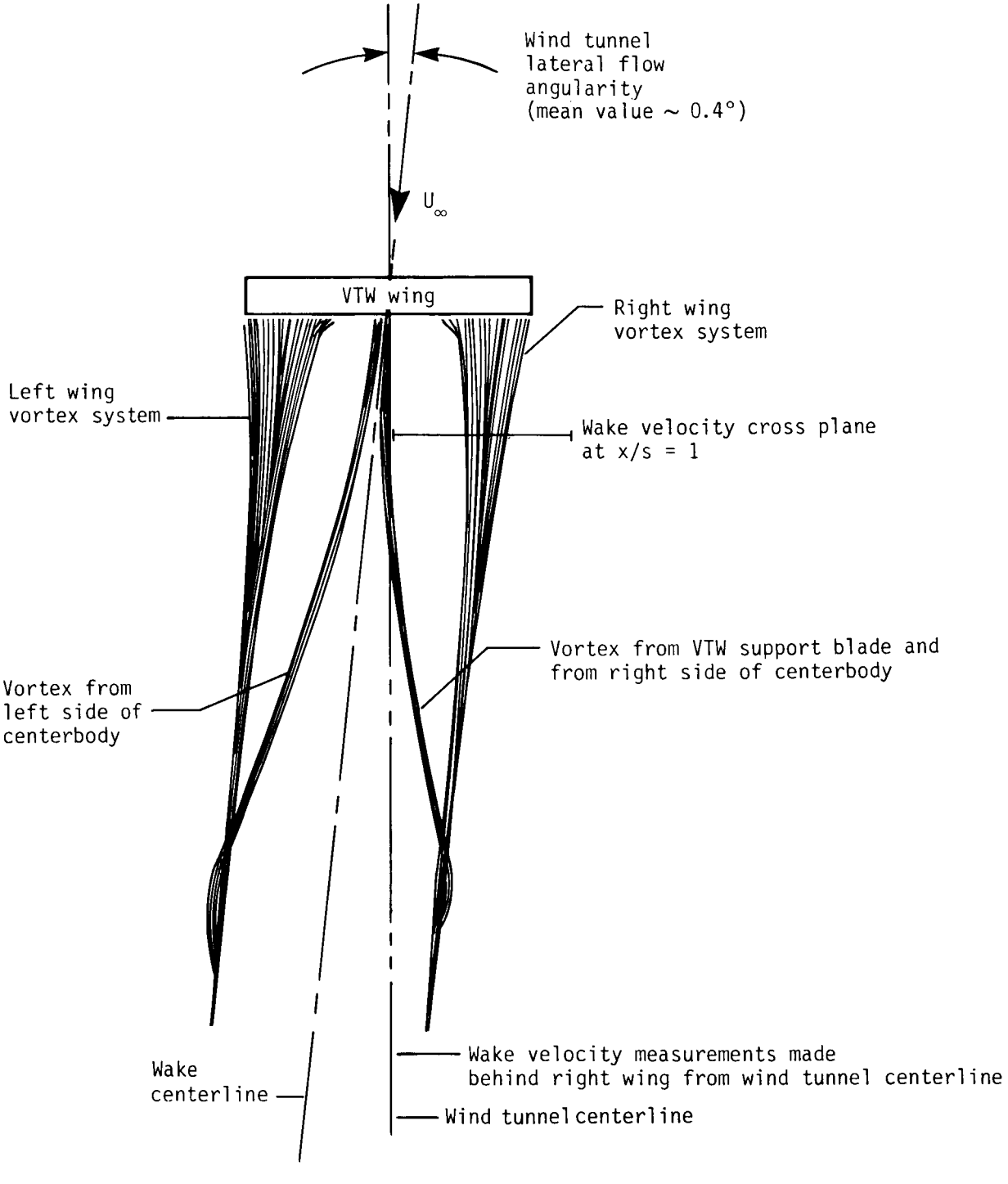


(a) Sketch of vorticity roll up with downstream distance.

Figure B11. Possible effects of wind tunnel lateral flow angularity on wake velocity measurements.

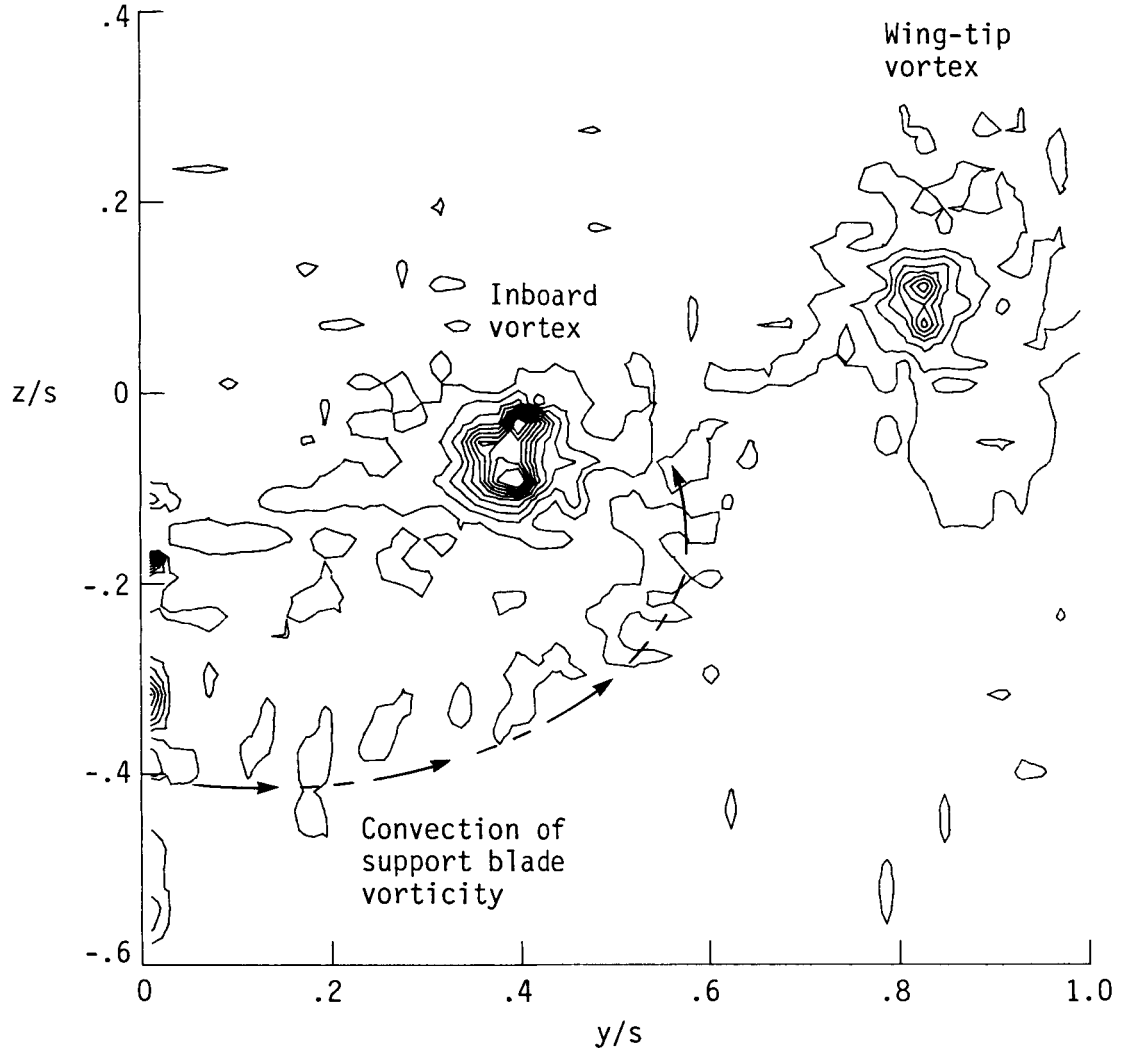


(b) Support blade (and possible centerbody) vorticity wrapping into wake velocity survey region at $x/s = 6$ in wake of VTW7S$_3$. Measured vorticity ($\Omega s/U_\infty$) contours range from 0.2 to 9.2 in increments of 1. Only positive vorticity contours are presented.

Figure B11. Concluded.

## References


1. *Wake Vortex Minimization.* NASA SP-409, 1977.
2. Hallock, J. N., ed.: *Proceedings of the Aircraft Wake Vortices Conference.* Rep. No. FAA-RD-77-68, June 1977. (Available from DTIC as AD A055 510.)
3. Olsen, John H.; Goldburg, Arnold; and Rogers, Milton, eds.: *Aircraft Wake Turbulence and Its Detection.* Plenum Press, 1971.
4. El-Ramly, Z.: *Aircraft Trailing Vortices—A Survey of the Problem.* Rep. No. ME/A 72-1, Carleton Univ. (Ottawa, Canada), Nov. 1972.
5. Lissaman, P. B. S.; Crow, S. C.; MacCready, P. B., Jr.; Tombach, I. H.; and Bate, E. R., Jr.: *Aircraft Vortex Wake Descent and Decay Under Real Atmospheric Effects.* FAA-RD-73-120, Oct. 1973. (Available from DTIC as AD 771 311.)
6. Donaldson, Coleman duP.; Bilanin, Alan J.; and Crow, Steven C., compilers: *Vortex Wakes of Large Aircraft.* AIAA Professional Study Series, June 1974.
7. Croom, Delwin R.: The Development and Use of Spoilers as Vortex Attenuators. *Wake Vortex Minimization,* NASA SP-409, 1977, pp. 339–368.
8. Patterson, James C., Jr.; Hastings, Earl C., Jr.; and Jordan, Frank L., Jr.: Ground Development and Flight Correlation of the Vortex Attenuating Spline Device. *Wake Vortex Minimization,* NASA SP-409, 1977, pp. 271–303.
9. Hastings, Earl C., Jr.; and Champine, Robert A.: Results of Full-Scale Vortex Attenuation Flight Experiments. *Fifth Annual Symposium Proceedings 1974, Advancements in Flight Test Engineering,* Soc. Flight Test Eng., 1974, pp. 4-26–4-46.
10. Betz, A.: *Behavior of Vortex Systems.* NACA TM 713, 1933.
11. Donaldson, Coleman duP.; and Bilanin, Alan J.: Vortex Wakes of Conventional Aircraft. AGARD-AG-204, May 1975.
12. Rossow, Vernon J.: Inviscid Modeling of Aircraft Trailing Vortices. *Wake Vortex Minimization,* NASA SP-409, 1977, pp. 9–59.
13. Bilanin, Alan J.; Donaldson, Coleman duP.; and Snedeker, Richard S.: *An Analytic and Experimental Investigation of the Wakes Behind Flapped and Unflapped Wings.* AFFDL-TR-74-90, U.S. Air Force, Sept. 1974. (Available from DTIC as AD A021 344.)
14. Corsiglia, Victor R.; and Dunham, R. Earl, Jr.: Aircraft Wake-Vortex Minimization by Use of Flaps. *Wake Vortex Minimization,* NASA SP-409, 1977, pp. 305–338.
15. Miller, E. R., Jr.; and Brown, C. E.: *An Experimental Study of Trailing Vortex Wakes Using a Large Towing Tank.* Tech. Rep. 7105-1 (Contract NAS1-10546), Hydronautics, Inc., Aug. 1971.
16. Jones, W. P.; and Rao, B. M.: Airloads and Moments on an Aircraft Flying Over a Pair of Inclined Trailing Vortices. *Aircraft Wake Turbulence and Its Detection,* John H. Olsen, Arnold Goldburg, and Milton Rogers, eds., Plenum Press, 1971, pp. 523–545.
17. Madden, Stephen J., Jr.; and Harlan, Raymond B., eds.: *A Program To Analyze and Model Trailing Vortices on Airports.* RN-69 (Contract No. DOT-TSC-166), Dep. Aeronaut. & Astronaut., Massachusetts Inst. Technol., Oct. 1971.
18. Nelson, Robert C.; and McCormick, Barnes W.: Aircraft-Vortex Penetration. SAE Tech. Paper 730296, Soc. Automot. Eng., Inc., Apr. 1973.
19. Smith, Harriet J.: *A Flight Test Investigation of the Rolling Moments Induced on a T-37B Airplane in the Wake of a B-747 Airplane.* NASA TM X-56031, 1975.
20. Barrows, Timothy M.: Simplified Methods of Predicting Aircraft Rolling Moments Due to Vortex Encounters. AIAA Paper No. 76-61, Jan. 1976.
21. Roberts, Leonard: Persistence and Decay of Wake Vorticity. *Flight/Ground Testing Facilities Correlation,* AGARD-CP-187, Apr. 1976, pp. 9-1–9-10.
22. Dunham, R. Earl, Jr.: Unsuccessful Concepts for Aircraft Wake Vortex Minimization. *Wake Vortex Minimization,* NASA SP-409, 1977, pp. 221–249.
23. McWilliams, Ian G.: Hazard Extent About Aircraft Trailing Wake Vortices—Analytic Approach. *Proceedings of the Aircraft Wake Vortices Conference,* J. N. Hallock, ed., Rep. No. FAA-RD-77-68, June 1977, pp. 23–30.
24. Bofah, K. K.: Some Remarks on Aircraft Wake Vortex Analysis. *Proceedings of the Aircraft Wake Vortices Conference,* J. N. Hallock, ed., Rep. No. FAA-RD-77-68, June 1977, pp. 31–46.
25. Tymczyszyn, Joseph J.; and Barber, Marvin R.: Techniques for Early Demise of Vortices—A Pilot's View. *Proceedings of the Aircraft Wake Vortices Conference,* J. N. Hallock, ed., Rep. No. FAA-RD-77-68, June 1977, pp. 247–263.
26. El-Ramly, Z.: Induced Rolling Moment on Trailing Wings. AIAA Paper 77-663, June 1977.
27. Barber, Marvin R.; and Tymczyszyn, Joseph J.: Wake Vortex Attenuation Flight Tests: A Status Report. *1980 Aircraft Safety and Operating Problems,* Joseph W. Stickle, compiler, NASA CP-2170, Part 2, 1981, pp. 387–408.
28. Holbrook, G. Thomas; and Dunham, Dana Morris: *Detailed Pressure Distribution Measurements Obtained on Several Configurations of an Aspect-Ratio-7 Variable Twist Wing.* NASA TM-86308, 1985.
29. Leonard, A.: Vortex Methods for Flow Simulation. *J. Comput. Phys.,* vol. 37, no. 3, Oct. 1980, pp. 289–335.
30. Weston, R. P.; and Liu, C. H.: Approximate Boundary Condition Procedure for the Two-Dimensional Numerical Solution of Vortex Wakes. AIAA-82-0951, June 1982.
31. Weston, Robert Paul: Refinement of a Method for Determining the Induced and Profile Drag of a Finite Wing From Detailed Wake Measurements. Ph.D. Diss., Univ. of Florida, 1981.
32. Tulinius, J.: *Unified Subsonic, Transonic, and Supersonic NAR Vortex Lattice.* TFD-72-523, Los Angeles Div., North American Rockwell, Apr. 27, 1972.
33. Croom, Delwin R.: *Low-Speed Wind-Tunnel Investigation of Forward-Located Spoilers and Trailing Splines as Trailing-Vortex Hazard-Alleviation Devices on an Aspect-Ratio-8 Wing Model.* NASA TM X-3166, 1975.

34. Croom, Delwin R.; Vogler, Raymond D.; and Williams, Geoffrey M.: *Low-Speed Wind-Tunnel Investigation of Flight Spoilers as Trailing-Vortex-Alleviation Devices on a Medium-Range Wide-Body Tri-Jet Airplane Model.* NASA TN D-8360, 1976.
35. Herriot, John G.: *Blockage Corrections for Three-Dimensional-Flow Closed-Throat Wind Tunnels, With Consideration of the Effect of Compressibility.* NACA Rep. 995, 1950. (Supersedes NACA RM A7B28.)
36. Gillis, Clarence L.; Polhamus, Edward C.; and Gray, Joseph L., Jr.: *Charts for Determining Jet-Boundary Corrections for Complete Models in 7- by 10-Foot Closed Rectangular Wind Tunnels.* NACA WR L-123, 1945. (Formerly NACA ARR L5G31.)
37. Brown, Clinton E.: *The Use of Ship Model Basins for the Study of Vortex Wake Phenomena.* AFOSR-TR-73-0567, U.S. Air Force, Mar. 1973. (Available from DTIC as AD 758 893.)
38. Hirsh, Joel E.; and Williamson, Guy G.: *Analysis and Simulation of Flow Downstream of a Variable Twist Segmented Wing.* Rep. No. 398 (Contract NAS1-15409), Aeronautical Research Associates of Princeton, Inc., Sept. 1979.
39. Sellers, William L., III; and Elliott, Joe W.: Recent Applications of a Laser Velocimeter in the Langley 4- by 7-Meter Wind Tunnel. NASA paper presented at 8th Biennial Symposium on Turbulence, Univ. of Missouri-Rolla, Sept. 1983.
40. Peake, David J.; and Tobak, Murray: Three-Dimensional Flows About Simple Components at Angle of Attack. *High Angle-of-Attack Aerodynamics,* AGARD-LS-121, Dec. 1982, pp. 2-1–2-56.
41. Jorgensen, Leland Howard: *Prediction of Static Aerodynamic Characteristics for Slender Bodies Alone and With Lifting Surfaces to Very High Angles of Attack.* NASA TR R-474, 1977.
42. Hess, John L.: *Calculation of Potential Flow About Arbitrary Three-Dimensional Lifting Bodies.* Rep. No. MDC J5679-01 (Contract N00019-71-C-0524), McDonnell Douglas Corp., Oct. 1972. (Available from DTIC as AD 755 480.)
43. Crow, Steven C.: Stability Theory for a Pair of Trailing Vortices. AIAA Paper No. 70-53, Jan. 1970.
44. Parks, P. C.: A New Look at the Dynamics of Vortices With Finite Cores. *Aircraft Wake Turbulence and Its Detection,* John H. Olsen, Arnold Goldburg, and Milton Rogers, eds., Plenum Press, 1971, pp. 355–388.
45. Yuan, S. W.; and Bloom, A. M.: Experimental Investigation of Wing-Tip Vortex Abatement. ICAS Paper 74-35, Aug. 1974.
46. Crow, S. C.; and Bate, E. R., Jr.: Lifespan of Trailing Vortices in a Turbulent Atmosphere. *J. Aircr.,* vol. 13, no. 7, July 1976, pp. 476–482.
47. Bliss, Donald B.: Effect of Unsteady Forcing on the Sinusoidal Instability of Vortex Wakes. *J. Aircr.,* vol. 19, no. 9, Sept. 1982, pp. 713–721.
48. Rotta, Nicholas R.: *The Stability of a Vortex Pair in the Presence of a Ground Plane.* Rep. No. 71-81A (Contract No. F44620-70-C-0106), Oceanics, Inc., June 1971 (Revised Nov. 1971). (Available from DTIC as AD 732 473.)
49. Jones, W. P.; and Chevalier, H. L.: Aircraft Trailing Vortex Instabilities. ICAS Paper 74-34, Aug. 1974.
50. Jacobs, Eastman N.; and Sherman, Albert: *Airfoil Section Characteristics as Affected by Variations of the Reynolds Number.* NACA Rep. 586, 1937.
51. Corsiglia, V. R.; Schwind, R. G.; and Chigier, N. A.: Rapid Scanning, Three-Dimensional Hot-Wire Anemometer Surveys of Wing-Tip Vortices. *J. Aircr.,* vol. 10, no. 12, Dec. 1973, pp. 752–757.
52. Orloff, K. L.; Corsiglia, V. R.; Biggers, J. C.; and Ekstedt, T. W.: *Investigating Complex Aerodynamic Flows With a Laser Velocimeter.* NASA TM X-73171, 1976.
53. Gartrell, Luther R.; and Rhodes, David B.: *A Scanning Laser-Velocimeter Technique for Measuring Two-Dimensional Wake-Vortex Velocity Distributions.* NASA TP-1661, 1980.

Standard Bibliographic Page

| 1. Report No. | 2. Government Accession No. | 3. Recipient's Catalog No. |
|---|---|---|
| NASA TP-2442 | | |

| 4. Title and Subtitle | 5. Report Date |
|---|---|
| Vortex Wake Alleviation Studies With a Variable Twist Wing | November 1985 |
| | 6. Performing Organization Code: 505-31-23-13 |
| 7. Author(s): G. Thomas Holbrook, Dana Morris Dunham, and George C. Greene | 8. Performing Organization Report No.: L-15870 |
| 9. Performing Organization Name and Address: NASA Langley Research Center, Hampton, VA 23665 | 10. Work Unit No. |
| | 11. Contract or Grant No. |
| 12. Sponsoring Agency Name and Address: National Aeronautics and Space Administration, Washington, DC 20546 | 13. Type of Report and Period Covered: Technical Paper |
| | 14. Sponsoring Agency Code |

15. Supplementary Notes

16. Abstract

Vortex wake alleviation studies were conducted in a wind tunnel and a water towing tank using a multisegmented wing model which provided controlled and measured variations in span load. Fourteen model configurations were tested at a Reynolds number of $1 \times 10^6$ and a lift coefficient of 0.6 in the Langley 4- by 7-Meter Tunnel and the Hydronautics Ship Model Basin water tank at Hydronautics, Inc., Laurel, Md. Detailed measurements of span load and wake velocities at one semispan downstream correlated well with each other, with inviscid predictions of span load and wake roll up, and with peak trailing-wing rolling moments measured in the far wake. Average trailing-wing rolling moments were found to be an unreliable indicator of vortex wake intensity because vortex meander did not scale between test facilities and free-air conditions. A tapered-span-load configuration, which exhibited little or no drag penalty, was shown to offer significant downstream wake alleviation to a small trailing wing. The greater downstream wake alleviation achieved with the addition of spoilers to a flapped-wing configuration was shown to result directly from the high incremental drag and turbulence associated with the spoilers and not from the span load alteration they caused.

| 17. Key Words (Suggested by Authors(s)) | 18. Distribution Statement |
|---|---|
| Vortex wake<br>Vortex alleviation<br>Trailing-vortex hazard<br>Vortex flows<br>Span load<br>Wake velocities | Unclassified - Unlimited<br><br>Subject Category 01 |

| 19. Security Classif.(of this report) | 20. Security Classif.(of this page) | 21. No. of Pages | 22. Price |
|---|---|---|---|
| Unclassified | Unclassified | 116 | A06 |

For sale by the National Technical Information Service, Springfield, Virginia 22161

NASA-Langley, 1985

National Aeronautics and
Space Administration
Code NIT-3

Washington, D.C.
20546-0001





2 2 1J,A, 851119 S00161DSR
DEPT OF THE AIR FORCE
ARNOLD ENG DEVELOPMENT CENTER(AFSC)
ATTN: LIBRARY/DOCUMENTS
ARNOLD AF STA TN 37389

NASA